AN ABSTRACT OF THE THESIS OF

Thomas Keffer for the Doctor of Philosophy

in Oceanography presented on October 27, 1980

Title: Mean and Time-Dependent Temperature and Vorticity Balances

in the Sub-Tropical North Atlantic

Redacted for privacy

Abstract approved: P. P. Niiler

The North-Atlantic mesoscale eddy field, as observed by POLYMODE Array III, is discussed and compared with previous MODE and POLYMODE studies. Cluster A, located on the western slopes of the Mid-Atlantic Ridge, had similar characteristics with the MODE region with longer time scales and reduced deep water energies due to the rough topography. Cluster B, on the eastern slopes, showed bottom trapping of energy, perhaps due to western intensification within the eastern basin. Cluster C, in the Atlantic North Equatorial Current, showed a complex vertical structure and little or no down gradient heat fluxes.

The Array III current meter data was used to derive absolute u, v, w mean velocity profiles at the three clusters. These were then used to determine the mean potential temperature, salinity,

and potential density balances. These were found to be consistent with horizontal eddy diffusion and vertical salt fingering. The implications on the β-spiral method for determining absolute velocities are discussed.

The time dependent temperature and vorticity balance at Cluster C was considered. The linear temperature equation was found to predict correctly the location of a critical layer. Relative vorticity changes were found to balance advection of planetary vorticity in the low frequency (81-324 days). Advection of vorticity was found to be important at mid frequencies (30-65 days) and stretching at high frequencies (4-28 days). Finally, the baroclinic instability model of Gill, Green and Simmons was tested for predicted modal shapes, growth rates, and heat fluxes.

MEAN AND TIME-DEPENDENT TEMPERATURE AND VORTICITY BALANCES IN THE SUB-TROPICAL NORTH ATLANTIC

by

Thomas Keffer

A THESIS

submitted to

Oregon State University

in partial fulfillment of
the requirements for the
degree of

Doctor of Philosophy

completed October 27, 1980

Commencement June 1981

APPROVED:

Redacted for privacy

Professor of Oceanography

Redacted for privacy

Dean of the School of Oceanography

Redacted for privacy

Dean of Graduate School

Thesis presented October 27, 1980

Typed by Pamela Wegner for Thomas Keffer

ACKNOWLEDGEMENTS

I thank my major professor, Dr. Peter Niiler, for serving as my scientific guru over the last three years. His continuous stream of novel ideas and insights has been dazzling and I have been fortunate enough to catch a few as they went by. He has also provided three years of stable funding and shielded me from the vagarities of the grantsmanship game.

Roland DeSzoeke has been of invaluable help in separating the harebrained from the plausible and in sorting out the subtleties of the baroclinic instability process. He has also served as my surrogate adviser during Peter Niiler's leave of absence.

I was fortunate enough to inherit the statistical package that was started by Chet Koblinsky. His spectacular computer output formats were as accurate as they were impressive. I was able to build on them rather than start from scratch. Chet also served as office-mate, early morning skiing and biking buddy, and most recently, long distance telephone confidant.

Joe Jennings has been a faithful roommate for three years. Without his Indian cooking I would never have been introduced to popadoms or had the courage to try something as smelly as Asafoetida.

Other people who have helped in one way or another are Dennis Mildner, Art Woolf, Joan Gottlieb, Jack Semura, and Bruce Marsh.

But Corvallis will be remembered most of all for where I met Heidi Powell. She has been my greatest inspiration and morale booster. I have never met somebody with her enthusiasm, spontaneity,

and optimism. I thank her entire family for giving me a home away from home.

But most of all I thank my first family. I continue to marvel my sister's ability to make a living at those things the rest of us only dream about. My parents have taught me the importance of independent thinking and have patiently endured my sometimes sophomoric eras. I have been incredibly fortunate to be on the receiving end of 28 years of abundant love and support from all of them.

TABLE OF CONTENTS

LIST OF FIGURES

Chapter III

Chapter IV

Chapter I

Introduction

POLYMODE Array III is part of a much larger joint US/USSR program to provide a first order look at mesoscale (eddy) variability within the North Atlantic. Previous studies included the MODE series (MODE-0, MODE-I) and early POLYMODE studies (Array I, Array II). The last of the POLYMODE studies, the Local Dynamics Experiment (LDE) was recovered in June, 1979 and is currently being analyzed.

Comprehensive accounts of these experiments can be found in the literature but are briefly restated here. MODE (Mid-Ocean Dynamics Experiment) consisted of two parts, referred to as MODE-0 and MODE-I. The former, MODE-0, was designed to test space and time scales and to provide energy estimates so as to optimally design the upcoming MODE-I. Instrument and mooring designs were also tested. It was found that a subsurface mooring with distributed buoyancy provided the minimal contamination due to rotor "pumping" from surface wave induced motions. Because of this study all subsequent MODE and POLYMODE moorings used this design. Fluctuations were dominated by time scales of about 20 days and length scales of approximately 100km. A full report can be found in Gould, Schmitz and Wunsch (1974).

MODE-I was a much larger experiment that ran from March to July of 973 in an area southwest of Bermuda. Objectives were to further resolve any dominant space and time scales, to provide quantitative estimates of eddy kinetic and potential energies, and to examine the zero order dynamics of the eddy variability. A dominant time scale of 15-20 days was again found with a vertical scale comparable to the water depth, implying the dominance of low

barotropic or near-barotropic modes. Longer periods were found to be largely zonal in character and confined to the thermocline. A reduction of barotropic energy was found over rough topography.

The temperature data was expanded as a set of free linear Rossby waves. The first three modes described 88% of the energy. However, phase locking was observed between the supposedly independent modes. The possibility of baroclinic instability as an energy source was also examined. But the mean shears, needed as an energy source, were very weak and, indeed, significant heat fluxes were not found. Upward phase propagation is also a signature of baroclinic instability (motions at depth leading more shallow ones) but no phases were found that were statistically different from zero. The nearby Gulf Stream was hypothesized as an energy source. Details can be found in the comprehensive report of Richman, Wunsch and Hogg (1977).

The POLYMODE program was a still larger international sequel to the MODE series. Four U.S. arrays as well as Soviet, Canadian, and British arrays were involved. POLYMODE Array I was deployed along 28°N and 60°W (see Figure 1) from August, 1974 to May, 1975. Two orders of magnitude variation in eddy kinetic energy at 4000m were found. The maximum energy was found near the Gulf Stream, decaying to a minimum near the MODE-I site (Schmitz, 1976).

Array II was deployed along 55°W and 37°N (Fig. 1) from May, 1975 to July, 1977. Motion was found to be more baroclinic

in regions with lower eddy kinetic energy. Near the Gulf Stream, the kinetic energy spectrum was not found to be red, unlike the MODE-I area where energy increased continuously with decreasing frequency (Schmitz, 1978). A heavily instrumented mooring at 31^{o} 35'N, 54^{o} 56'W was used by Bryden (1980) to show conservation of potential vorticity: $\beta v = f w_z$.

POLYMODE Array III was deployed from May, 1977 to May, 1978 and is the subject of Chapters II thru IV.

In the continuing series of still larger experiments, the Local Dynamics Experiment (LDE) was the largest yet. If MODE-I was designed to look at the zero order dynamics of the eddy field then the LDE was designed to provide a first order look. It was divided into two components. The first was an extensive two month experiment that included vertical profiling, SOFAR floats, and hydrographic surveys. The second part was an overlapping 15 month deployment of 9 closely spaced moorings, recovered in July, 1979. Horizontal coverage is sufficient to allow for the first time explicit estimation of the advection of relative vorticity. The relative energies of all of the terms in the complete vorticity equation will be evaluated. Energy transfer from mean kinetic and potential energy reservoirs to eddy energy will also be estimated.

Chapter II of this thesis discusses the mesoscale eddy field as observed by Array III in largely qualitative terms. Also considered is the nature of the hydrographic environment that the clusters were placed in.

In chapter III, profiles of the absolute velocity field in the Array III area are derived and used, in conjunction with historical

hydrographic data, to calculate divergence of conserved quantities (temperature, salinity, density) by mean motions. The nature of the implied eddy diffusion is then considered. The results are also compared to those derived from the so-called "β-spiral" method.

Chapter IV treats the time-dependent temperature and vorticity balances. Horizontal advection of temperature is correlated with local change of temperature. Vertical advection is estimated as the residual. Evidence of the existence of a critical layer is presented. Within the vorticity equation, advection of planetary vorticity, local change of relative vorticity and stretching are estimated. Advection of relative vorticity is found to be important in some frequency bands.

References

Bryden, H.L., (1980), Geostrophic vorticity balance in Mid-Ocean. J. of Geophysical Research. In press.

Gould, W.J., W.J. Schmitz, Jr. and C. Wunsch, (1974), Preliminary field results for a Mid-Ocean Dynamics Experiment (MODE-0). Deep-Sea Res., 21, 499-528.

Richman, J.G., C. Wunsch and N.G. Hogg, (1977), Space and time scales of mesoscale motion in the Western North Atlantic. Rev. of Geophysics and Space Physics, 15, 385-420.

Schmitz, W.J., Jr., (1976), Eddy kinetic energy in the deep Western North Atlantic. J. of Geophysical Research, 81, (27), 4981-4982.

Schmitz, W.J., Jr., (1978), Observations of the vertical distribution of low-frequency kinetic energy in the Western North Atlantic. J. of Marine Research, 36, (3), 295-310.

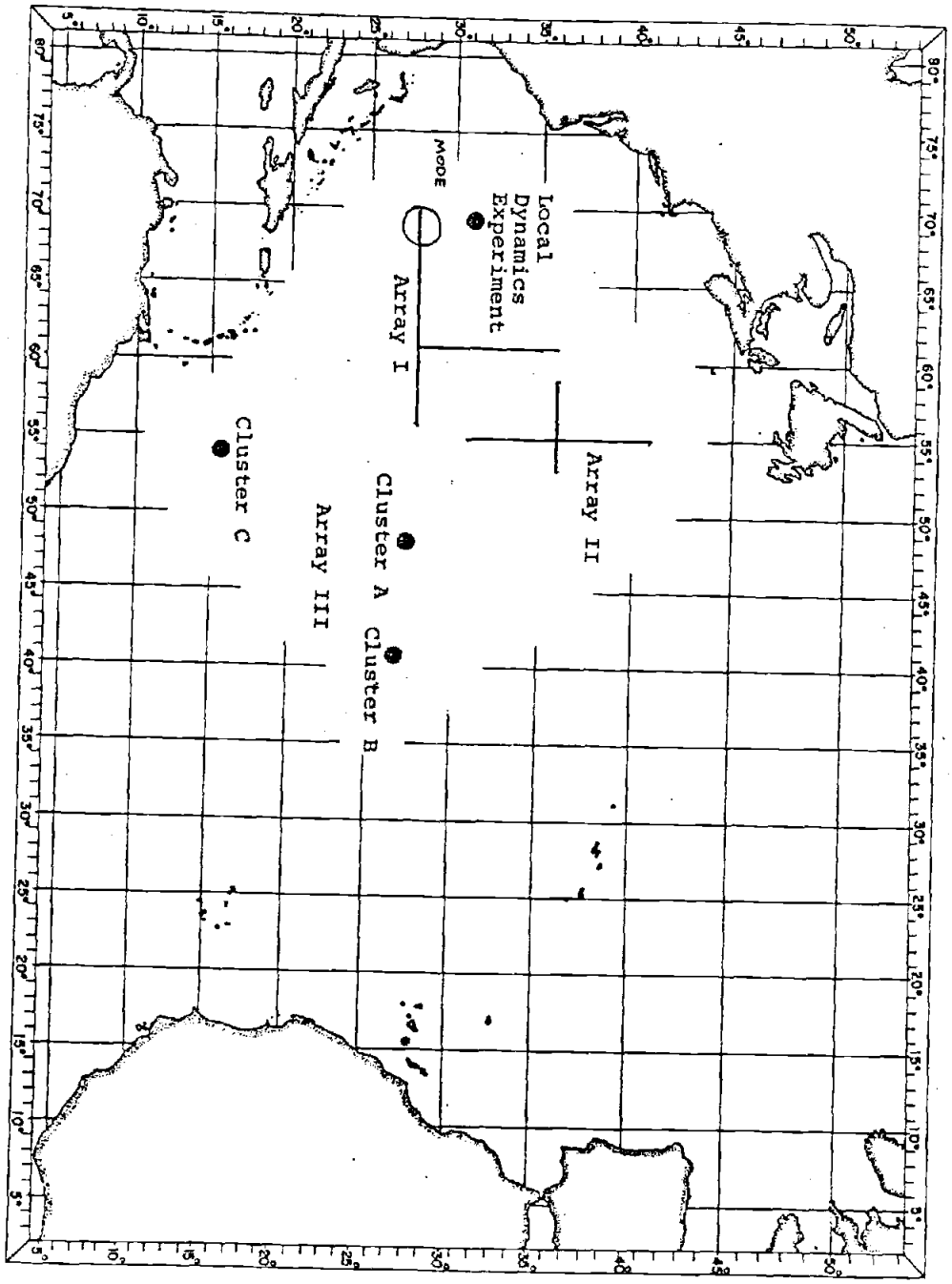
MODE
Local
Dynamics
Experiment
Array I
Array II
Array III
Cluster A
Cluster B
Cluster C

Figure 1

Chapter II

Low-Frequency Motions Observed in POLYMODE Array III: The Mid-Atlantic Ridge and the Atlantic North-Equatorial Current

by

Thomas Keffer
School of Oceanography
Oregon State University

in cooperation with

Lee-lueng Fu
Joint Program in Oceanography
M.I.T. / W.H.O.I.

Pearn P. Niiler
School of Oceanography
Oregon State University

Carl Wunsch
Department of Earth and Planetary Sciences
M.I.T.

I. Introduction

A. Objectives

The MODE-I and early POLYMODE studies have established that there are large variations in the vertical and horizontal structure of the eddy field, as well as orders of magnitude changes of eddy kinetic and potential energy, over small areas of the North Atlantic. So little of the ocean has been explored that it seems unlikely that we have seen the full range of eddy phenomena in either a qualitative or quantitative sense.

A major objective of POLYMODE Array III was to simply expand the first order picture over a more significant fraction of the North Atlantic. As a result, the array consists of three clusters each with four to five moorings, placed in widely different hydrographic and dynamical regimes. Clusters A and B were placed on the western and eastern slopes of the Mid-Atlantic ridge, respectively. The ridge is by far the largest topographic feature in the ocean and its dynamical effect was virtually unknown. Does it act as a western boundary to the eastern basin? Does it "shield" the deep water from Gulf Stream eddy radiation?

Cluster C was deployed in the Atlantic North-Equatorial Current, an area which theoretical models have shown is a likely area for eddy generation. Exploratory measurements to test for down-gradient eddy temperature fluxes were needed to measure the extent of the eddy production.

At all three clusters, estimates of time mean potential and kinetic energies and mean velocities were major objectives. The intention was to map the North Atlantic mesoscale eddy field in a modern descriptive sense. The extent to which estimates of the means are possible will be determined by the dominant time scales, also a major objective.

B. Cluster Bathymetry and Mean Currents

The general location of Clusters A, B, and C are shown on Figure 1. Clusters A and B lie on the western and eastern faces of the Mid-Atlantic Ridge, respectively, and Cluster C is on the northwestern extension of the Demerara Abyssal Plain or in the deep valley of the Amazon Canyon. The deep western North Atlantic basin and the South Atlantic ocean are joined at the Cluster C area. The mean bottom depth at the moorings in Cluster A is 4959 m, at B 4303 m, and at C 5336 m. Figures 2a, 2b, and 2c display the location of each mooring within the rather complicated topographic features that are displayed on the Navoceano NA 9-9A and NA-10 maps. The U.S. Naval cartographers who draw these maps use considerable artistic license to construct individual features. To find locally flat areas for the moorings detailed bottom surveys were carried out during the mooring placements. While new and different individual features were discovered, the general impression is that the maximum excursion of the topography on the Cluster A and B area are well represented (5600 m to 3600 m in Cluster A and 4200 m to 3200 m in Cluster B), although the topographic roughness on the horizontal scale of 1-10 km and 300-800 m is not resolved. Although the Cluster C map displays the depth of the smooth abyssal plain areas well, we discovered a few mountains which rise up to 1400 m above this plain which do not appear on the map. B.C. Heezen and M. Tharp's rendering of the "World Ocean Floor" (Lamont-Doherty Geological Observatory, 1977) presents a more accurate picture of mountains in the Cluster C area. On the horizontal scale of the

mooring elements, Cluster A and B are in "very rough" topographic areas because many protuberances can occur between the moorings. Cluster C is in a "moderately rough" area, because an abyssal plain is found over most of the cluster area.

Figure 2 also shows the mean current vectors at 4000 m, 500 m (1500 m at A, B) and 180-200 m levels. In passing, it is very interesting to note how well the 4000 m mean currents at all three clusters follow local bathymetry. In the A and B areas the mean bottom circulation must be very complex; in C there is a well defined, deep, northward flow into the western North Atlantic Basin.

All three clusters were deployed on stiff, jacketed-wire, sub-surface moorings, with a distributed buoyancy. The moorings were designed for a maximum 15^{o} tilt for currents less than 50 cm s^{-1} in the upper 500 m (nominally 2000 lb tension in the line). This was the first POLYMODE experiment where year-long records were obtained in the North-Atlantic above 500 m from sub-surface moorings. The hydrostatic pressure (or depth) of various mooring elements in the clusters was monitored by pressure sensors both in the P/T recorders and the VACMs (180 m level only at C). The rms vertical excursion of the moorings was a few meters, the maximum excursion at A, B, and C was 16 m, 17 m, and 14 m, respectively. Because of the vertical stability of these moorings, no depth correction is applied to the data set. The instruments nearest to the euphotic zone were on Cluster C at the 180 m level. After 353 days in the water the sensor areas were

free of biological foulings, although a few "barnacles" were found attached to the instrument cases or the flotation. There was no evidence of deposits on rotor bearings nor was rotor sticking observed on the records. Details of the individual instrument performance and mooring configurations are in the data reports (Koblinsky, Keffer and Niiler, 1979; Fu and Wunsch, 1979).

II. Hydrography and Large Scale Dynamic Topography

A. T-S Profile

During the recovery cruises CTD casts were made to the bottom at each mooring site. The T-S diagrams at each cluster are presented on Figure 3, along with the nominal locations of the instruments in the water column. Cluster A and B casts were made by the WHOI CTD operation group and Cluster C casts were made by the GEOSECS operations group from Scripps Institute of Oceanography. Both groups used nearly identical Niel Brown (model 11) CTD's. Each cast is calibrated by at least three bottle samples which were located at the relative maxima and minima of salinity. From these diagrams, the clusters and instruments are placed in the context of the North Atlantic water masses.

In all clusters the main thermocline lies between $20^{\circ}C$ and $8^{\circ}C$ and is of similar T-S characteristics. At Cluster C there is a fresh warm water layer above 50 m which can be traced to overflow of surface water of the equatorial rain belt and may at times contain isolated layers of Amazon River water (Mazeika, 1973). At both Clusters A and B the relatively salty water from the Mediterranean outflow lies between $8^{\circ}C$ and $5^{\circ}C$. At Cluster C (and at Cluster B, mooring 627), the salinity minimum at $6^{\circ}C$ is characteristic of water in the intermediate levels of the South Atlantic or Antarctic. The bottom instruments of Cluster A and B are in the North atlantic Deep Water while the bottom 1500 m of water at C is clearly of Antarctic bottom water origin (see insert on Figure 3c).

It is interesting to note the variable character of the T-S diagram at Cluster B when compared to Clusters A and C. Near the surface, and at 700-1500 m, the individual T-S diagrams show a signature which is typical of interleaving of water masses. Individual traces of salinity as a function of depth show that in the main thermocline (of Cluster C as well) there is considerable layering, while the T-S variability above and below the thermocline is more likely due to interleaving. Apparently, the water masses above 300 m and within the Mediterranean outflow are broken up or patchy on the horizontal scale of the clusters and hence the temperature variability at these levels may not be a reliable measure of density change.

B. Brunt-Vaisala Profiles

Figure 4 shows the Brunt-Vaisala frequency at a representative mooring within each cluster as observed during the recovery cruises. At each depth a density versus depth curve at 2.5 m resolution is computed within a 50 m band (100 m below 1000 m) about the mean pressure at that depth. The density is referenced to the mean pressure to remove the effects of compressibility and adiabatic heating. Then a least squares linear fit of this local potential density versus depth relation is determined. The $(\text{Brunt-Vaisala frequency})^2$ is equal to the slope of the local potential density versus depth curve, multiplied by gravitational acceleration and divided by the mean potential density. Between the surface and 1000 m a value is computed every 25 m and below, every 50 m.

The Cluster A and B Vaisala-frequency profiles are similar above 3000 m, while below the stratification is significantly larger at A than at B. Both have a relatively shallow seasonal pycnocline (2.0-2.6 cph) extending to 200 meters. At Cluster C the permanent pycnocline lies between 100 and 400 m. The small minimum at 120 m seems to be a permanent feature and is associated with the shallow salinity maximum. Below 4000 m the water at C is relatively strongly stratified except for a 200 m column at the bottom (the bottom depth was estimated to be 5281 m, the last data point was at 5275 m). Within this bottom layer there are significant changes in potential temperature indicating it was not well mixed at the time of the observation. Because the 15-16 minute sampling

rate of the instruments gives a Nyquist frequency of .5 cph the time series do not resolve Vaisala frequency phenomena above 1000 m.

C. Historical Density Field

To display the horizontal structure of the main thermocline density field in the Array III area we use hydrographic stations in the National Oceanographic Data Center's (NODC) archived bottle data, edited in the following fashion. We first retain only those stations which report oceanographically plausible values of σ_t ($20.0 < \sigma_t < 30.0$). The study area is then divided into squares of two degrees latitude and longitude. Those stations that report temperature or salinity with values greater than two standard deviations from the mean of each square are eliminated. Of the 3590 stations in the NODC archives, we retain 3033, 2441, 2096, to 100, 300, and 700 meters, respectively. Fewer "good" stations extend to deeper levels. Figure 5 display locations of the 700 m edited stations. These values of σ_t (and other parameters) are interpolated with splines onto a standard 1^o latitude by 1^o longitude grid, smoothed with a Laplacian filter, and then contoured. Figures 6a, 6b, and 6c show the σ_t distributions at 100 m, 300 m, and 700 m, respectively.

The principle features of the geostrophically balanced vertical shear of horizontal currents of the sub-tropical North Atlantic are displayed in these figures. Figure 6a shows the vertical shear associated with the North Equatorial Countercurrent, south of 10^oN latitude. At the 100 m level, an easterly shear is indicated at Clusters A and B and a southerly shear at Cluster C.

Figure 6b shows contours of σ_t at 300 meters.

The vector at Cluster C is the difference vector between observed mean velocities at 180 and 500 meters. Using the vertically integrated thermal wind relationship we computed a geostrophically balanced horizontal velocity difference from the historical hydrographic data. To obtain in situ horizontal density gradients for this computation a least square fit of a sloping plane, $\rho(x,y)$, was made to the in situ density distribution in an area of 4^{o} latitude and 4^{o} longitude around Cluster C. Stations where the potential density did not monotonically increase with depth were eliminated. The results are shown in Table 1.

Figure 6c shows contours of σ_t at 700 meters. The horizontal gradients of the main thermocline have decreased in magnitude and have moved to the north with the deepening thermocline. Observed mean velocity differences between 200 m and 1500 m are shown as vectors at Clusters A and B which are computed from cluster averages of the velocity at each level. Geostrophically derived velocity differences were also calculated using the plane fitting procedure previously described within 6^{o} latitude by 6^{o} longitude boxes. The results are also shown in Table 1.

In Clusters A and B the measured mean flow at 1500 m is to the north-west and is quite stable spatially from mooring to mooring (see Figure 2b, 2c). From the 29 month long record at the central mooring in Cluster A (#630 and its continuation #648) we see that there is temporal stability as well. An exception is the most southerly mooring of Cluster B (#627) which shows a mean velocity still northward, but directed to the east. When the Cluster B moorings were deployed, this mooring was on the southern side of

a well defined edge of the Mediterranean salt tongue. The trace referred to as Station 49 on Figure 3b was taken at this mooring. The water mass transition shows clearly from 1000 to 2000 m.

The 200 m (or 500 m currents) are not well determined with even a 28 month long record at either A or B. Therefore, we can assume that the measured values at 1500 m in Clusters A and B form a stable reference level above which the computed relative geostrophic velocity profile is a better measure of the true mean profile than our directly measured profile. If we add the geostrophically computed velocity difference (Table 1) to the measured 1500 m current, we see that the geostrophically balanced velocity vector rotates counterclockwise with decreasing depth through the main thermocline. As described by Bryden (1976), this pattern of vertical rotation of a mean geostrophic current provides a horizontal divergence of density and this divergence must be balanced by either a vertical sinking or a turbulent divergence of density. As we saw earlier (Figure 3), in the Cluster A and B area, there is a well defined water mass in the main thermocline. In the main thermocline a horizontal divergence of density implies a turbulent convergence of heat (a warming, following horizontal water motion) and turbulent convergence of salt (water becomes more saline). To the south and west of Clusters A and B the ocean surface is heated, there is intense evaporation, and the Ekman layer is convergent. Therefore, our observed motions at A and B is consistent with a vertical convergence of the heat and salt fluxes and/or vertical sinking throughout the column from 1500 m and 200 m.

In the Cluster C area, although the observed and computed vertical shear is consistent between 500 m and 100 m, the mean shear has not been well resolved by the year long records. While the mean rotation of the horizontal flow is not as clearly evident as in Clusters A and B, the observed surface heating, evaporation and mass convergence is very much the same. Hence it is difficult to imagine how the mean heat and salt budgets are satisfied at Cluster C without significant horizontal turbulent processes in the main thermocline or large horizontal and vertical advective patterns in the upper 180 m.

III. Temporal and Spatial Variability

A. Temperature records

With energy in the super-inertial frequency band properly removed by a low-pass filter, daily temperature records at those stations which have the most complete data in each cluster are displayed in Figure 7. Fluctuations with time scales ranging from tens to hundreds of days are general features. Indications of possible annual oscillations, which in the upper levels is characterized by cooling to a constant temperature in winter and warming in summer, can be found at 200 m of Mooring 630 and 495 m of Mooring 623. From 233 m to 663 m of Mooring 81 a possible seasonal signal of the opposite trend may be present, suggesting that the oceanic response to the annual forcing is of opposite sign in the main thermocline and the mixed layer (Myers, 1978).

The temperature variations with shorter than seasonal time scale in the topmost record are generally incoherent with deep ones except the second half of Mooring 81, where fluctuations at depths from 160 m to 663 m are coherent in the vertical. The isolated bursts of warmings at 129 m in the winter period at Mooring 623 is notably different from the others, probably due to large mixing events in the mixed layer. These events become more frequent in the spring as the seasonal thermocline is established.

The deep records of Mooring 630 at depths from 542 m to 4909 m are fairly coherent and in phase with one another, at least for periods greater than 100 days. The short-period (~50 days)

fluctuations at 542 m are not observed at the same depth in other clusters. Recall that this is the level where intermittent occurrence of South Atlantic intermediate water appears on the T-S diagram (Figure 3). For Mooring 623, records in the main thermocline (496 m and 844 m) are apparently coherent (in phase), but below, no apparent coherence is detected.

At the nominal depth 1500 m there is a distinct difference between Moorings 623 and 630; the short-period fluctuations at 623 are believed to be related to the advection of small horizontal scale variation of Mediterranean water in the Cluster B area (see Figure 3b). The temperature fluctuations at Mooring 81 are coherent (in phase) at depths from 180 m to 750 m. Notable features here are the occasional rapid excursions of spikes which are confined to these depths. Phenomena similar to these were also observed in the MODE area (Richman et al., 1977). The raggedness of the record at 663 m (and every other Cluster C record at this depth) is again caused by the variability of the T-S relation which results from the presence of the South Atlantic Intermediate Water at this depth (Figure 3a). The records at 1509 m and 4008 m appear to have very coherent fluctuations with a period of about 70 days. These seemingly regular deep temperature signals were not found in the MODE area.

In summary, the apparent vertical coherence of energy-containing variations through the water column in Cluster A is similar to that found in the MODE area, whereas the variations in the vertical observed in Clusters B and C are novel and more complex features.

B. Velocity Records

Displayed in Figure 8 are the stick diagrams of the low-passed records of horizontal current velocity at the same stations as in Figure 7 except Cluster A where Mooring 629 is shown instead due to the loss of the 4000 m velocity record at Mooring 630.

For moorings in Clusters A and B, velocity fluctuations at nominal depths 200 m and 1500 m are characterized by eddy-like features with time scales of about 50 days that are vertically coherent and in phase. Super-imposed on these "eddies" are short-period fluctuations with time scales of about 10 days and with smaller amplitudes; they are incoherent in the vertical. At 4000m, these records are dominated by short-period fluctuations in both clusters with a time scale of about 15 days in Cluster B and 25 days in Cluster A. This difference in time scale is probably related to the fact that the 4000 m record is closer to the bottom in Cluster B than it is in Cluster A. The weak eddy motion at 4000 m here (eddy kinetic energy is less by one order of magnitude here than the MODE area) is believed to be due to the effects of rough topography, which inhibits large scale horizontal motions and forces the vertical structure of eddy motion to form a node at the bottom. If the eddies are generated in remote flat-bottom areas, where there are appreciable deep velocities, and then propogate to the mooring site, bottom-trapped waves are likely to be generated in the transition area (from smooth to rough bottom) as suggested by the theory and observations of topographic Rossby waves on the continental rise (Suarez, 1971; Thompson and Luyten, 1976). Schmitz (1978) noted a similar decrease of eddy

energy at great depths over rough topography in the POLYMODE Array I area.

For Mooring 81, the time scale of the zonal fluctuations at depths from 160 m to 510 m is apparently longer than that of the meridional fluctuations; the latter is about 30 days and is independent of depth. The eddy-like motion occurs at all depths and are coherent in two separate groups: 1) from 160 m to 510 m; 2) from 2500 m to 4000 m, indicating that the eddy dynamics is probably different in the thermocline than in the deep water. Long-period zonal fluctuations above 500 m are now believed to be a common occurrence in POLYMODE Arrays I, II, and III.

C. Time and space scales

The integral time scale of each long daily average records of u', v', T', is computed from the integral of the square of the lagged autocorrelation function (Richman et al., 1977). Table 2 displays the cluster average values of these quantities. A bracketed value again indicates that values at individual moorings vary by a factor of two. The temperature time scale is most consistent among the moorings in all clusters. It is vertically uniform in both A and C, with the exception of the small value at 750 m at C which was noted from the visual inspection of the temperature records and is most probably due to the erratic advection of South Atlantic Intermediate Water elements. The vertical structure of the temperature time scales is more complex at B, and as we shall see later, so are the vertically coherent structures of temperature variability. The mid-water minimum time scale, for example, is in the Mediterranean water mass. At 500 m, the 33 day time scale at C is half of the 62 day scale at B, indicating that the baroclinic oscillations are much longer at B.

Velocity time scales in general are shorter than the temperature scales. In B, as in temperature, the velocity time scales are variable with depth and in A, as in temperature, these are uniform with depth. In Cluster C, the east-west time scale is nearly twice as long as in the north-south direction and is also variable among the moorings in the cluster. We found that in all clusters, quite different four month to twelve month changes

of progressive vector diagram patterns would occur at various moorings and various depths.

The correlation coefficient of the daily records as a function of horizontal separation is graphed on Figure 9 for all three clusters. At A and B, the most coherent level for velocity is 1500 m where we estimate a coherence scale of 100-150 km. At 200 m the scale is 50-100 km and at 4000 m it is less than 50 km. The temperature coherence scale at 200 m, 500 m, 2800 m, and 4000 m is similar at each mooring, about 200 km. At 1500 m, the horizontal coherence scale of temperature is significantly smaller in B (100 km) than at A (150 km). These estimates are based on the premise that the variations are isotropic in A and B.

A display of the correlation coefficient of the v' component at 500 m in Cluster C is on Figure 12b (the t=0 graph; see section III F). It is apparent that the east-west scale is shorter, about 100 km, than the north-south scale which is not resolved by this array. The eddy field is clearly not isotropic.

D. Kinetic and potential energy distribution

The cluster averages of the eddy kinetic energy and the eddy potential energy are shown in Table 3. Both quantities are computed from the daily fluctuation records of u', v', T' of eastward and northward fluctuation velocity and temperature, respectively, using the formulas K.E.'= $\frac{1}{2}\overline{(u'^2 + v'^2)}$ and P.E.'= $\frac{1}{2} N^2 \overline{T'^2} (dT/dz)^2$. Here N is the Vaisala frequency and (dT/dz) is the temperature gradient computed from the C.T.D. casts during the recovery cruise at each mooring (see section II). For comparison, similar quantities for the MODE area and POLYMODE Array I are also presented. These fall roughly on the same latitude circle as Clusters A and B (see Figure 1). On Table 3, a cluster average quantity is computed at levels where two or more complete records of a variable are available (335 days in A and B and 353 days in C). Because there are at most 4 complete records of any quantity at any specific level, an estimate of the significance of the cluster mean is not attempted. Bracketed quantities are the cluster mean values in which individual values vary within a cluster by more than a factor of two. Specific note is made of exceptional levels of K.E.' or P.E.'.

Quite clearly, the kinetic and potential eddy energy at 500 m along the 28°N latitude band first decreased eastward from MODE C to the western foot of the Mid-Atlantic Ridge and then increases to Cluster A; the potential energy continues to increase across the Ridge to Cluster B. The Cluster C K.E.' and P.E.' at 500 m are of intermediate magnitude compared to the 28°N values. At 1500 m, K.E.' at Cluster A and B is less than at MODE C, and is comparable to MODE E. However, the apparent P.E.' at A and B is three times larger than the

value at MODE E.

The temperature variances at 1500 m at Cluster A is due to a smooth low-frequency signal in the records. Because water mass variability there is not apparent in the CTD traces, we interpret our computed P.E.' as a good measure of the actual eddy potential energy. However, at Cluster B all five 1500 m records show a ragged high-frequency temperature variability. We are not sure how much of this temperature variance is due to vertical motions (and hence associated with potential energy) and how much is due to the horizontal advection of heterogeneous elements of Mediterranean Water. It is interesting to note that at 1500 m, K.E.' at Cluster B is double that of A. This increase probably reflects the general eddy energy increase in the upper layers on the eastern flank of the Mid-Atlantic Ridge rather than the K.E.' due to Mediterranean water mass elements. Finally, at 4000 m, the K.E.' and P.E.' seem to be controlled by both bottom roughness and the upper level variability. MODE E and Cluster C are in moderately rough bottom areas and the bottom energy levels are comparable. Clusters A and B exhibit a more drastic vertical decay of energy to the rough bottom than occurs at MODE E or Cluster C. Evidence for increase of P.E.' near the bottom is seen at Cluster A and most dramatically in both K.E.' and P.E.' at mooring #79, Cluster C.

In Array III we obtained, for the first time in POLYMODE, long records at the top of the main thermocline, between 120 and 215 meters. In each cluster three long current records exist. There

is at most a 10% variation in K.E.' among the separate moorings in each cluster. At all three clusters K.E.' decreases with increasing depth through the main thermocline although this is less dramatic at C. At each upper level instrument in Clusters A and C, $\overline{v'^2} > \overline{u'^2}$ and Cluster B $\overline{u'^2} > \overline{v'^2}$. Also at Cluster A and C the spatial inhomogeneity of P.E.' within the cluster is larger than B. At Clusters A and C there is a maximum value of P.E.' at the surface. Furthermore, at each mooring in C, P.E.' decreases with increasing depth and then increases again to a maximum between 320-540 m (see Figure 10) but the exact vertical distribution is somewhat different at each mooring.

A byproduct of the historical density field calculations done in section II are eddy potential energy profiles. Those calculations attempted to explain the density variance at a depth as being due to constant horizontal gradients of density, $\overline{\rho}_x$ and $\overline{\rho}_y$, balanced (through the thermal wind relations) by a mean vertical shear. Naturally, all of the density variance cannot be explained this way. Some of the residual variance will be due to error, and some due to vertical fluctuations around the mean depth. Figure 10 shows the inferred eddy potential energy at Cluster C from:

$$\text{P.E.}' = \tfrac{1}{2} \frac{\rho'^2}{\rho_z} N^2 = \tfrac{1}{2} \frac{g^2}{\rho_o^2} \frac{\rho'^2}{N^2}$$

where ρ'^2 is the density residual at each depth. Also shown are the estimated energies from the temperature records and their

average. The maximum at 300 m appears to be a real feature.

At each instrument at Cluster C, except 300-500 m level on #81, $\overline{v'^2} > \overline{u'^2}$. At A, there appears to be a uniform vertical decrease of P.E.' . However, because of the vertical sampling, we do not know whether a relative maximum occurs between 500 m and 200 m as there is at C. At B, the near surface value of P.E.' is less than that at the 500 m level. At A and C the thermal field variance in the upper portion of the main thermocline is horizontally more inhomogeneous than at B, while below the main thermocline it is more inhomogeneous at B than at the other two clusters.

In summary, in Array III the mid-water K.E.' and P.E.' are comparable to central MODE region values. There is a relative increase of K.E.' from 500 m to the 200 m level and, over rough topography, a sharp decrease of both K.E.' and P.E.' to the ocean bottom. The horizontal inhomogeneity of the P.E.' distribution in and above the main thermocline is observed where there is a north-south polarization of the low-frequency currents. In some moorings there is bottom trapping of P.E.' and K.E.'.

E. Eddy Temperature Fluxes

If the eddy field is locally converting mean potential energy of the main thermocline to eddy energy, the horizontal eddy density flux (or eddy temperature flux, $\overline{\vec{v}'T'}$) has a component opposite the direction of the mean horizontal density gradient (or mean temperature gradient ∇T). We computed the eddy temperature transports at all instruments with long records. Significant fluxes (correlation coefficient between $\vec{v}'$ and T' greater than 0.3) that are consistent within a cluster occur between 160 m and 500 m in Cluster C and at the 1500 m level on three westernmost moorings in Cluster B (#623, 626, 627). We also computed the cospectra between the time series of $\vec{v}'$ and T' and find that when consistent fluxes (or correlation coefficients) occur, the contributions to these comes from 60-20 day period variable components of the time series. Recall that between 150 m and 500 m at Cluster C there is a well defined water mass, and at 1500 m, in Cluster B, the water mass variability occurs at relatively much higher frequencythan the frequency band from which we obtain the significant covariance contributions. On Figure11 the heat flux vectors and the velocity variance ellipses at 500 m in C and 1500 m in A and B are plotted. The estimate of the direction of the historical density gradient at 500 m in C (see Table 1) and the vertically averaged horizontal density gradient between 1000 m and 2000 m at A and B are also plotted. In the upper layers of Cluster C the cluster averaged eddy heat flux, although marginally significant at the 90% level, is to the northeast, and the historical density gradient is at precisely right angles to this flux! At moorings

#80 and #82 there is a conversion to eddy potential energy, and at moorings #81 and #79 the conversion is in the opposite sense and of the same magnitude. The very low frequency, or secular scale, variation in the east-west direction at mooring 81 is more intense than at the other moorings and this results in an east-west oriented variance ellipse.

In Cluster B we estimate that the temperature flux vector is directed to the southeast, in the opposite direction of the density gradient, indicating a decaying eddy field. The Cluster A picture is not quite so clear but seems to indicate a neutral or slightly decaying eddy field.

It is interesting to postulate how rapidly eddies could convert potential energy to kinetic energy if conditions at each mooring in Cluster C were viewed individually. At mooring #82 there is a well developed shear of mean currents through the thermocline to the southwest and an eddy temperature flux to the southeast (correlation coefficient of 0.6 between $\vec{v}'$ and T'). Here an estimate of the local rate of eddy conversion in a geostrophically balanced mean current of shear $\partial v/\partial z$ is $\frac{\alpha g f}{\rho_o N^2} \frac{\partial v}{\partial z} \overline{v'T'}$ where $\overline{v'T'}$ is the component of the temperature perturbation flux projected to the left of the mean shear, $\alpha = (d\sigma/dT)$, taken from CTD casts near mooring #82, f is the Coriolis parameter, g is the gravitational acceleration and N is the Brunt-Vaisala frequency. Between 300 m and 500 m at mooring #82 with the values $\frac{\alpha g \overline{v'T'}}{\rho_o} = 0.1$ cm $\sec^{-3}$, $\partial v/\partial z = 1.0 \times 10^{-4}$ $\sec^{-1}$, $f = 4.0 \times 10^{-5}$ $\sec^{-1}$, and $N^2 = 3.1 \times 10^{-5}$ rad/sec^2,

this conversion rate is 1.3×10^{-5} cm^2 sec^{-3}. The average of K.E.' + P.E.' at these levels is 76.4 cm^2 sec^{-2}, giving a time scale for doubling the local eddy energy level of about 68 days. The ocean shear is varying on a secular time scale, long compared to an eddy period. Therefore, eddies can be created at Cluster C very locally where the ocean shear is favorable for their creation for a few months. It is not surprising that we observe spatial inhomogeneity of the eddy potential energy statistics and eddy temperature fluxes in the upper ocean in the Cluster C area. It is the large mean shears and occasional large temperature fluxes that indicate that eddies could have been born in the vicinity of moorings #82 and #80 during this observational period.

F. Horizontal and Vertical Phase Propogation

Because the dominant fluctuations of each variable u, v, and T are generally spatially correlated within each cluster (except at nominal depth of 4000 m in Clusters A and B) we can investigate if there is any horizontal phase propogation. Displayed in Figure 12a are the correlation coefficients of the north-south (v) velocity component at 1500 m in Cluster B with different time lags. For a given time lag, the correlation coefficient is shown as a function of horizontal separation vector. With t = 0, the correlation coefficient is symmetric about the origin as it should be. Although it seems that the motion field is horizontally isotropic the array configuration is not adequate to confirm this in the north-west and south-east quadrants of the graph. When t increases, a southwestward propogation of the pattern of the correlation can be clearly seen, indicating that the v-velocity of the eddy field has a southwestward phase propogation with estimated phase speed about 3 km/day. Results for other variables, including those in Cluster A, show similar westward phase propogation with less clearly resolved north-south component.

The correlation coefficients of the v-velocity at 500 m in Cluster C is shown in Figure 12b. It is clear that the meridional scale is longer than the zonal scale. Westward phase propogation with speed about 3-5 km/day can be seen for small lags; correlation coefficients with large lags are probably not significant. Similar westward propogation was also found for temperature field, whereas no significant propogation was found for u-velocity field.

In interpreting the phase propogation observed in Cluster C,

we have to keep in mind that the mean flow at 500 m is also westward with a speed of 1-2 km/day. The apparent phase propogation may be partly due to the advection of a stationary perturbation by the mean flow but cannot be explained entirely by it. In all areas of Clusters A and B the mean flow at 1500 m is also about 1 km/day to the north-west and the observed phase propogation may be an intrinsic property of the eddy field. South-westward propogation with speed about 4 km/day was also observed in the MODE area (The MODE Group, 1978).

One of the features of linear baroclinic instability models is the prediction of upward phase propogation (Gill, Green and Simmons , 1974). That is, variations at depth should lead those at a more shallow depth. Figure 13 is a contoured plot of deviation from the mean at each instrument in units of standard deviations. The meridional (v) velocity at mooring #81, Cluster C is shown. If there were no vertical phase differences then all lines would be either vertical (disturbances of equal relative amplitude) or a symmetrical "tent" shape (disturbances of unequal relative amplitudes). Careful inspection of the figure will show that the lines are generally bow shaped with the surface and deep instruments leading the mid-depth instruments. Spectral analysis confirms this and indicates that it is the low frequency (period greater than 30 days) that is experiencing the phase differences. Mooring #82 v velocity gives a similar picture. Temperature and u velocity, however, are more complicated; the former because of the lack of vertical coherence and the latter because the "bows" are curved in both directions.

G. Empirical Orthogonal Modes

The most weighted and vertically coherent variations are most simply viewed in terms of the empirical orthogonal modes (EOMs) of the vertical covariance matrix (Lumley, 1970). These are graphed on Figures 14 and 15 for the vertical displacement, $\xi' = T'/(\partial T/\partial z)$, and the horizontal velocity, $\vec{v}'$, respectively. The velocity modes are drawn so that the maximum vector is unity and the bottom vector is along the positive x axis. Cluster A, or Mooring 630, presents the simplest picture. Most of the variance is associated with the vertical displacement of the main thermocline, very much like a dynamical mode, and the second most energetic fluctuation is surface trapped. One velocity mode, which is quite baroclinic, accounts for 96% of the overall variance, but does not account for the variance in detail at 4000 m because the 1500 m and 4000 m currents are not correlated while those at the 200 m and 1500 m levels are.

In Cluster B, both at moorings #623 and #625, 96% of the variance field of velocity is also representative of a single velocity mode which looks identical to that at Cluster A. However, 98% of the variance in the displacement structure is represented by three modes: the most energetic one is bottom trapped (61%), the second most energetic mode (24%) resembles the most energetic mode in Cluster A. We also computed the displacement EOMs at the southernmost Cluster B at mooring #627, and here two modes (64% and 30%) are required to account for 94% of the variance, with significantly different shapes than in #623.

Cluster C has the most complex vertical structure. At mooring #81 (and also #79) three modes are required to represent 86% of the displacement variance (47%, 23%, 16% at mooring #81 and 65%, 21%, and 9.2% at mooring #79). Two modes are required to represent 95% of the velocity variance at both #81 and #82. The velocity modes are similar with nodes at nominal instrument depth 300 m.

Recalculation of the displacement EOMs without the records where spatial inhomogeneity is suspected (1500 m record at B and the 750 m record at C), does not significantly change the vertical structure or energy distribution of the modes. It is interesting to note that above 1500 m we observe a weak counterclockwise rotation with depth of the most energetic mode at all moorings.

IV. Conclusions

Array III was set for largely descriptive purposes; i.e. to define the geographical variability of mesoscale variability in the western North Atlantic. We have seen that as compared to the MODE area, Cluster A, located just west of the mid-Atlantic Ridge, has many of the same characteristics as that region. There is a tendency towards somewhat longer periods of motion. But the most striking difference (also seen at Cluster B) is the loss of energy in the deep water over rough topography.

Cluster B, located just east of the Ridge, is surprisingly different from A. Eddy heat fluxes indicate that it is in a region of decaying eddy energy whereas Cluster A appears to be in a more neutral region. The Mediterranean water has a more pronounced effect. The rapid transition in T-S characteristics here and the abrupt variability of the means is part of a puzzle having to do with the interactions of the water masses, topography, and the eddy field that we have not begun to sort out.

Cluster C, in the North Equatorial Current, has a more complex variability than we anticipated. The idea that this area should exhibit a comparatively simple form of baroclinic instability has not been borne out.

As noted earlier by Schmitz (1976,1978) and Richman, et. al. (1977), the gross energy variations of the mid and upper ocean remain consistent with a general intensification toward the

Gulf Stream, with secondary maxima toward other boundaries. There seems to be a broad minimum of eddy kinetic and potential energy in the thermocline centered at around 28°N that is consistent with Dantzler's(1977) potential energy diagram. However, there is no justification for calling this region an "eddy desert" as there is only a quantitative, not a qualitative change in energy levels over the North Atlantic.

Bryden, H.L. 1976. Horizontal advection of temperature for low-frequency motions. Deep-Sea Research, 23, 1165-1174.

Dantzler, H.L., Jr. 1977. Potential energy maxima in the tropical and subtropical Atlantic. J. of Phys. Oc., 7, 512-519.

Fu, L-l., and C. Wunsch. 1979. Recovery of POLYMODE Array III Clusters A and B. Polymode News, No. 50 (unpublished manuscript) Woods Hole Oceanographic Institution, Woods Hole, Mass.

Gill, A.E., J.S.A. Green and A.J. Simmons. 1974. Energy partition in the large-scale ocean circulation and the production of mid-ocean eddies. Deep-Sea Research, 21, 499-528.

Koblinsky, C.J., T. Keffer and P.P. Niiler. 1979. A compilation of Observations in the Atlantic North Equatorial Current. Oregon State University, Reference 79-12, 119 pp.

Lumley, J.L. 1970. Stochastic Tools in Turbulence. Academic Press, 194 pp.

Mazeika, P.A. 1973. Circulation and Water Masses East of the Lesser Antilles. Deutsche Hydrographische Zeitschrift, 26, 49-73.

Richman, J.G., C. Wunsch, and N. Hogg. 1977. Space and time scales of mesoscale motion in the Western North Atlantic. Rev. Geophys. Space Phys., 15, 385-420.

Schmitz, W.J., Jr.. 1976. Eddy kinetic energy in the western North Atlantic. J. Geophys. Res., 81, 4981-4982.

Schmitz, W.J., Jr. 1978. Observations of the vertical distribution of low frequency kinetic energy in the Western North Atlantic. J. Mar. Res., 36, 295-310.

Suarez, A. 1971. The propagation and generation of topographic oscilations in the ocean. Ph.D. thesis, Massachusetts Institute of Technology.

The MODE group. 1978. The Mid-Ocean Dynamics Experiment. Deep-Sea Res., 25, 859-910.

Thompson, R.O.R.Y., and J.R. Luyten. 1976. Evidence for bottom-trapped topographic Rossby waves from single moorings. Deep-Sea Res., 23, 629-635.

Cluster	Depths	Observed (cm/sec) Δu (east)	Δv (north)	Geostrophically derived (cm/sec) Δu (east)	Δv (north)
A	200-1500m	-0.3 0.6*	-1.1 -1.1	-1.0±.4	-1.4±.4
B	200-1500m	-1.3	-1.4	-0.7±.4	-0.7±.4
C	180-500m	-4.8	-0.8	-2.7±.2	-1.1±.2

Table 1. Observed and computed velocity differences. Starred (*) quantities are estimates from the site mooring (#643) at Cluster A (May 1978 to September 1979).

Depth Range	POLYMODE - IIIA (28°N, 48°W)			POLYMODE - III B (27°N, 41°W)			POLYMODE - III C (16°N, 54°W)		
m	u	v	T	u	v	T	u	v	T
120-215	26	30	42	(62)	(44)	26	(34)	21	30
230-260									43
320-340							(45)	20	41
480-540			(41)			(62)	(51)	19	33
660-850									20
1420-1530	32	35	50	(52)	68	23			39
2440-2830							52*	33*	35*
3400-4040	(26)	(23)	(47)	(20)	(14)	37*	(34)	29	(33)

* - two record average.

Table 2

	POLYMODE - III A		POLYMODE - III B		POLYMODE - III C		POLYMODE - I		MODE - C		MODE - E	
	($28^{o}N$, $48^{o}W$)		($27^{o}N$, $41^{o}W$)		($16^{o}N$, $54^{o}W$)		($28^{o}N$, $55^{o}W$)		($28^{o}N$, $67.7^{o}W$)		($28^{o}N$, $68.7^{o}W$)	
Depth Range m	K.E.'(cm^2sec^{-2})P.E.'		K.E.'(cm^2sec^{-2})P.E.'		K.E.'(cm^2sec^{-2})P.E.'		K.E.'(cm^2sec^{-2})P.E.'		K.E.'(cm^2sec^{-2})P.E.'		K.E.'(cm^2sec^{-2})P.E.'	
120-215	54.9	(74.0)	73.2	21.8	31.7	72.6						
230-260						40.7						
320-340					21.3	65.5						
480-540		35.7	35.9*	55.6	26.5	39.4	9.0	10.0	39.5	32.0	33.0	22.5
660-850			26.5+			39.7						
1420-1530	1.8	23.0	4.0	(15.2)		5.4			7.4		3.1	
2440-2830		3.0		(11.4)	5.3	3.7						
3400-4040	1.0	4.8	(0.9)	(2.2)	(4.0)*	1.6*	0.5	0.8	8.6	11.0	7.4	5.2
			*#624 only +#623 only		*with#79 (6.6)	*with#79 (2.3)						

Table 3

CAPTIONS

Figure 1. Location of the POLYMODE moored arrays. Array III consisted of Clusters A, B, and C.

Figure 2. Local bathymetry and mooring locations of the three clusters of Array III, drawn for NAVOCEANO maps.

Figure 3. Superpositions of the T-S relation of each mooring in the three clusters. Also shown is the nominal depth of the current meters (▲) and P/T recorders (•).

Figure 4. Brunt-Vaisala profile at a mooring in each of the three clusters. The profile was calculated by determining the slope of a line that was fit through the vertical density field.

Figure 5. The location of the 2096 NODC bottle stations constituting the 700 m data set. The 100 m and 300 m sets would include additional points as well as the ones shown.

Figure 6. The σ_t field at three different depths along with the observed mean shear. (a) σ_t at 100 meters. 3033 stations were used to draw this estimate. (b) σ_t at 300 meters. 2441 stations were used. Also shown is the observed mean shear between 180 m and 500 m at Cluster C. (c) σ_t at 700 meters. 2096 stations were used. The observed mean shears between 200 m and 1500 m at Clusters A and B are also shown.

Figure 7. Temperature as a function of time at moorings (a) 630, (b) 623, and (c) 81. The raw records were low-pass

filtered with a half power cutoff of two days for moorings 630 and 623 and four days for mooring 81, then subsampled daily.

Figure 8. Daily stick diagrams at moorings (a) 629, (b) 623, and (c) 81. The records were filtered as in Figure 7.

Figure 9. Correlation coefficient as a function of horizontal separation for (a) temperature, (b) u velocity, and (c) v velocity at Clusters A, B, and C.

Figure 10. Potential energy as a function of depth at Cluster C. The solid line was calculated from historical hydrographic data. The symbols mark observed potential energy from the Cluster C temperature data, the dashed line their average.

Figure 11. Variance ellipses for (a) Cluster A, 1500 m; (b) Cluster B, 1500 m; (c) Cluster C, 500 m. Also shown are the direction and magnitude of the observed eddy temperature flux (from the current meters) and of the mean density gradient ($\nabla\rho$) from the hydrographic data.

Figure 12. Correlation coefficient of north-south velocity component at (a) 1500 m in Cluster B and (b) 500 m at Cluster C, as a function of horizontal separation for six different time lags (T, in days). The intersection of the two coordinates is the origin. East is to the right. The interval between tic marks is 100 km. The lines of zero correlation (dashed lines) are subjectively drawn.

Figure 13. Deviations about the mean meridional (v) velocity in units of standard deviations as a function of time and

instrument number at #81, Cluster C. The record at each instrument had its mean removed and then was normalized by its standard deviation. This was then contoured. Vertical phase lags appear as sloping lines.

Figure 14. Displacement empirical orthogonal modes at moorings (a) 630, (b) 623, and (c) 81. Each mode has been normalized such that the eigenvector magnitude is 1.0. The percent of total energy of each mode is indicated.

Figure 15. The most energetic velocity (complex) empirical orthogonal modes at moorings (a) 629, (b) 623, and (c) 81. The vectors have been rotated so that the bottom vector lies along the x-axis and have been normalized so that the top vector has a magnitude of 1.0. Figure (d) is the second mode at mooring 81.

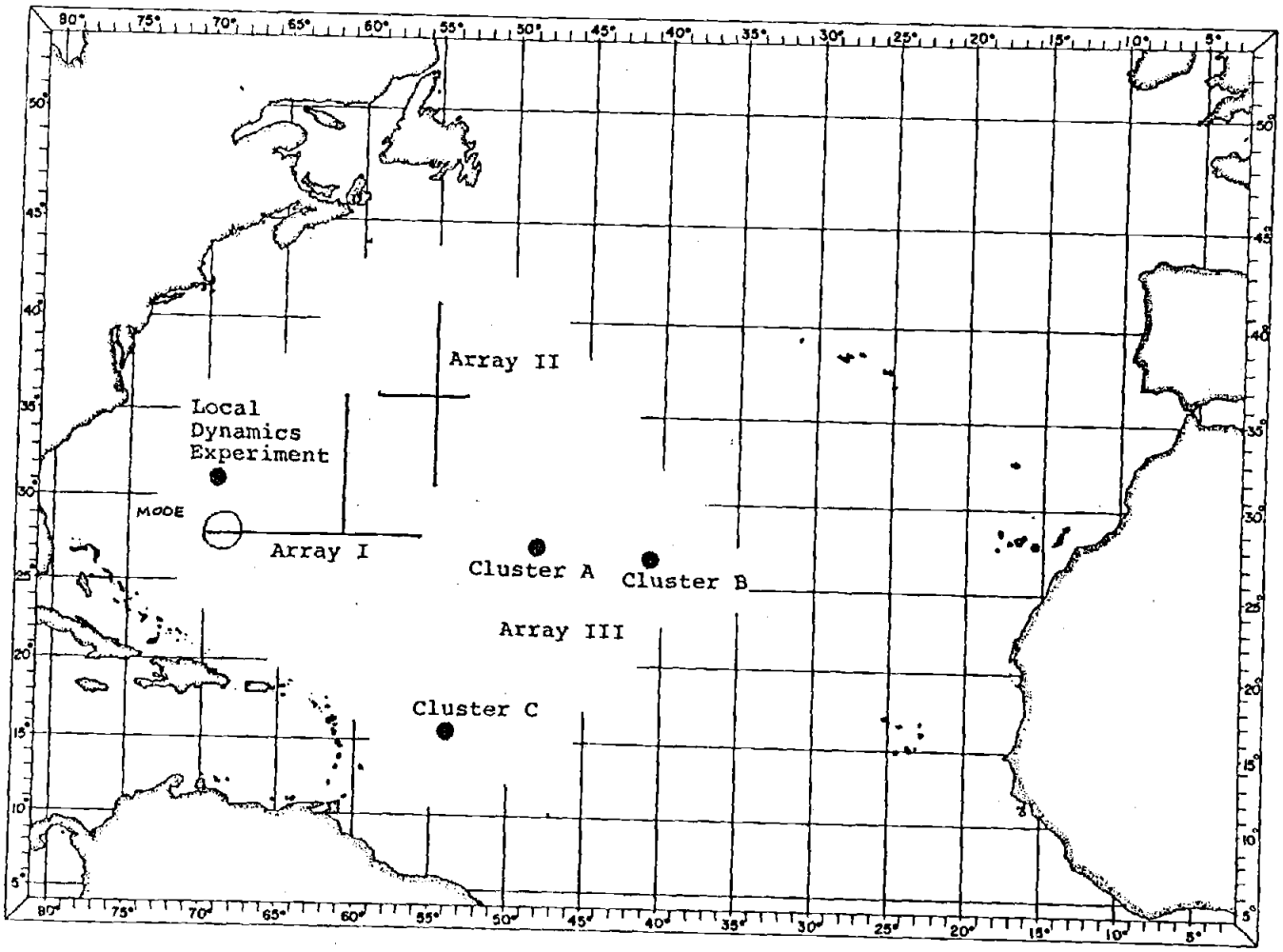
Array II
Local
Dynamics
Experiment
MODE
Array I
Cluster A
Cluster B
Array III
Cluster C

Figure 1

POLYMODE ARRAY III CLUSTER A BATHYMETRY

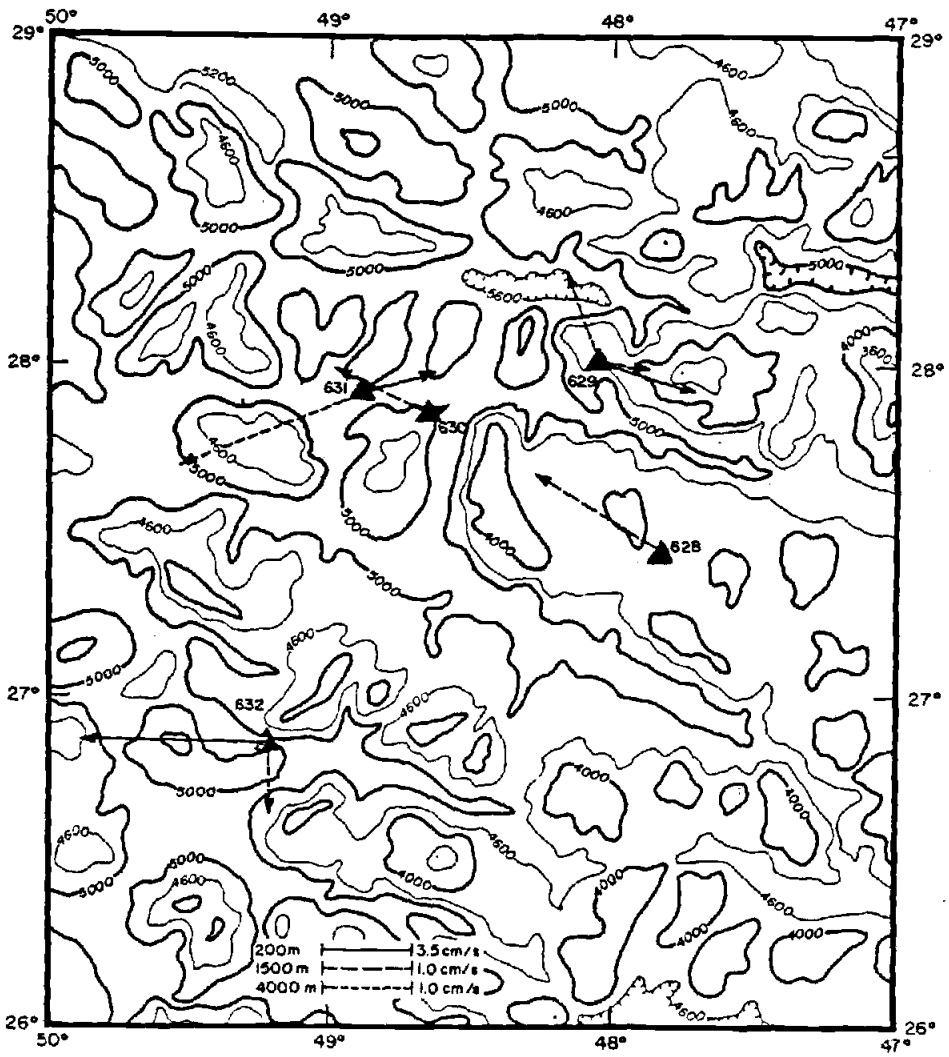

Figure 2a

POLYMODE ARRAY III CLUSTER B BATHYMETRY

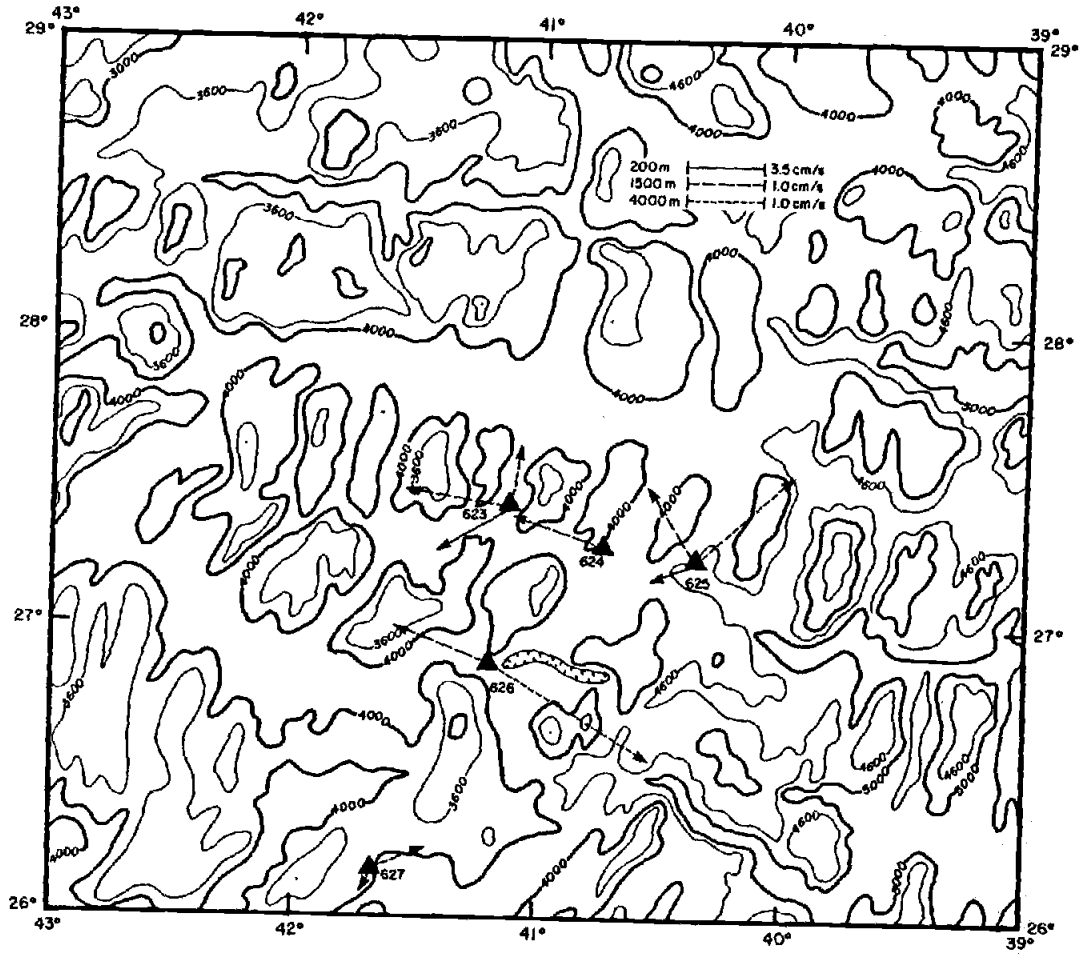

Figure 2b

POLYMODE ARRAY III CLUSTER C BATHYMETRY

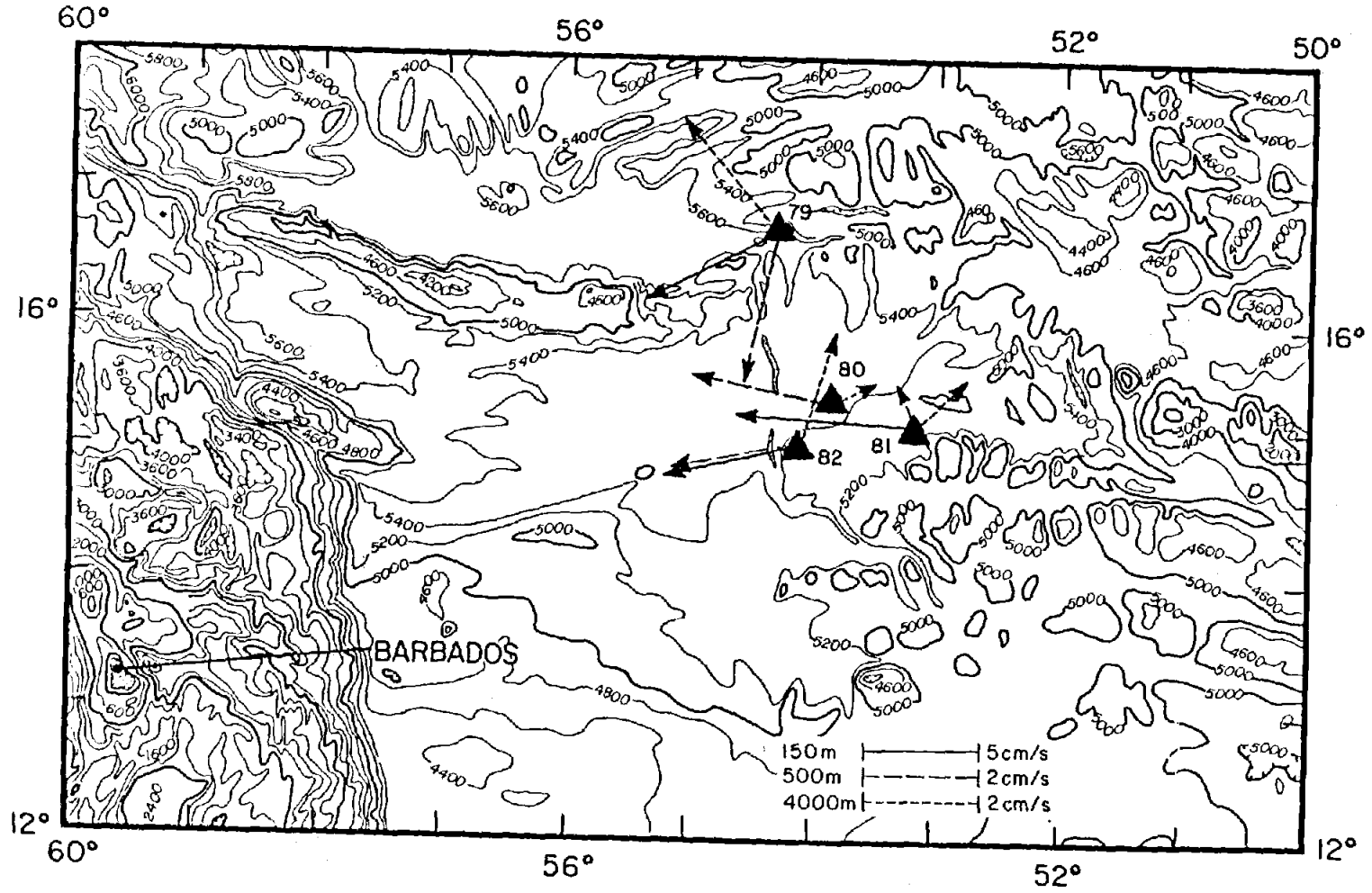

Figure 2c

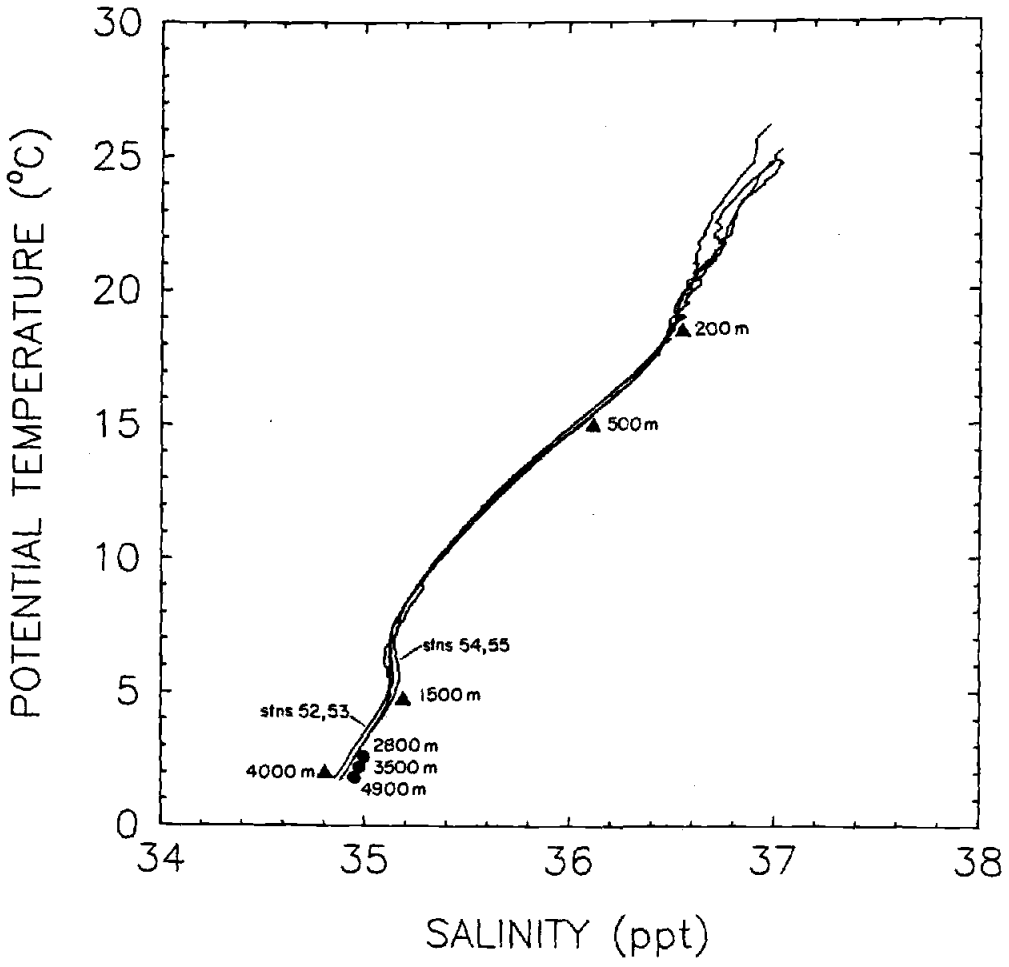

CLUSTER A

Figure 3a

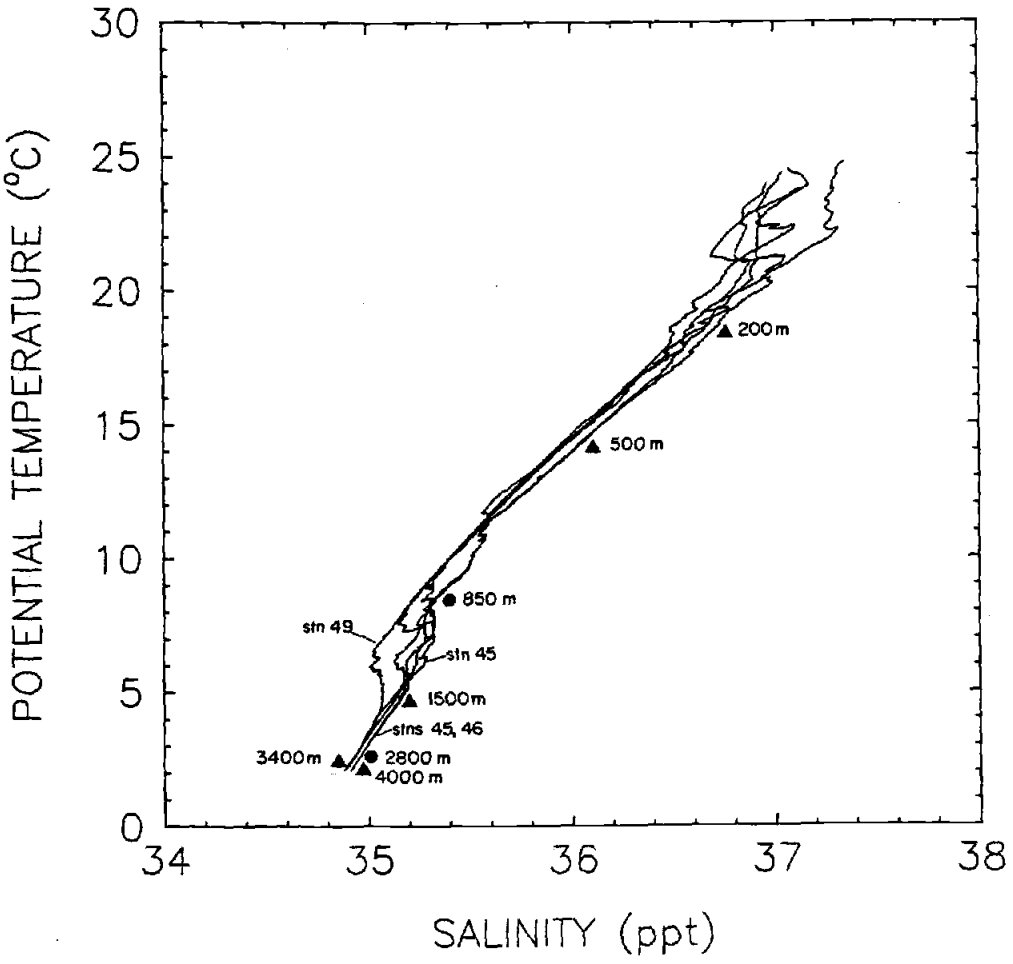

CLUSTER B

Figure 3b

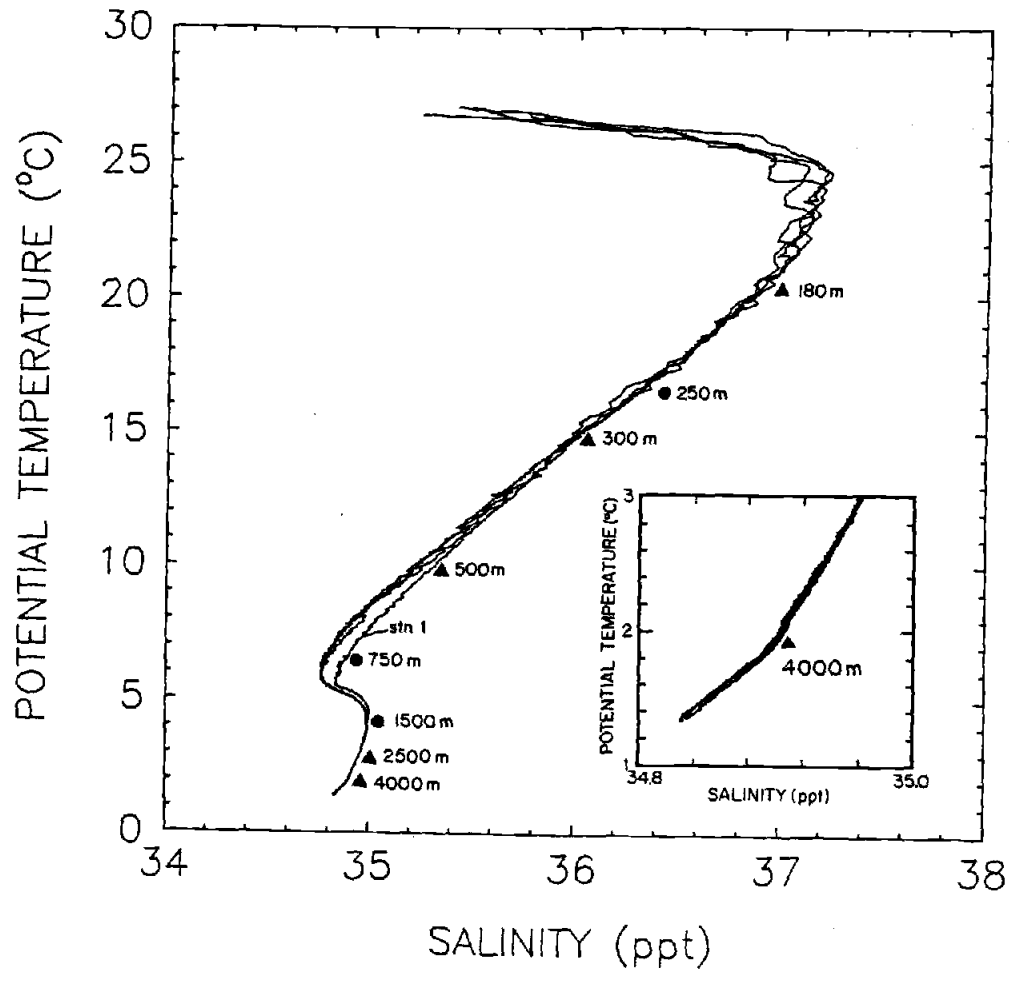

CLUSTER C

Figure 3c

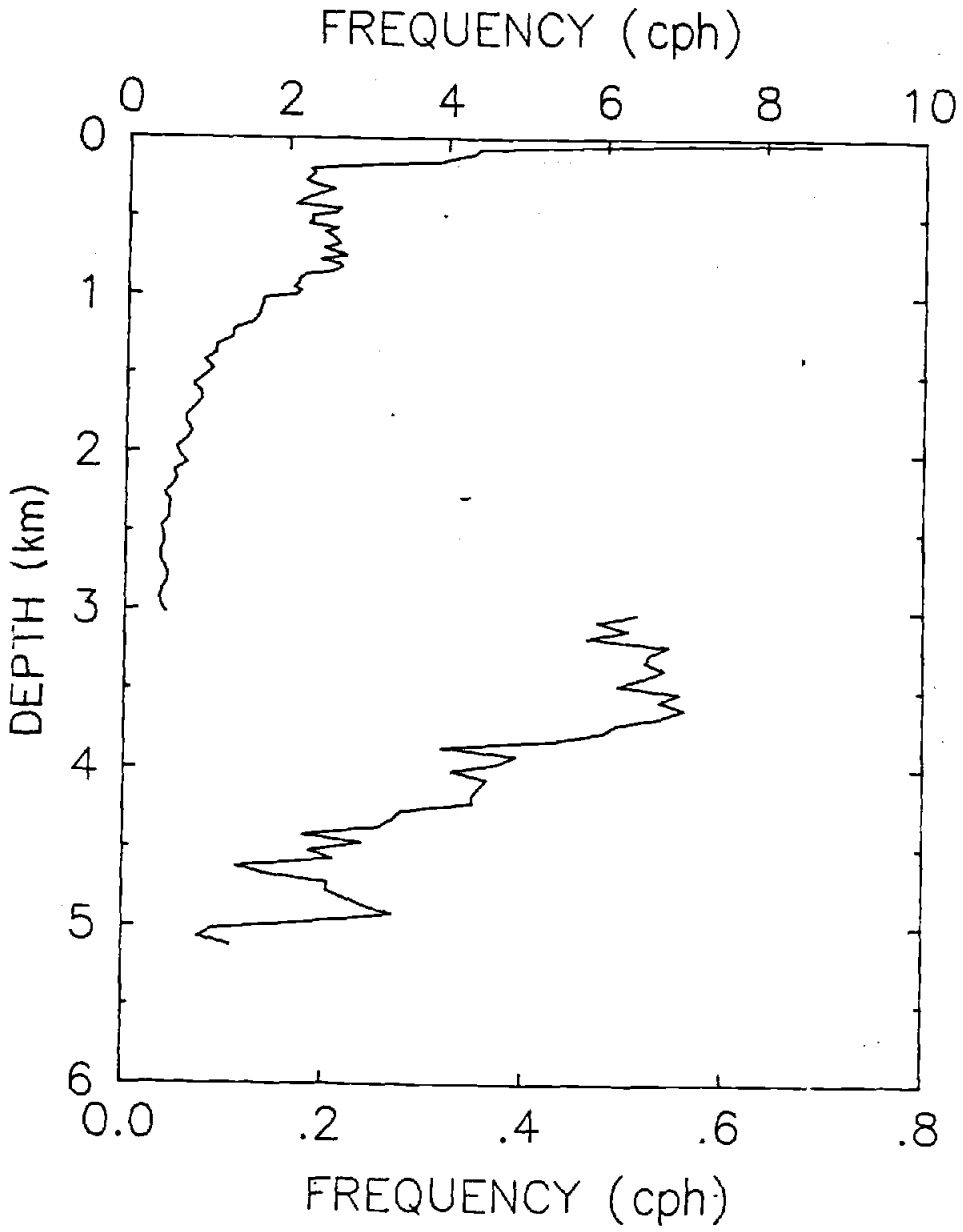

CLUSTER A — MOORING 630

Figure 4a

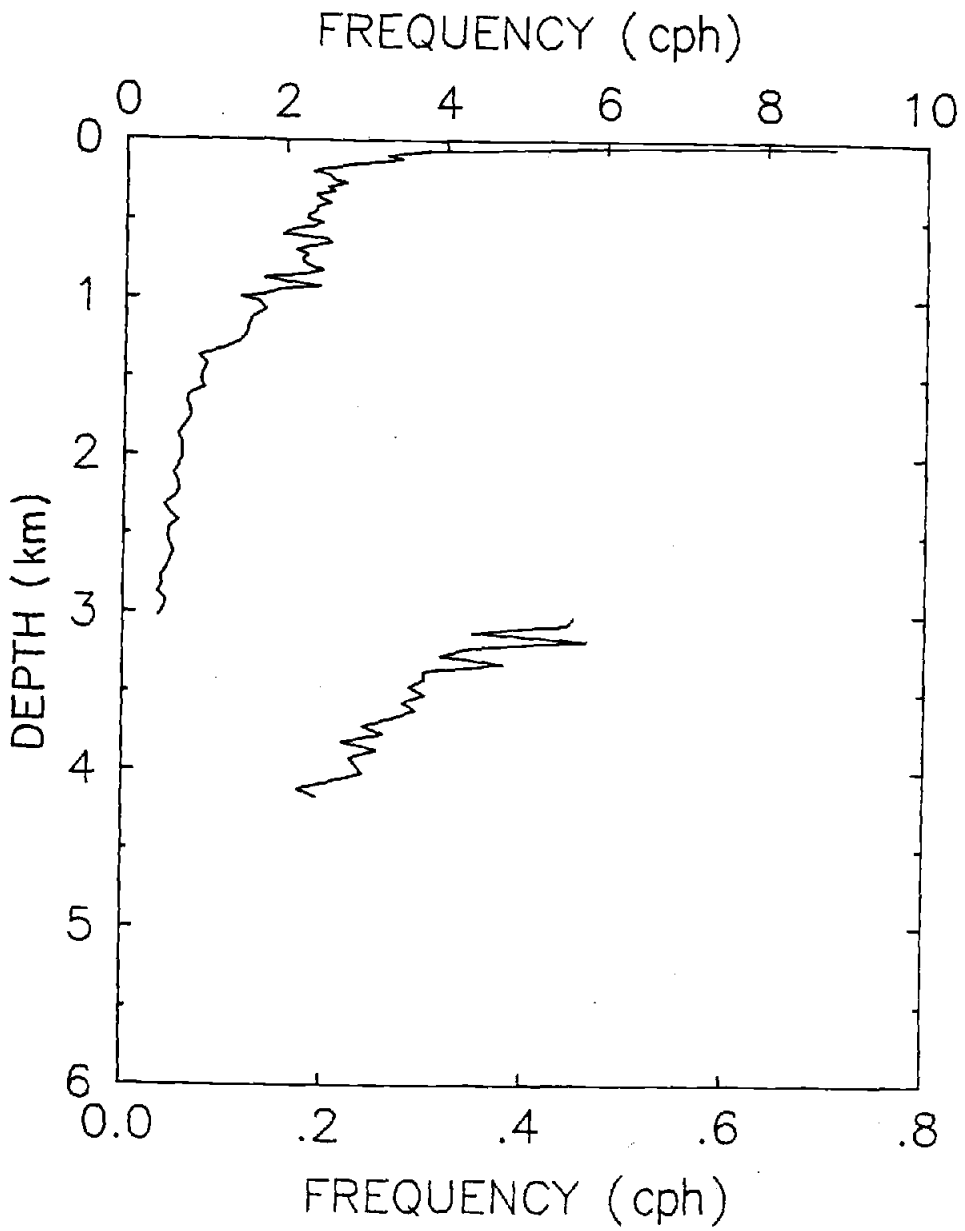

CLUSTER B – MOORING 623

Figure 4b

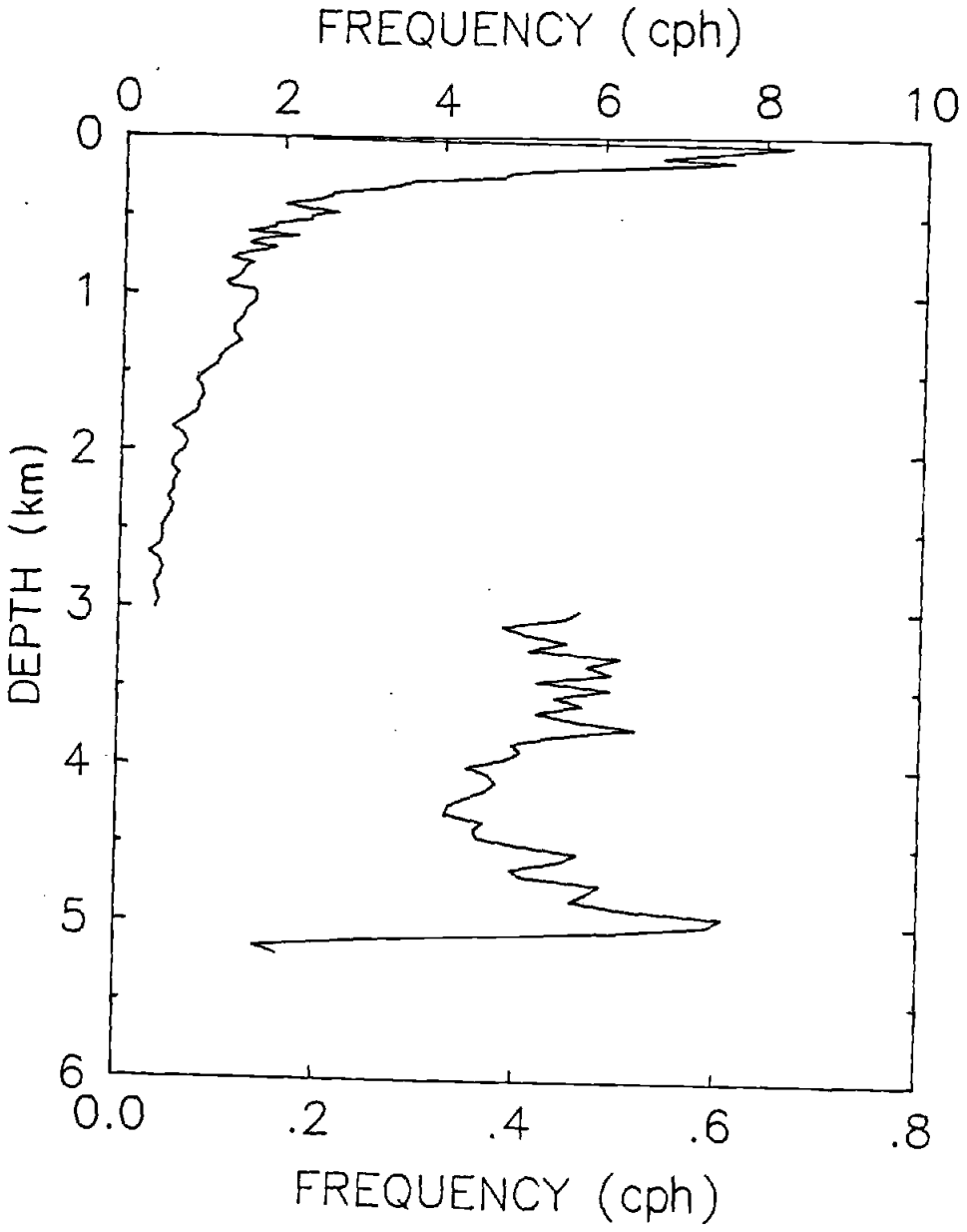

CLUSTER C – MOORING 81

Figure 4c

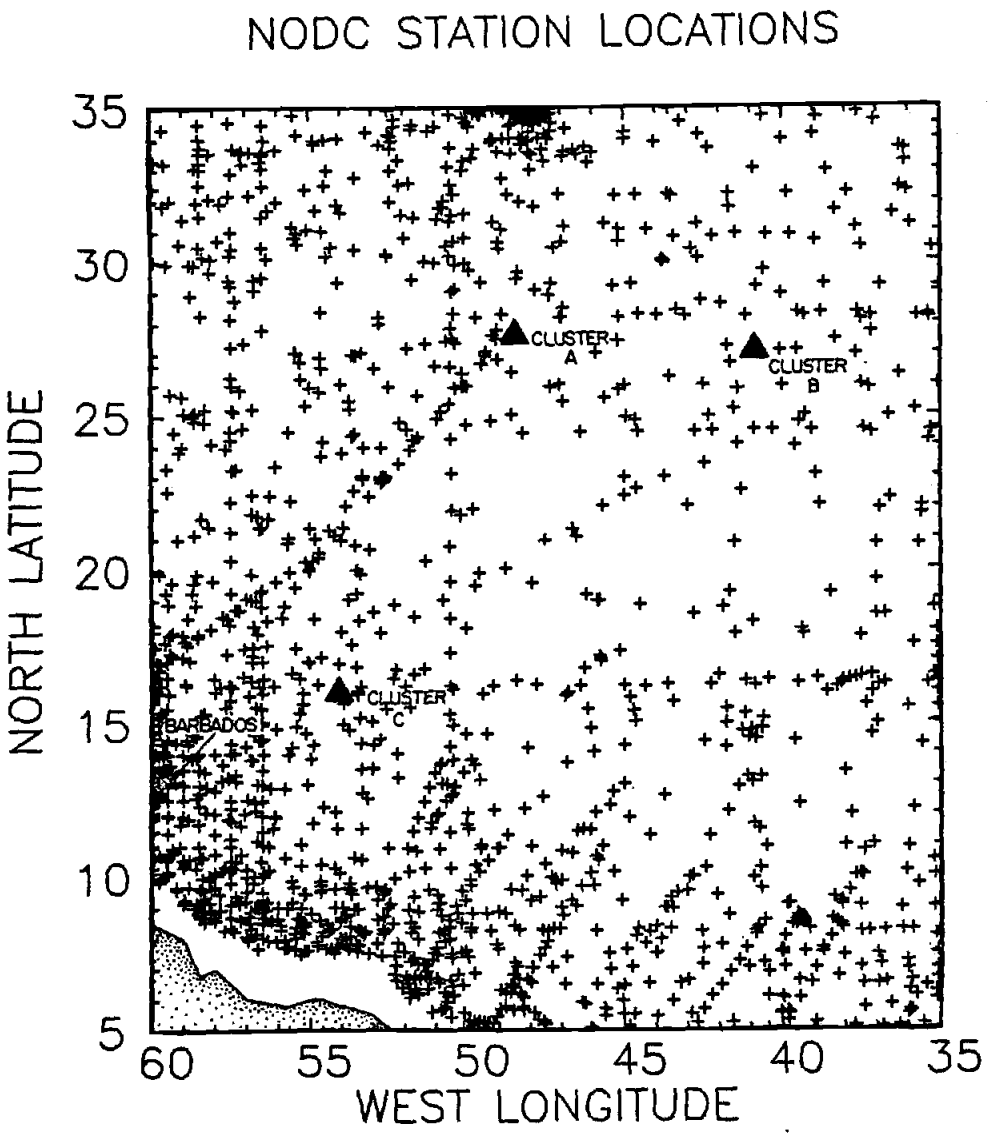
NODC STATION LOCATIONS
NORTH LATITUDE
35
30
25
20
15
10
5
60
55
50
45
40
35
WEST LONGITUDE
CLUSTER A
CLUSTER B
CLUSTER C
BARBADOS

Figure 5

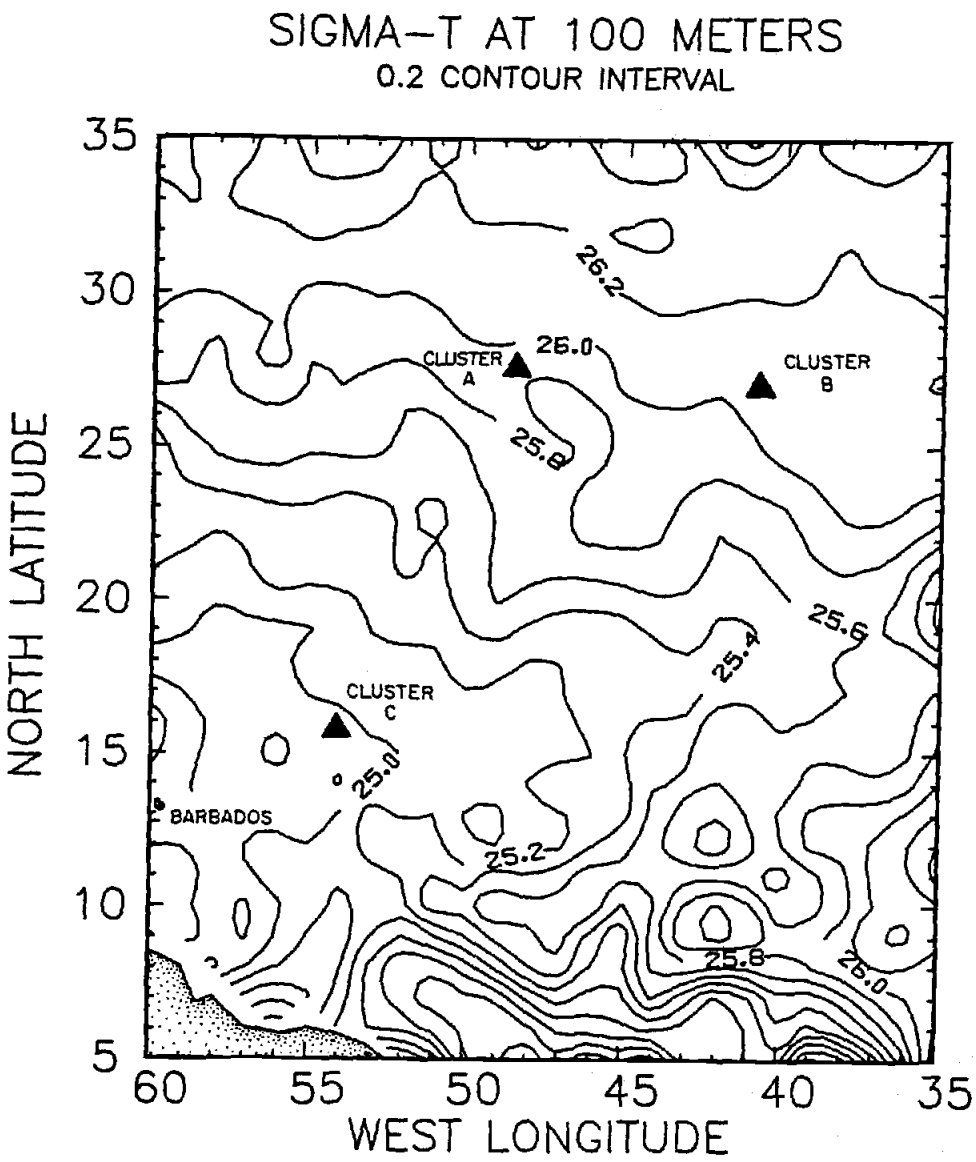
SIGMA–T AT 100 METERS
0.2 CONTOUR INTERVAL
NORTH LATITUDE
35
30
25
20
15
10
5
60
55
50
45
40
35
WEST LONGITUDE
CLUSTER A
CLUSTER B
CLUSTER C
BARBADOS
26.2
26.0
25.8
25.6
25.4
25.2
25.0
25.8
26.0

Figure 6a

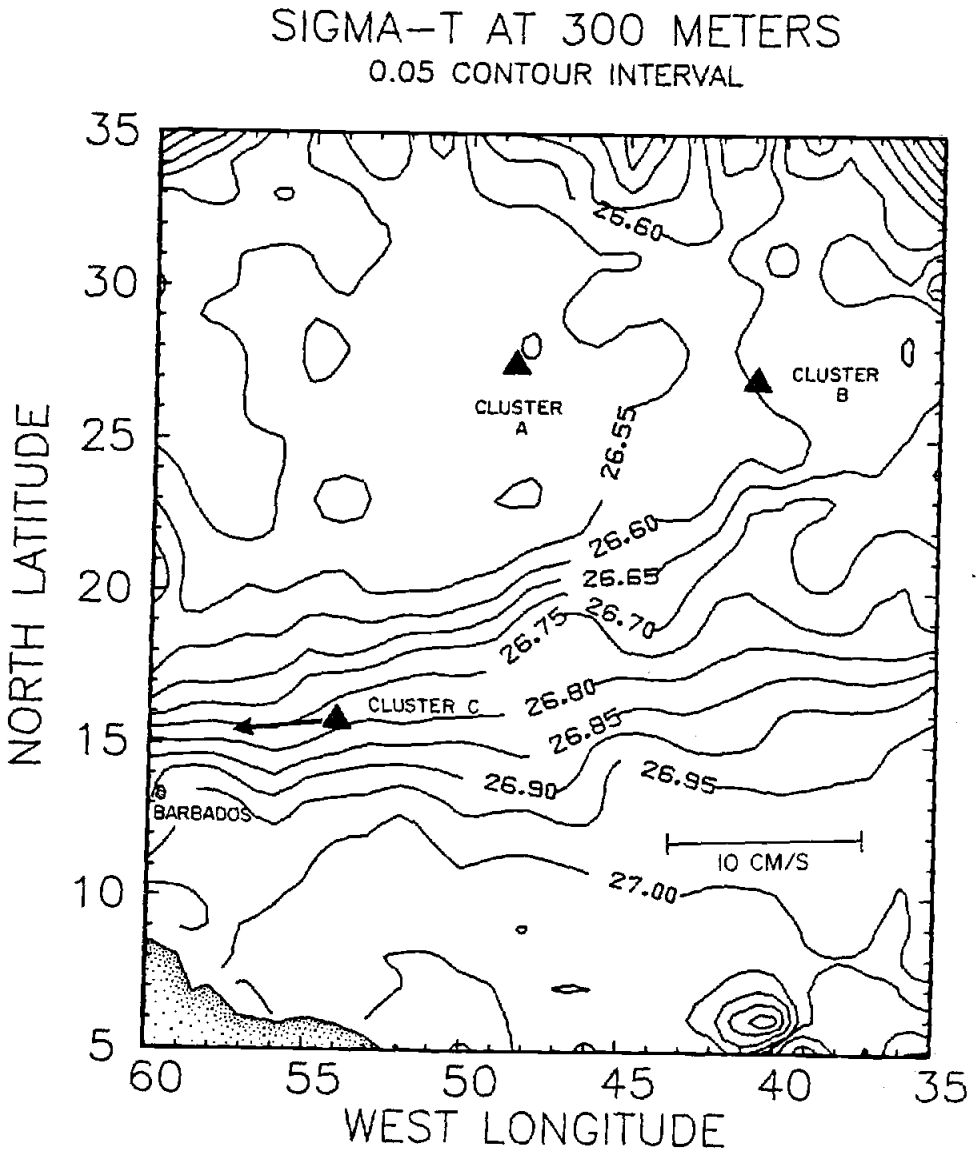
SIGMA–T AT 300 METERS
0.05 CONTOUR INTERVAL
NORTH LATITUDE
35
30
25
20
15
10
5
60
55
50
45
40
35
WEST LONGITUDE
CLUSTER A
CLUSTER B
CLUSTER C
BARBADOS
10 CM/S
26.60
26.55
26.60
26.65
26.75
26.70
26.80
26.85
26.90
26.95
27.00

Figure 6b

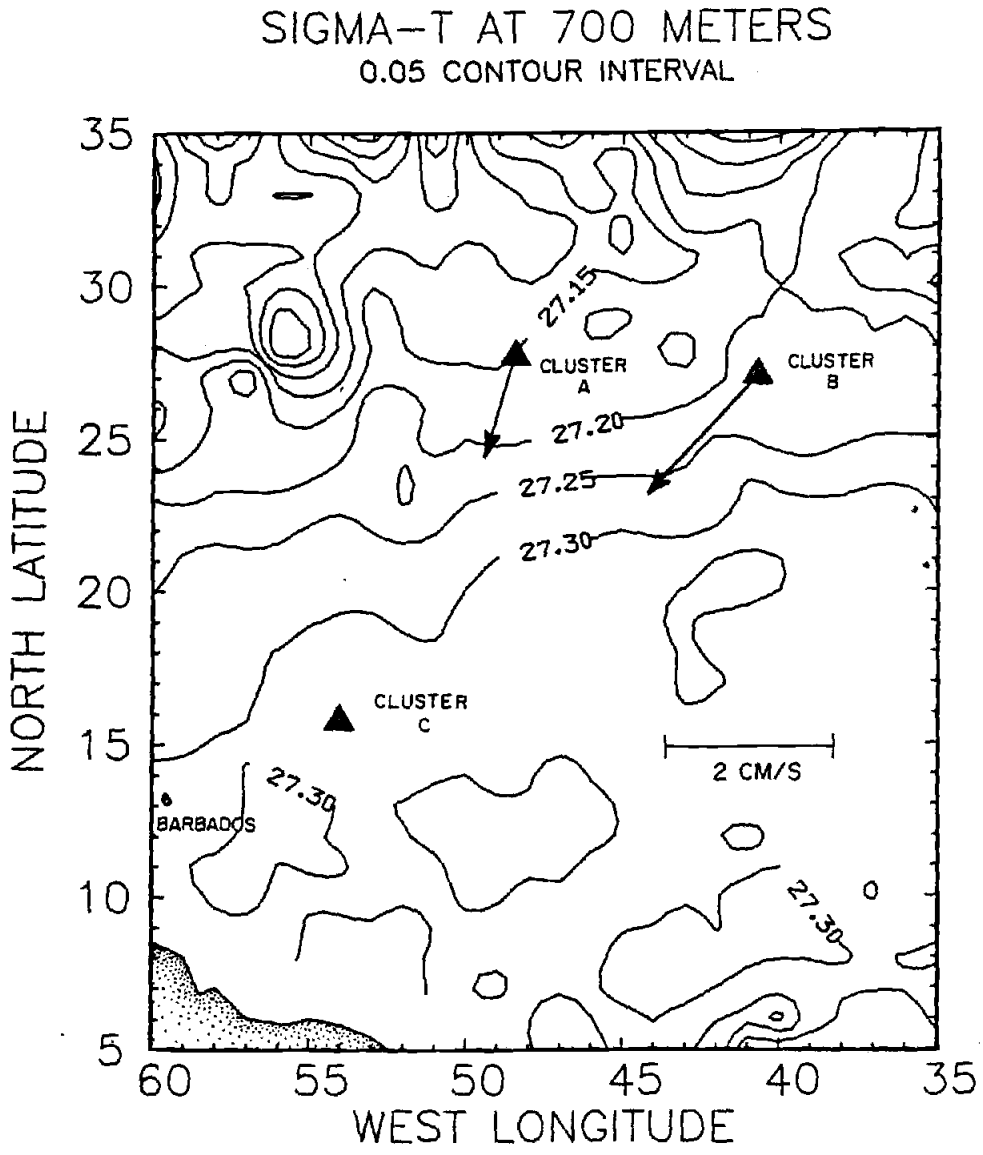
SIGMA–T AT 700 METERS
0.05 CONTOUR INTERVAL
NORTH LATITUDE
35
30
25
20
15
10
5
60
55
50
45
40
35
WEST LONGITUDE
27.15
27.20
27.25
27.30
27.30
27.30
CLUSTER A
CLUSTER B
CLUSTER C
2 CM/S
BARBADOS

Figure 6c

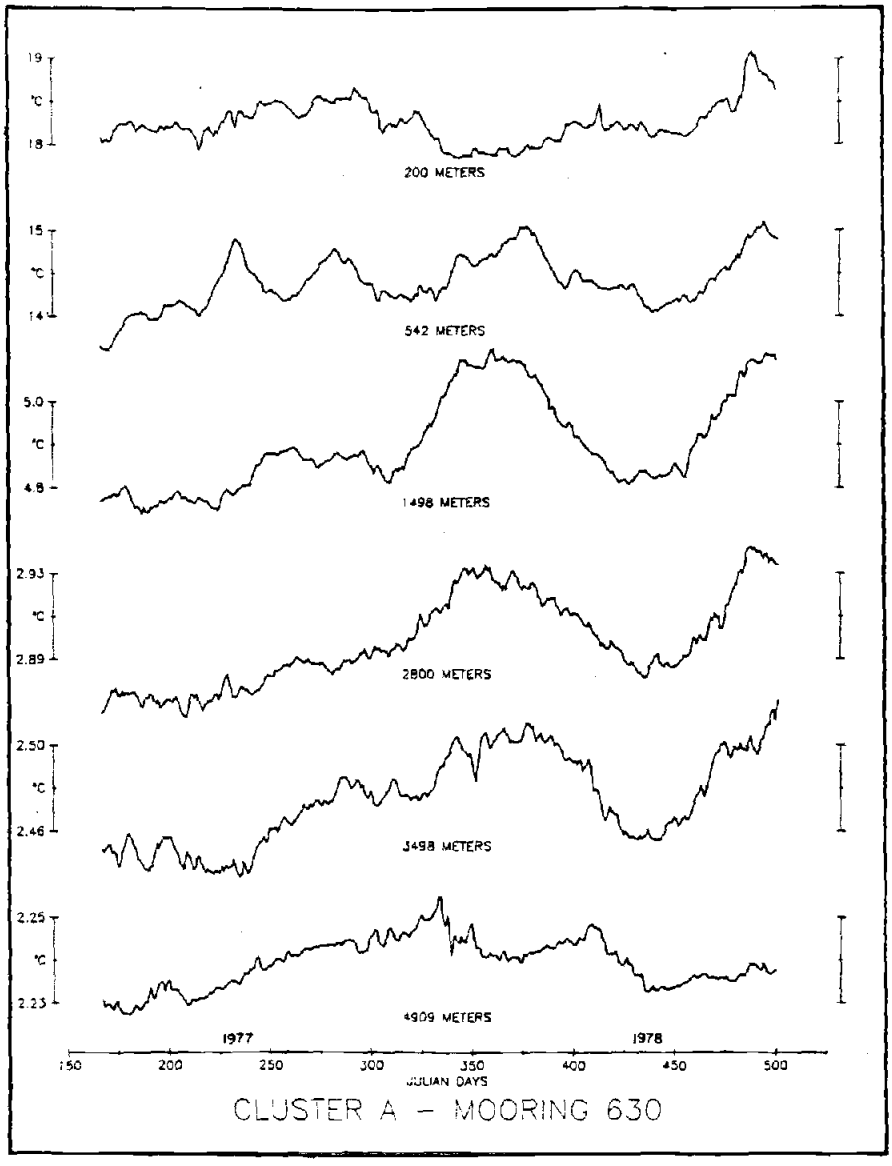
19
°C
18
200 METERS
15
°C
14
542 METERS
5.0
°C
4.8
1498 METERS
2.93
°C
2.89
2800 METERS
2.50
°C
2.46
3498 METERS
2.25
°C
2.23
4909 METERS
1977
1978
150
200
250
300
350
400
450
500
JULIAN DAYS
CLUSTER A – MOORING 630

Figure 7a

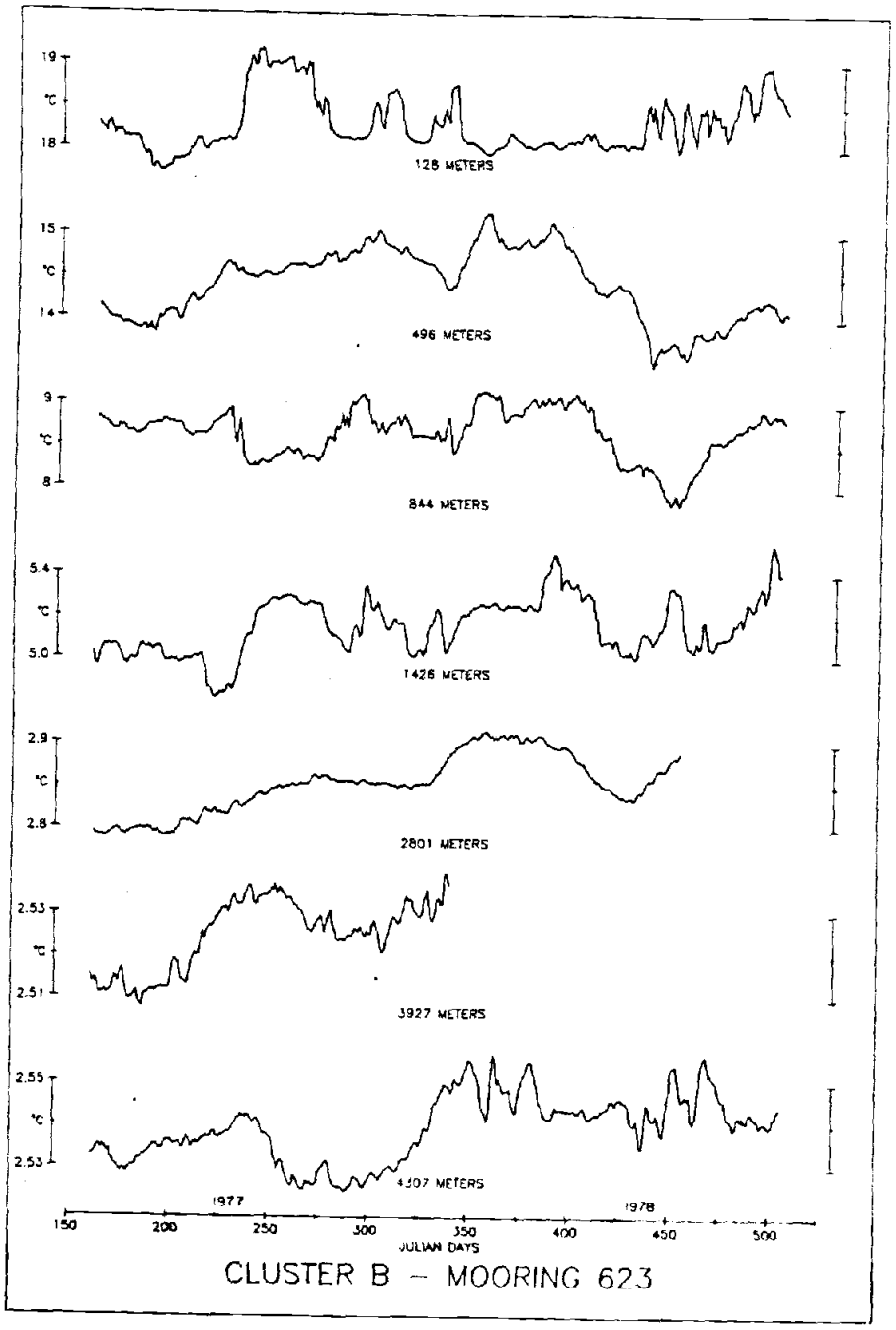
19
°C
18
128 METERS
15
°C
14
496 METERS
9
°C
8
844 METERS
5.4
°C
5.0
1426 METERS
2.9
°C
2.8
2801 METERS
2.53
°C
2.51
3927 METERS
2.55
°C
2.53
4507 METERS
1977
1978
150
200
250
300
350
400
450
500
JULIAN DAYS
CLUSTER B – MOORING 623

Figure 7b

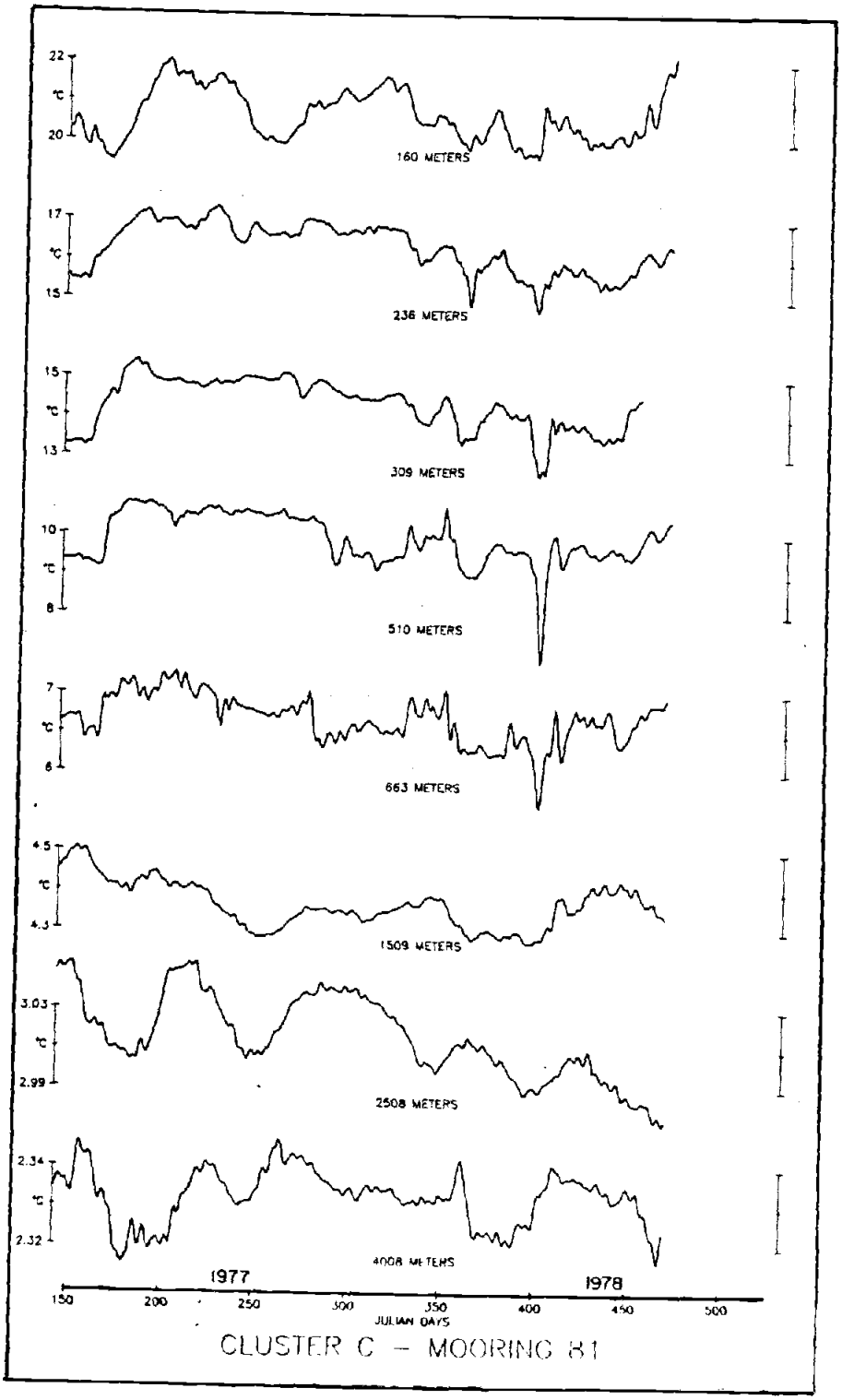
22
°C
20
160 METERS
17
°C
15
236 METERS
15
°C
13
309 METERS
10
°C
8
510 METERS
7
°C
6
663 METERS
4.5
°C
4.3
1509 METERS
3.03
°C
2.99
2508 METERS
2.34
°C
2.32
4008 METERS
1977
1978
150
200
250
300
350
400
450
500
JULIAN DAYS
CLUSTER C – MOORING 81

Figure 7c

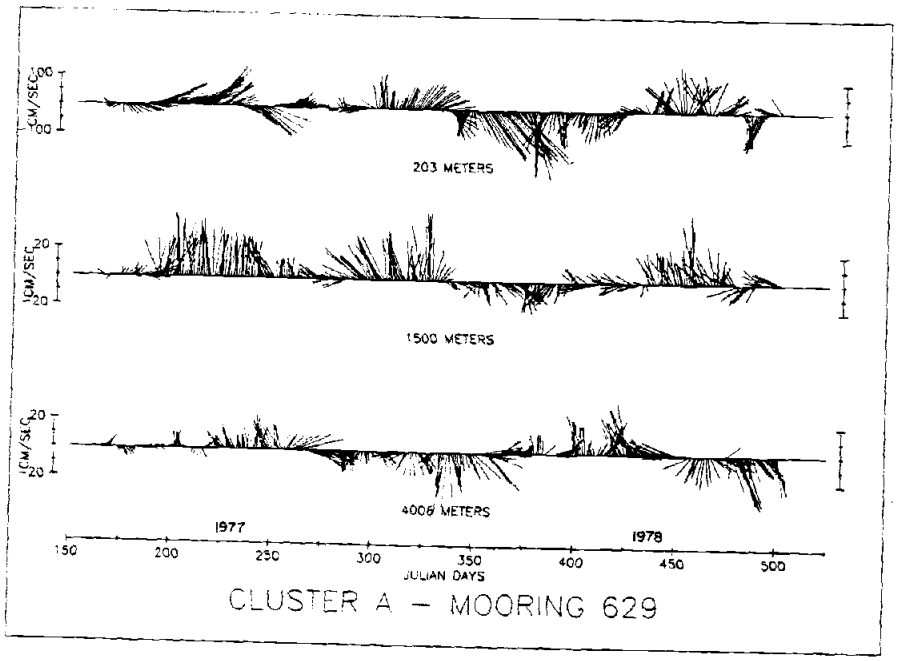
CM/SEC
100
-100
203 METERS
CM/SEC
20
-20
1500 METERS
CM/SEC
20
-20
4008 METERS
1977
1978
150
200
250
300
350
400
450
500
JULIAN DAYS
CLUSTER A — MOORING 629

Figure 8a

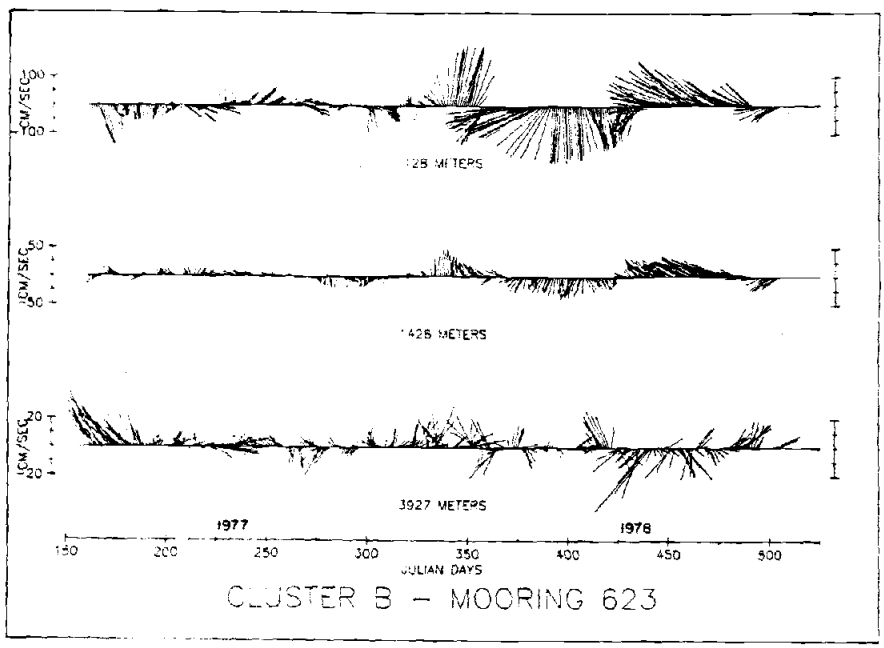
CM/SEC
428 METERS
3927 METERS
1977
1978
150
200
250
300
350
400
450
500
JULIAN DAYS
CLUSTER B – MOORING 623

Figure 8b

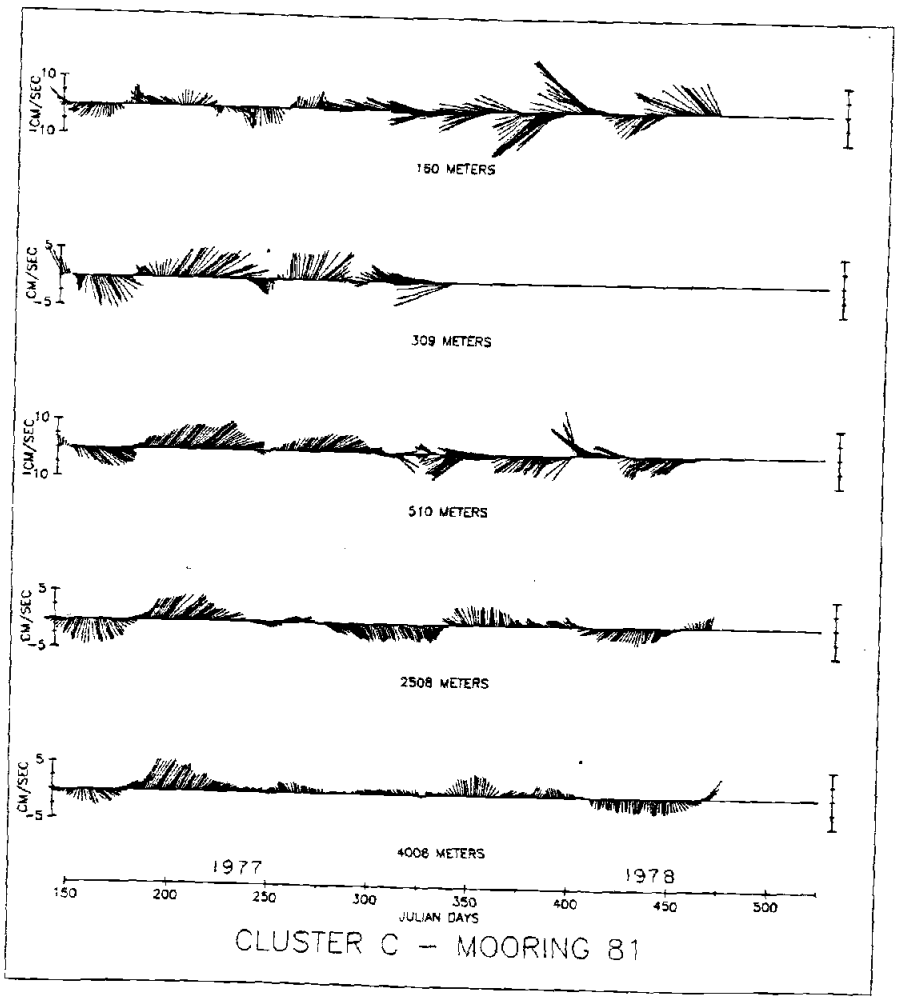
CM/SEC
10
-10
150 METERS
CM/SEC
5
-5
309 METERS
CM/SEC
10
-10
510 METERS
CM/SEC
5
-5
2508 METERS
CM/SEC
5
-5
4008 METERS
1977
1978
150
200
250
300
350
400
450
500
JULIAN DAYS
CLUSTER C - MOORING 81

Figure 8c

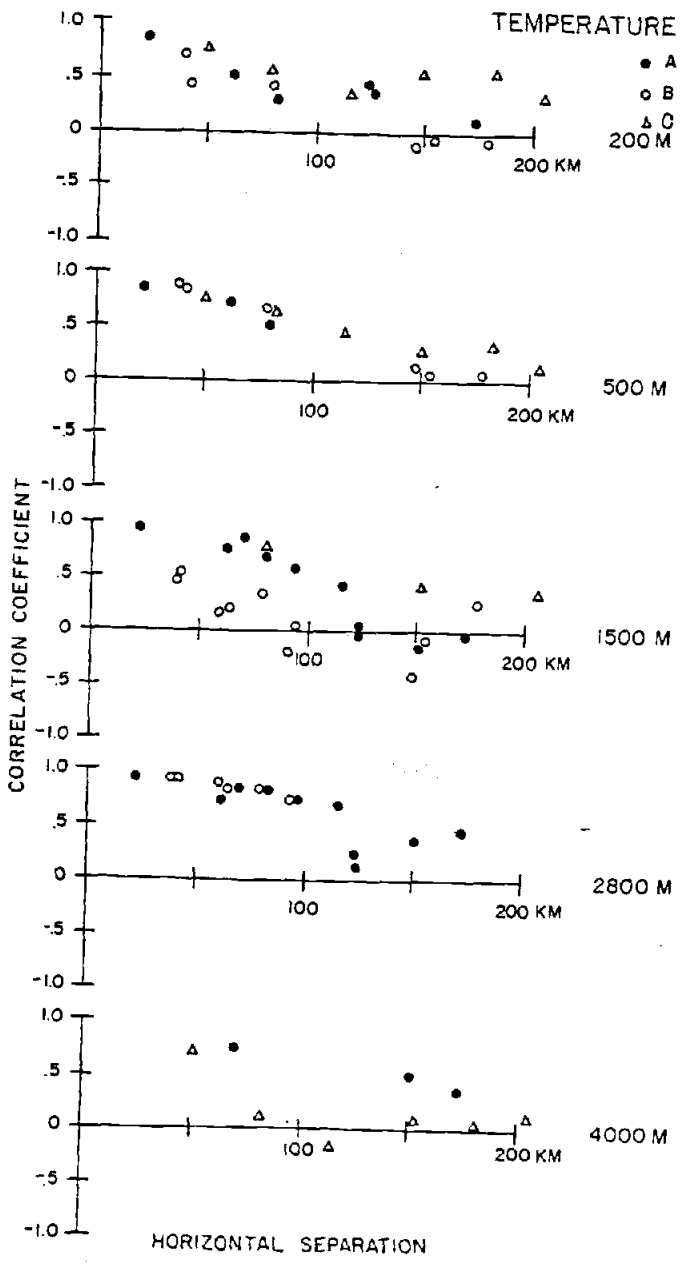
TEMPERATURE
A
B
C
200 M
500 M
1500 M
2800 M
4000 M
1.0
.5
0
-.5
-1.0
100
200 KM
CORRELATION COEFFICIENT
HORIZONTAL SEPARATION

Figure 9a

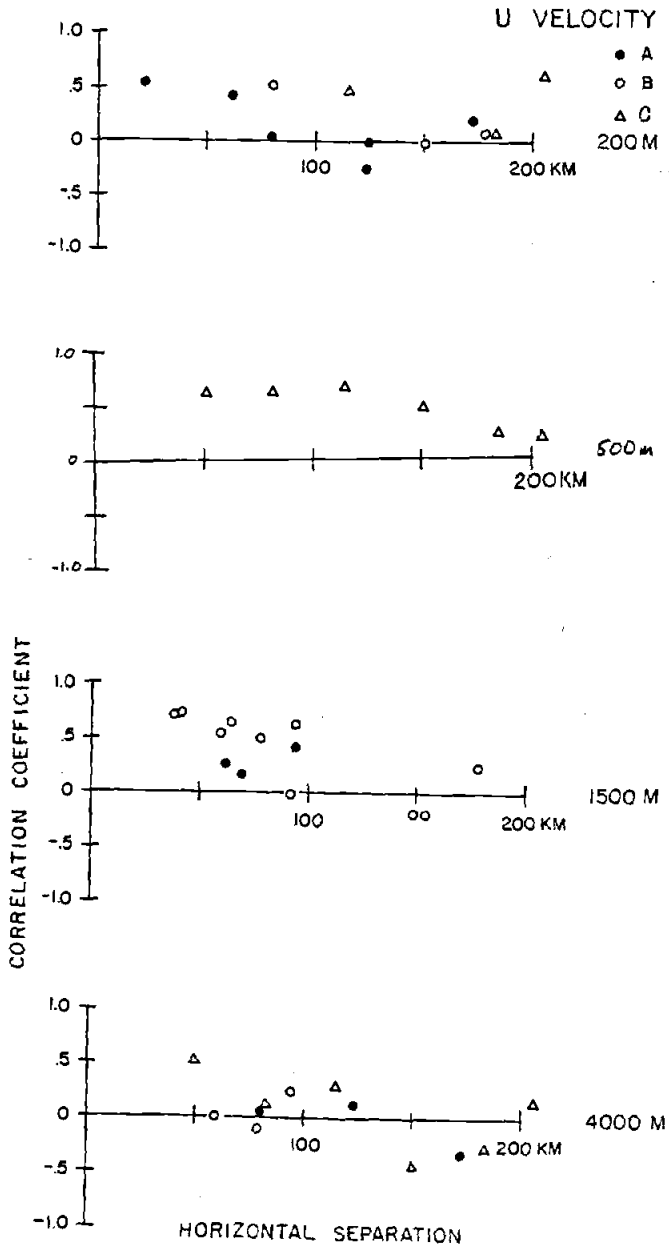
U VELOCITY
A
B
C
200 M
500 M
1500 M
4000 M
1.0
.5
0
-.5
-1.0
100
200 KM
CORRELATION COEFFICIENT
HORIZONTAL SEPARATION

Figure 9b

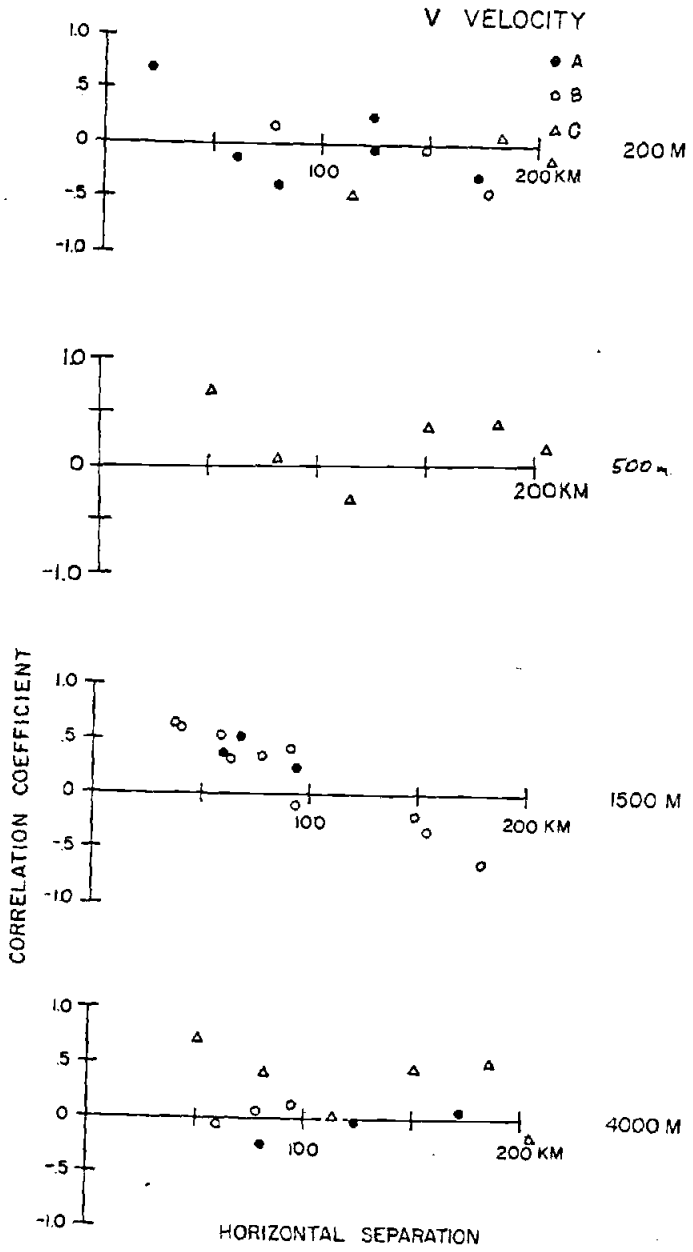
V VELOCITY
A
B
C
200 M
500 M
1500 M
4000 M
1.0
.5
0
-.5
-1.0
100
200KM
200 KM
CORRELATION COEFFICIENT
HORIZONTAL SEPARATION

Figure 9c

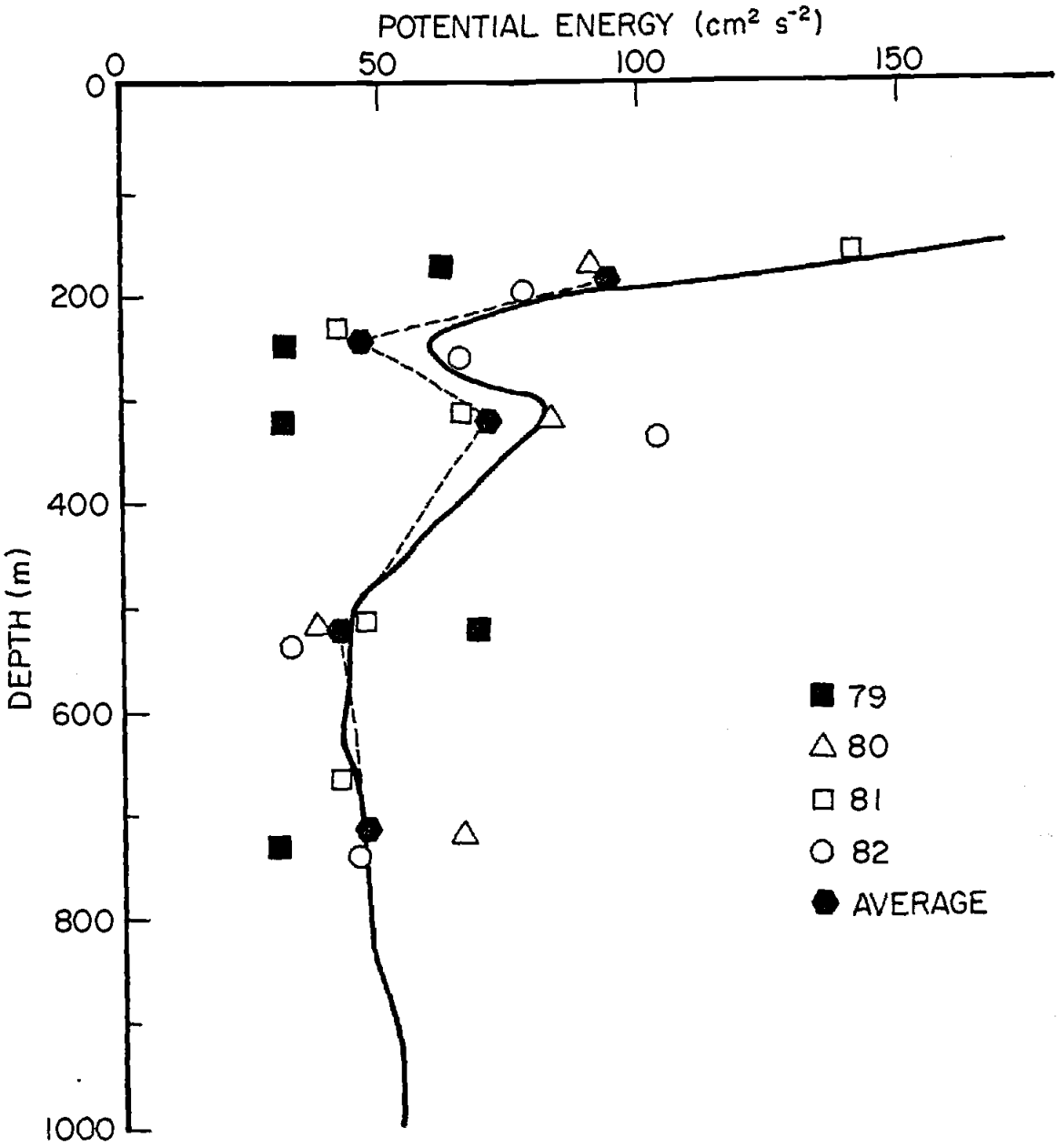
POTENTIAL ENERGY (cm² s⁻²)
0
50
100
150
0
200
400
600
800
1000
DEPTH (m)
79
80
81
82
AVERAGE

Figure 10

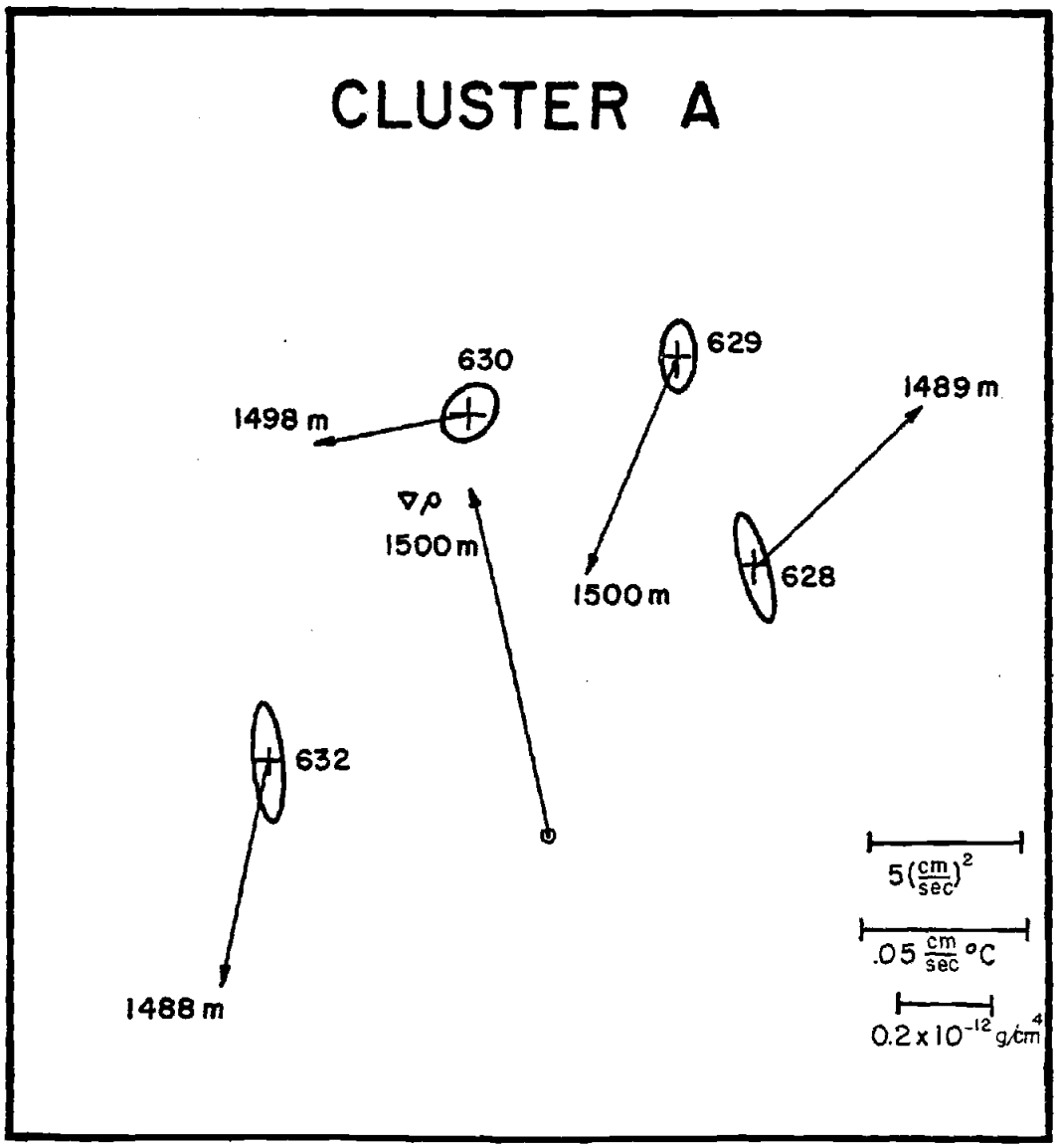
CLUSTER A
630
629
1498 m
1489 m
∇ρ
1500 m
1500 m
628
632
1488 m
5(cm/sec)²
.05 cm/sec °C
0.2x10⁻¹² g/cm⁴

Figure 11a

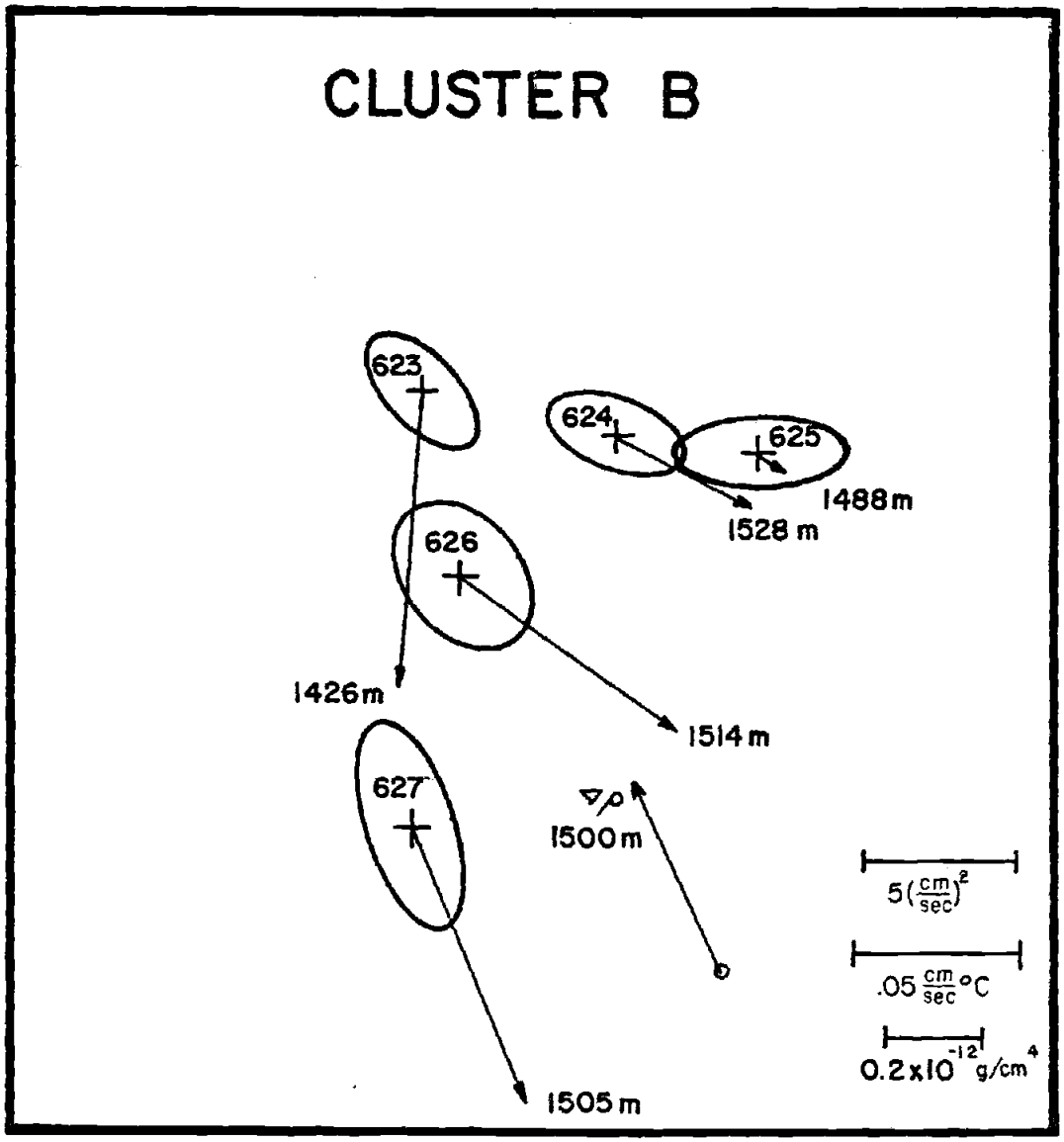
CLUSTER B
623
624
625
626
627
1488m
1528 m
1426m
1514 m
1500m
1505 m
5(cm/sec)²
.05 cm/sec °C
0.2x10⁻¹² g/cm⁴

Figure 11b

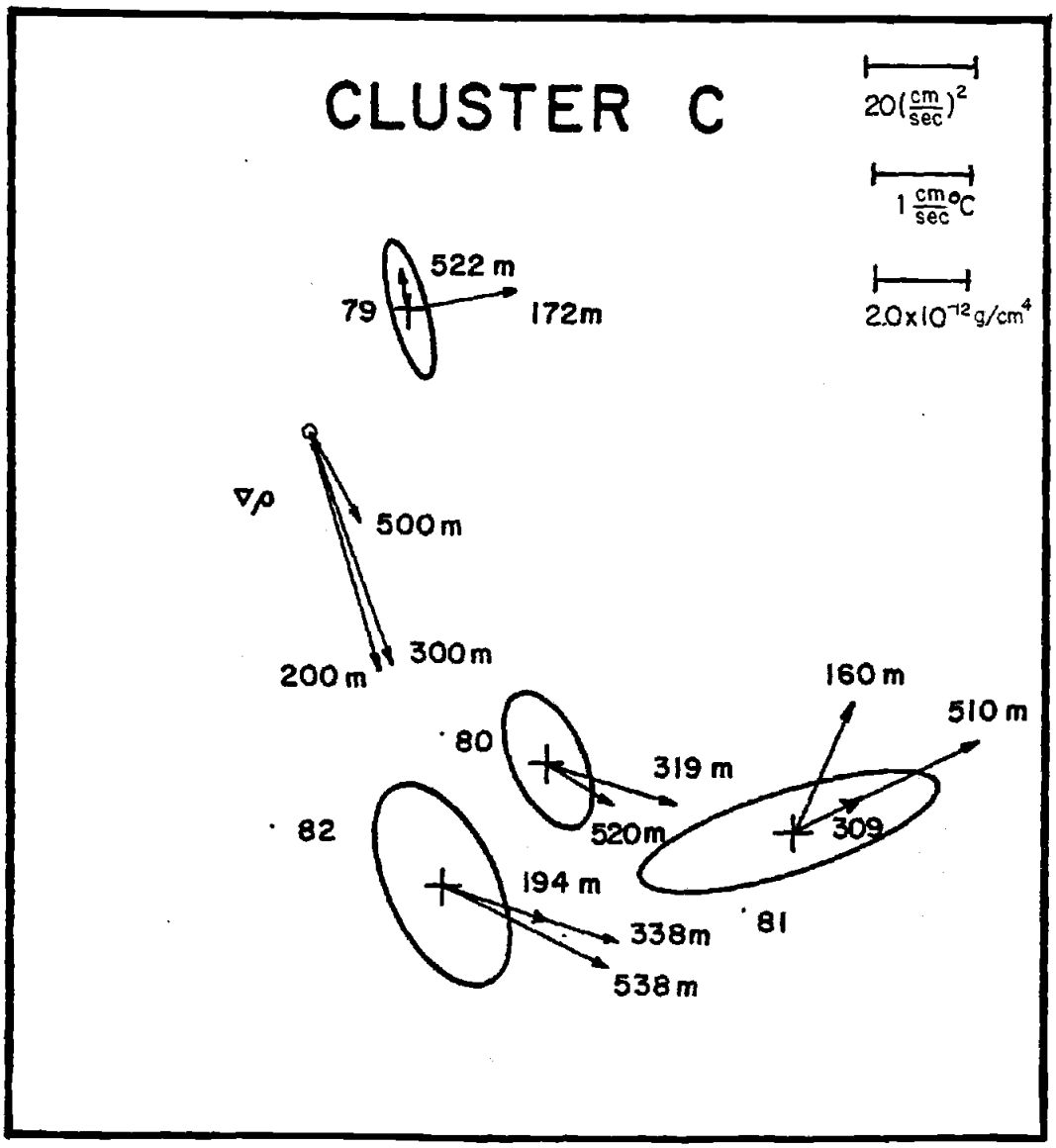
CLUSTER C
20(cm/sec)²
1 cm/sec °C
2.0x10⁻¹² g/cm⁴
522 m
79
172m
∇ρ
500 m
200 m
300 m
160 m
510 m
80
319 m
520m
309
82
194 m
338m
81
538 m

Figure 11 c

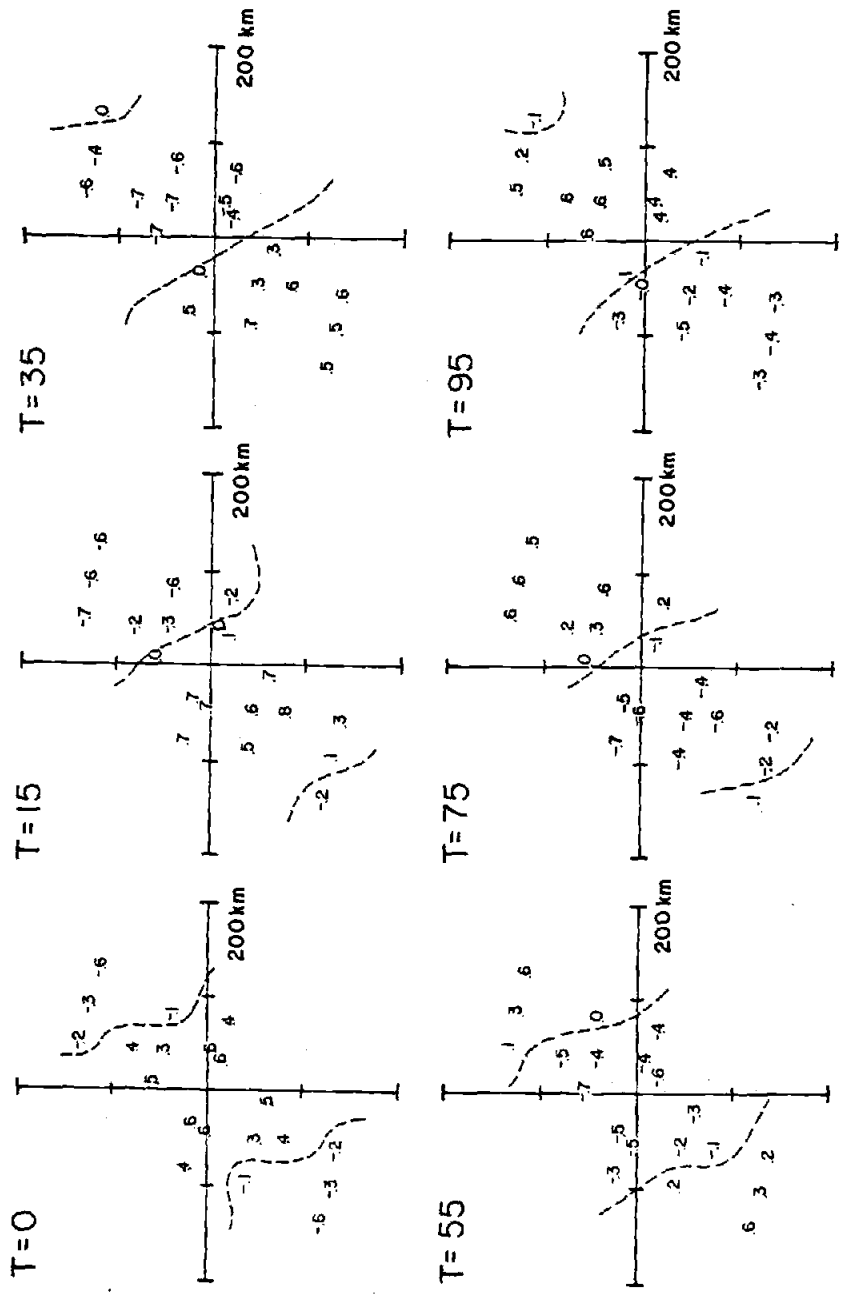

Figure 12a

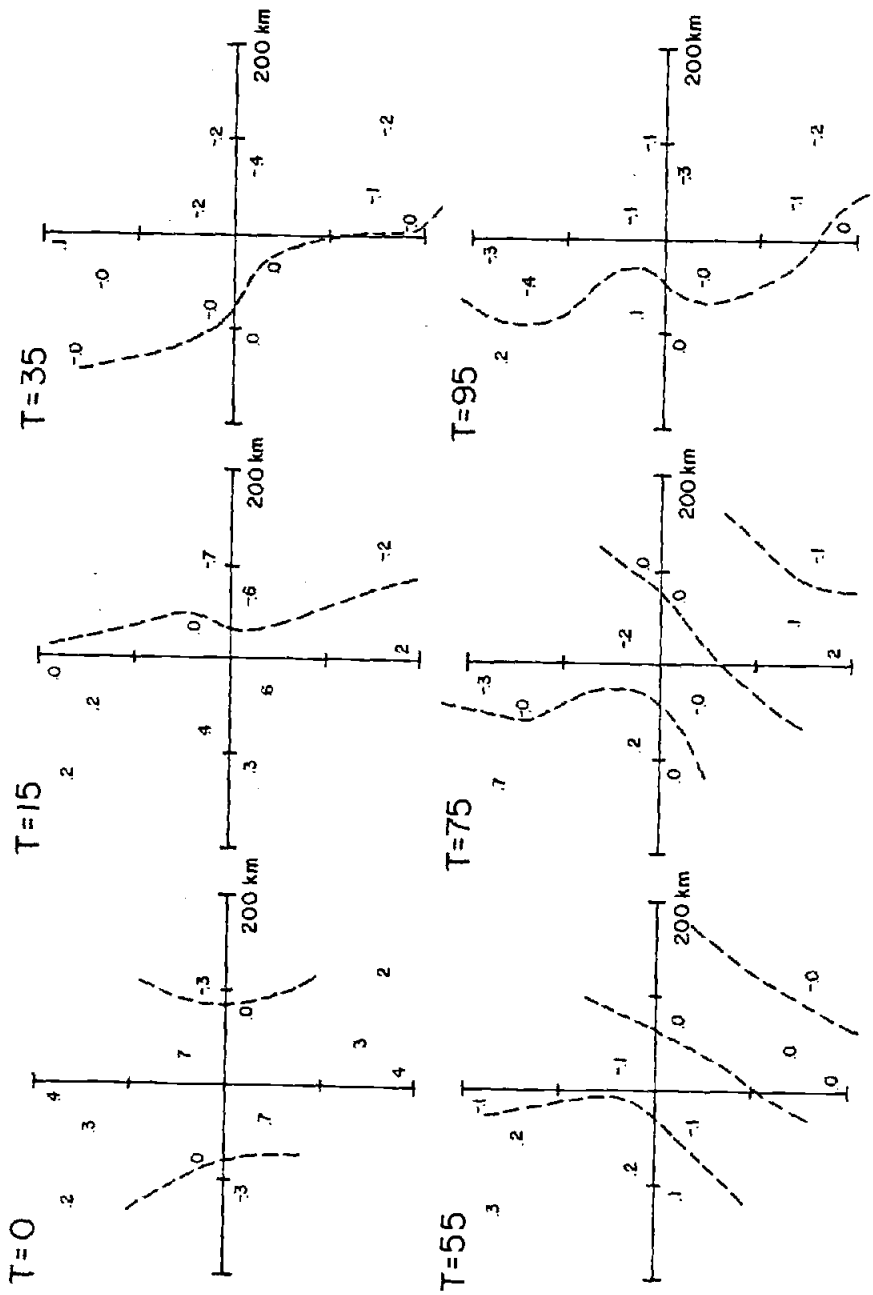

Figure 12b

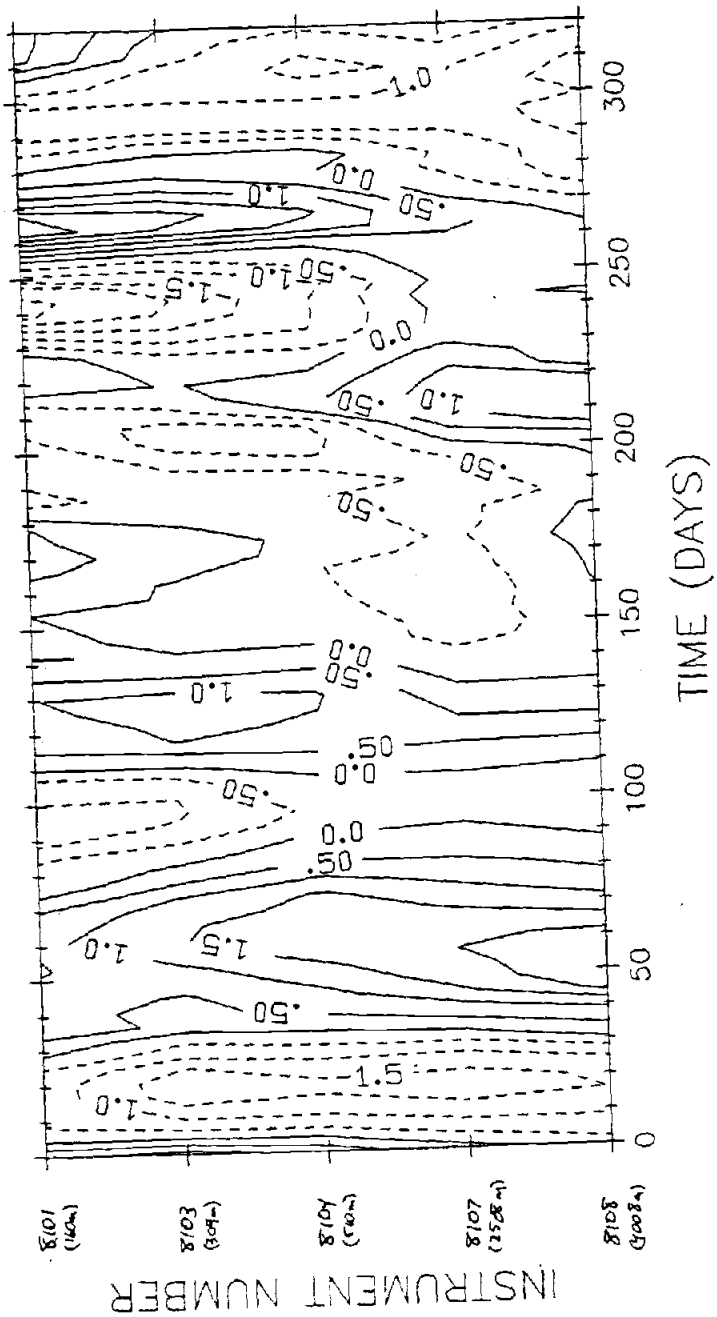
TIME (DAYS)
0
50
100
150
200
250
300
INSTRUMENT NUMBER
8101
8103
8104
8107
8108
1.0
0.0
.50
1.5

Figure 13

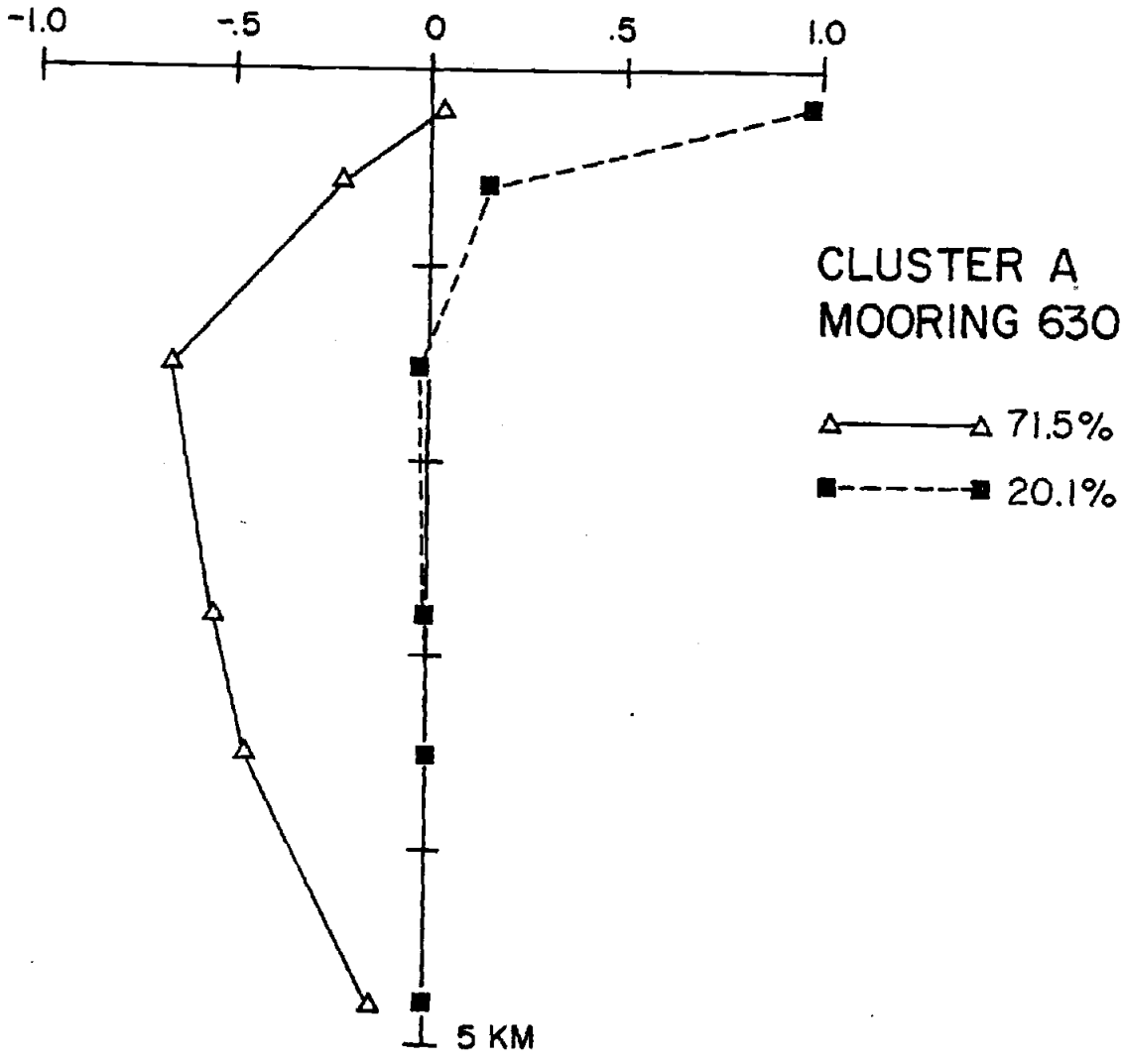

Figure 14a

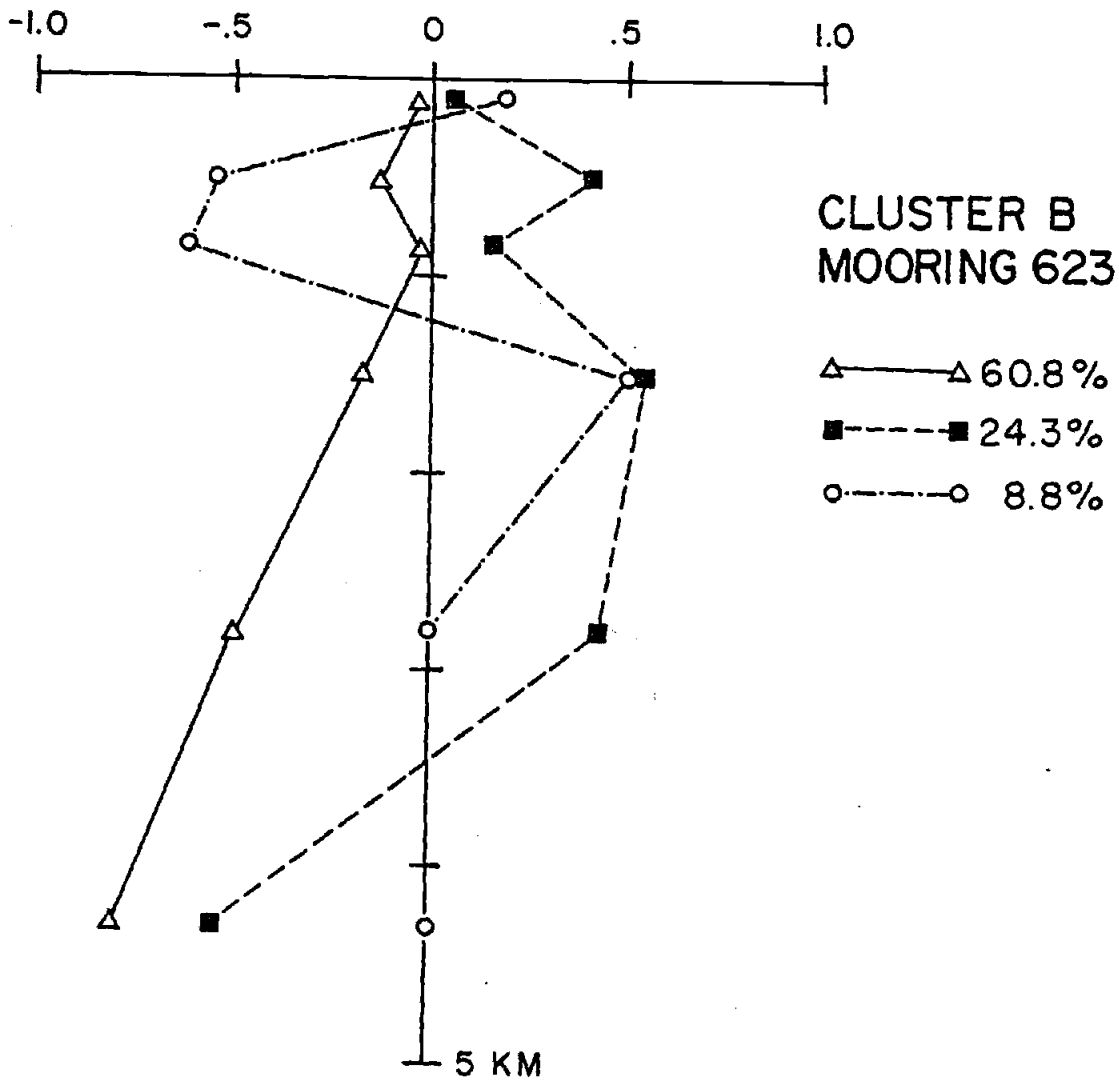

Figure 14b

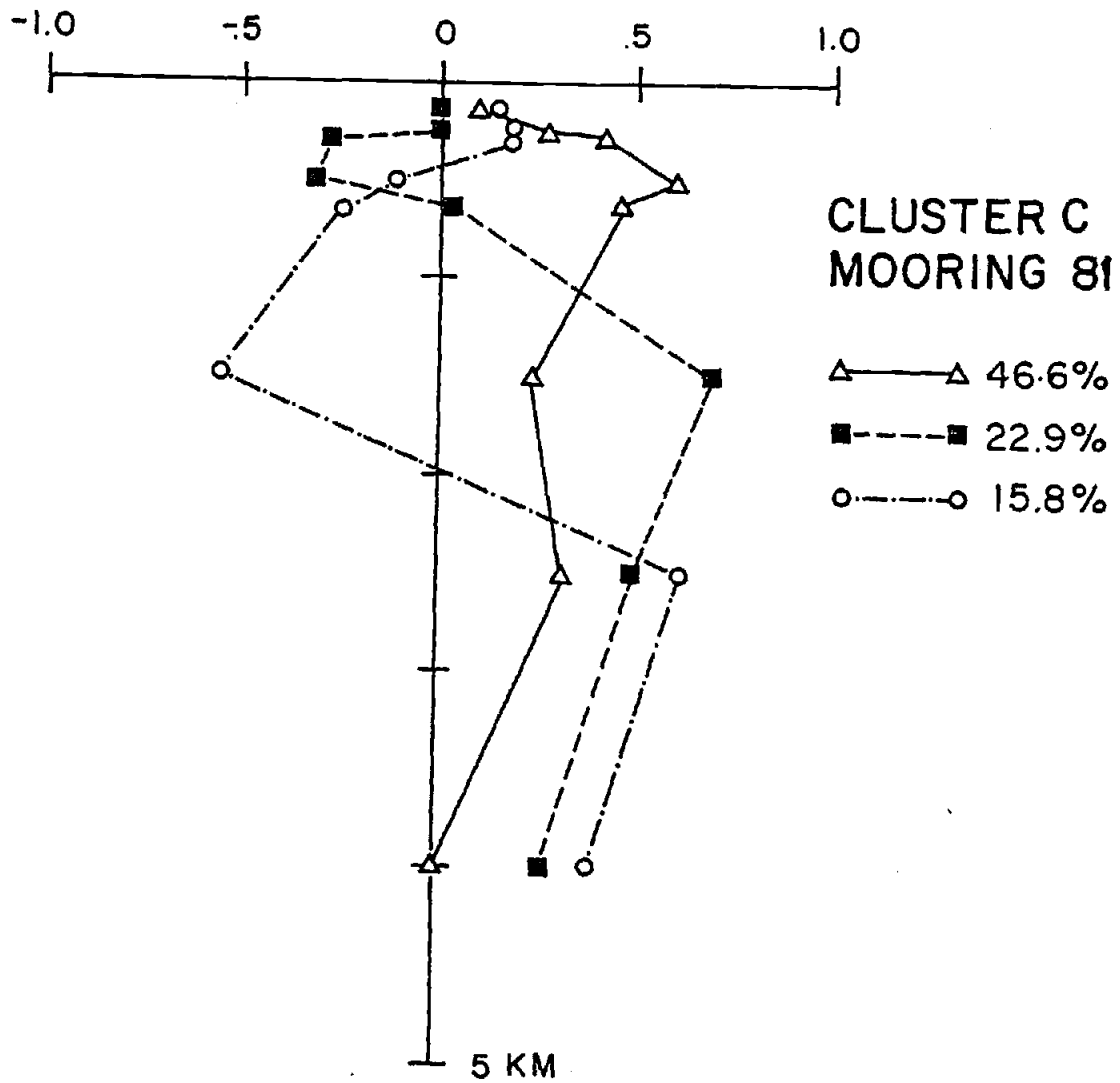

Figure 14c

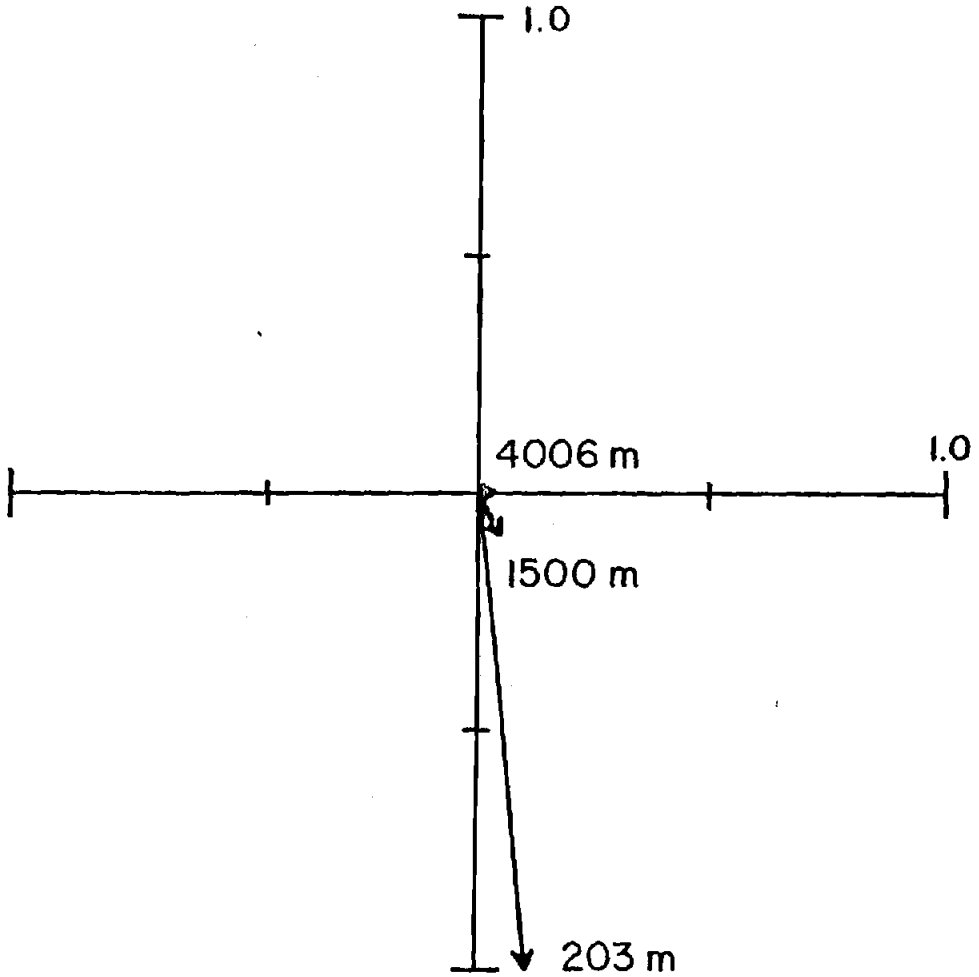

CLUSTER A
MOORING 629
96 %

Figure 15a

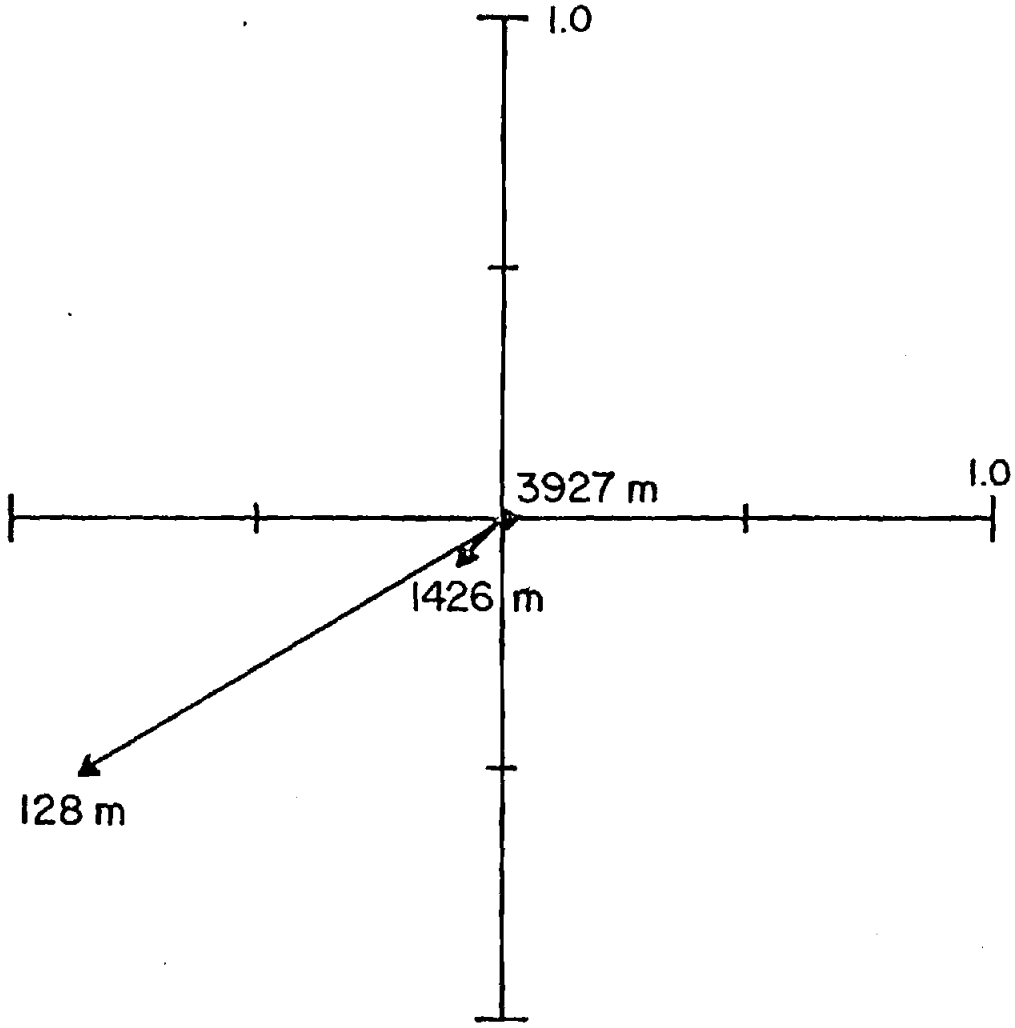

CLUSTER B
MOORING 623
96 %

Figure 15b

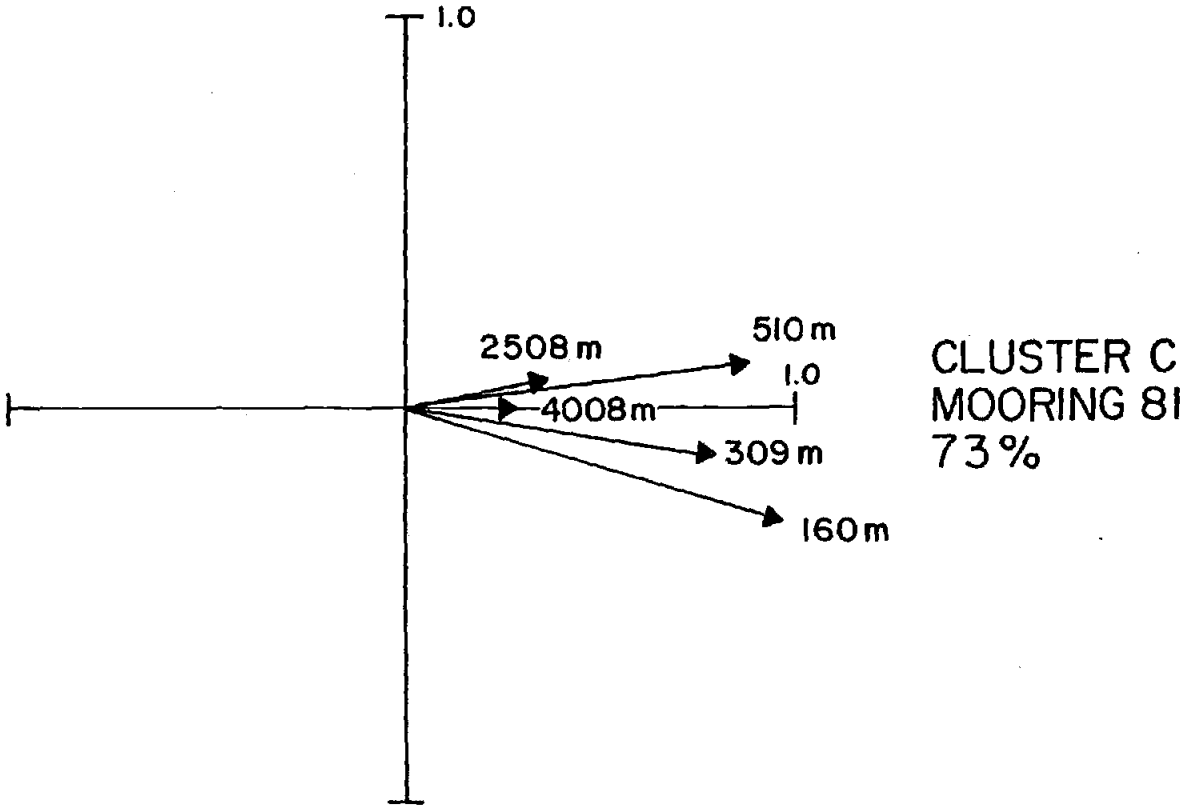

Figure 15c

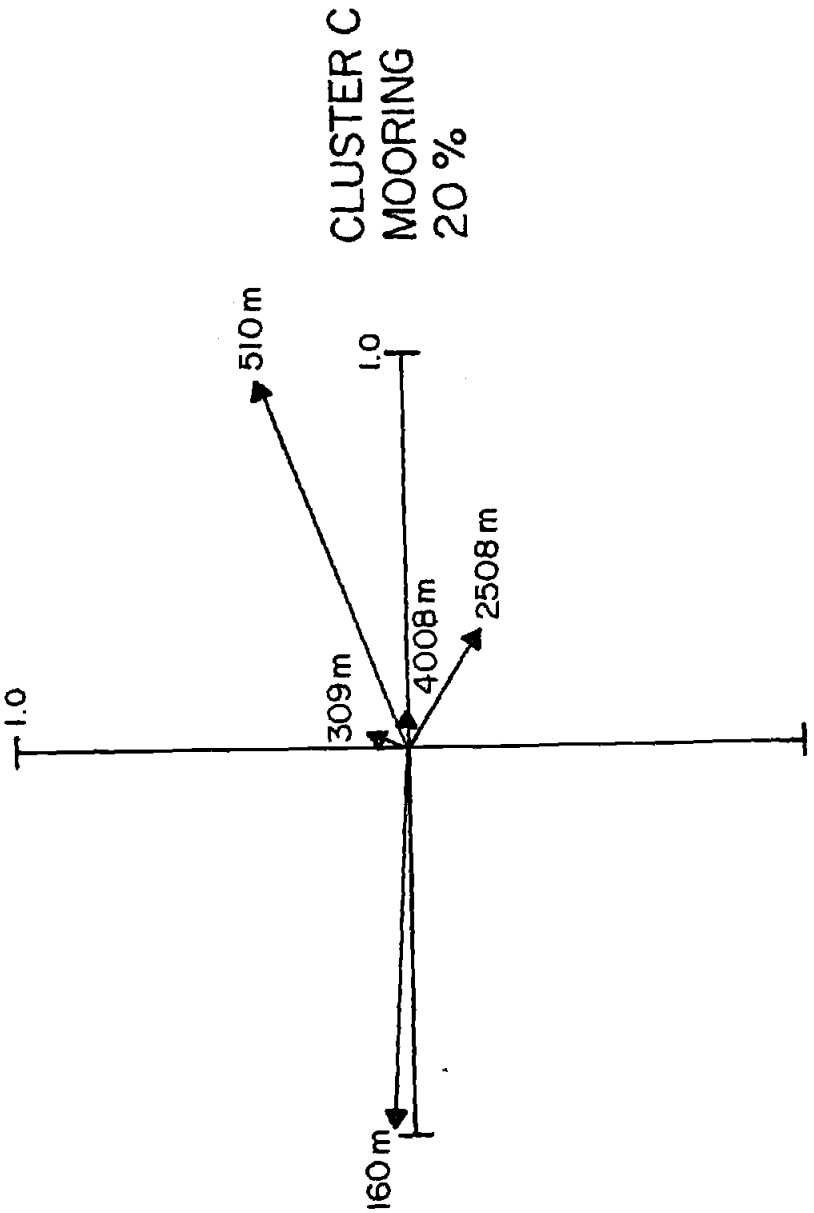

Figure 15d

Chapter III

The Vertical Structure of Observed and Geostrophically Derived Mean Flow and Heat and Salt Eddy Convergence in the Sub-Tropical North Atlantic

by

T. Keffer

and

P. P. Niiler

School of Oceanography

Oregon State University

Corvallis, Oregon 97331

October 1980

1. Introduction

Determination of the absolute velocity profile through the dynamical method requires the evaluation of some depth independent "reference velocity". Integration of the first order vorticity equation to determine the vertical velocity will require knowledge of a depth independent vertical velocity as well. Various methods have been proposed to determine these three constants from hydrographic data alone (Stommel and Schott, 1977; Schott and Stommel, 1978; Hidaka, 1940; Wunsch, 1978) or from hydrographic and wind stress data (Stommel, 1956; Sudo, 1965).

In this paper, we evaluate the horizontal "reference velocities" through use of observed stable mean flows from the POLYMODE Array III current meter data. The vertical reference velocity is obtained from Leetma and Bunker's (1978) updated charts of vertical velocities at the base of the Ekman layer.

The resulting absolute velocity field is then used to calculate mean advection of heat, salt, and density. Because this advection must be balanced by turbulent convergence, an estimate of the "diffusion" terms in the respective balance equation can be made. We can thus determine regions where potential vorticity is conserved and the method of maximal potential vorticity conservation (the so-called β-spiral method) should work.

Because Array III, Cluster A and B (Figure 1) are near the areas studied by Schott and Stommel (1978) and Behringer and Stommel (1980), we can determine whether the assumption of conservation of potential vorticity is appropriate for this area. Our conclusion is that the

ocean does not cooperate with the β-spiral method. In the depth intervals where potential vorticity is conserved, there are no potential vorticity gradients and the β-spiral method is ill-conditioned. In the regions where potential vorticity gradients exist, it is not conserved and the β-spiral method is physically unrealistic. This suggests that in the subtropical North Atlantic, inverse techniques which rely upon conservation principles are ill-conditioned and direct measurements will be needed to determine the absolute flow patterns.

The divergence and absolute velocity profiles are also studied for their implications on water mass movements. Although the divergence profiles give no information on the form the "dissipative" terms might take, horizontal eddy divergence is found to be appropriate in the lower-thermocline at Clusters A an B while double-diffusion processes are probably operating in the mid-thermocline at Cluster C.

2. Theory

In the central subtropical gyre, the large horizontal scale mean flow is in hydrostatic and geostrophic balance. Therefore, the relationship between the mean horizontal velocity components $\bar{u}$ and $\bar{v}$ and the *in situ* density field ρ is expressed in the thermal wind relationship, and the equation for mean vertical velocity, $\bar{w}$, is obtained from the continuity equation:

$$\frac{\partial \bar{u}}{\partial z} = \frac{g}{f\rho}\frac{\partial \rho}{\partial y} \qquad \frac{\partial \bar{v}}{\partial z} = -\frac{g}{f\rho}\frac{\partial \rho}{\partial x} \qquad \frac{\partial \bar{w}}{\partial z} = \frac{\beta}{f}\bar{v} \tag{2.1a,b,c}$$

where $f = f_o + \beta y$ is the Coriolis parameter, g is gravitational acceleration and the β-plane is used for convenience. Vertical integration of (2.1) give the expressions:

$$\bar{u}(x,y,z) = u_o(x,y) + \int_{z_o}^{z} \frac{g}{f\rho}\frac{\partial \rho}{\partial y}\, dz' \tag{2.2a}$$

$$\bar{v}(x,y,z) = v_o(x,y) - \int_{z_o}^{z} \frac{g}{f\rho}\frac{\partial \rho}{\partial x}\, dz' \tag{2.2b}$$

$$\bar{w}(x,y,z) = w_1(x,y) + \frac{\beta}{f}(z - z_1)v_o - \int_{z_1}^{z} dz' \int_{z_o}^{z} \frac{\beta g}{f^2\rho}\frac{\partial \rho}{\partial x}\, dz'' \tag{2.2c}$$

where u_o, v_o are the horizontal velocity components at a reference level $z = z_o$ for horizontal velocity and w_1 is the vertical velocity at a reference level $z = z_1$ for vertical velocity. Since the horizontal density gradients can be determined from hydrographic data, knowledge of the reference velocities (u_o, v_o, w_1) allows determination of the three dimensional absolute velocity field.

The conservation of potential temperature, salt, and potential density by this mean geostropic motion is expressed as:

$$\bar{u}\frac{\partial T}{\partial x} + \bar{v}\frac{\partial T}{\partial y} + \bar{w}\frac{\partial \theta}{\partial z} = \dot{Q}_\theta \qquad (2.3a)$$

$$\bar{u}\frac{\partial s}{\partial x} + \bar{v}\frac{\partial s}{\partial y} + \bar{w}\frac{\partial s}{\partial z} = \dot{Q}_s \qquad (2.3b)$$

$$\bar{u}\frac{\partial \rho}{\partial x} + \bar{v}\frac{\partial \rho}{\partial y} + \bar{w}\frac{\partial \tilde{\rho}}{\partial z} = \dot{Q}_{\tilde{\rho}} \qquad (2.3c)$$

where $\dot{Q}_\theta$, $\dot{Q}_s$, $\dot{Q}_{\tilde{\rho}}$ are the mean turbulent or "diffusive" eddy convergence of potential temperature (θ), salinity (s), and potential density ($\tilde{\rho}$). Here, horizontal derivatives use T and ρ, the <u>in situ</u> temperature and density, while vertical derivatives use θ and $\tilde{\rho}$, temperature and density corrected for the effects of adiabatic heating and compressibility. Knowledge of the reference velocities (u_o, v_o, w_1) allows the left-hand sides of (2.3) to be determined from hydrographic data alone. This allows the inference of the turbulent terms on the right-hand sides.

Conversely, if we can estimate the value of $\dot{Q}_\theta$, $\dot{Q}_s$, or $\dot{Q}_{\tilde{\rho}}$ at three vertical levels from another data set, then (2.3) will form linear algebraic equations for (u_o, v_o, w_1) and the three dimensional velocity profile is known. In fact, any <u>three</u> physical statements will do for the computation of (u_o, v_o, w_1). Schott and Stommel (1978) and Behringer and Stommel (1980) compute u_o, v_o from least squares minimization of the potential vorticity convergence $\frac{\partial}{\partial z}(\dot{Q}_{\tilde{\rho}}/f\ \frac{\partial \tilde{\rho}}{\partial z})$ over various intervals z_1 to z_o and set $\dot{Q}_{\tilde{\rho}} = 0$ at z_1, where $\tilde{\rho}$ is the potential density. Niiler and Reynolds (1980) minimize (u_o, v_o, w_1) over various intervals in the least squares sense. Wunsch (1978) sets the horizontal area average $\iint_{A_i} \dot{Q}_\theta dSdz$ equal to zero over three dimensional closed areas which are circumscribed by curve $S(x,y) = 0$

and whose vertical extent in z is between sheets of constant θ_i, and minimizes the average reference level kinetic energy, $\iint_{A_o} (u_o^2 + v_o^2)dA$, at a particular level A_o enclosed by the curve S. Davis (1978) points out the equivalance of these methods when applied over a large area and suggests, because ρ_x and ρ_y are "noisy" data, that geostrophic "noise" should really be minimized over appropriately chosen intervals with respect to (u_o, v_o, w_1). Each of the methods will give a somewhat different result and no direct and independent test of any of these methods has been done.

Our choices for u_o, v_o are from direct measurements from the POLYMODE data set. The reference vertical velocity is the Ekman vertical velocity $w_1 = \hat{k} \cdot \nabla \times (\vec{T}_o/f\rho_o)$ at $z_1 = 0$ (the surface), where $\vec{T}_o$ is the surface wind stress (Leetma and Bunker, 1978). The resulting absolute velocity profiles at Clusters A and B are compared to those of Schott and Stommel (1978) and Behringer and Stommel (1980).

The absolute profiles are also used to calculate the left-hand sides of (2.3) and thus profiles of potential temperature, salinity, and potential density eddy diffusion. If $\dot{Q}_{\tilde{\rho}} = 0$ everywhere, then vertical velocity could be computed from (2.3c):

$$\tilde{w} = -(u \frac{\partial \rho}{\partial x} + v \frac{\partial \rho}{\partial y}) / \frac{\partial \tilde{\rho}}{\partial z} \qquad (2.4)$$

Eqn. (2.1c) subtracted from the vertical derivative of (2.4) gives

$$\tilde{w}_z - \bar{w}_z = \frac{\partial}{\partial z}(\dot{Q}_{\tilde{\rho}} / \frac{\partial \tilde{\rho}}{\partial z}) \qquad (2.5)$$

Thus, the two estimates of w will have the same vertical derivative where the right-hand side of (2.5) vanishes. These are the depth intervals where the β-spiral method [which is based on the minimiza-

tion of the right-hand side of (2.5)] should work for computing reference velocities.

We can therefore discern not only depth intervals where heat and salt convergence minimization should work, but also where the β-spiral method is the optimum method. However, we cannot test Wunsch's (1978) method because not enough direct measurements are available in this area.

3. Data Base and Methods

Hydrographic. The National Oceanographic Data Center's (NODC) archived bottle data, interpolated to standard depths (Anon, 1974), was used to calculate horizontal density, temperature, and salinity gradients. There were 67, 69, and 51 stations within the boxes for Clusters A, B, and C, respectively, shown in Figure 1. Only those stations that showed a continuous increase in surface referenced potential density and a smooth temperature and salinity profile, were retained. This station editing left the 55, 47, and 36 stations shown in Figure 1. Within these retained casts no more than two interpolated observations at standard depths were allowed between observed depths; i.e. if the observed depths were so far apart vertically that there were three or more interpolated depths between them, then all of the interpolated depths were rejected.

Only five bottle stations extended to 5000 m within the Cluster C box (the bottom averages 5300 m). All of them were clustered near the western part of the box while the moorings are centered in the box. To improve the coverage at depth, 16 Conductivity-Temperature-Depth (CTD) stations were included. These were made by the GEOSECs operation group of the Scripps Institute of Oceanography during the POLYMODE Array III deployment and recovery cruises in 1977 and 1978, respectively. All casts included at least three bottles centered on the extrema of the T-S curve for calibration purposes. Density is considered correct to within .01 σ_t units and repeatable to .006 units within a cruise.

Direct Measurements. In the period between May 1977 and July 1979, three clusters of moorings were deployed in POLYMODE Array III. Cluster A (45°N, 29°W) and Cluster B (41°N, 28°W) were on the western and eastern slopes of the mid-Atlantic Ridge, respectively, and Cluster C (46°N, 54°W) was in the Atlantic North-Equatorial current (Figure 1). In Clusters A and B, some moorings had 825 days of data while in Cluster C, 354 days are available. The raw data from these moorings were low-pass filtered with a cut-off of 0.5 cycles per day (0.25 for Cluster C) and then subsampled daily. Estimates of the true means and variances of the currents were calculated from the resulting series. Mean flows significantly different from zero were found in Cluster C at 180-500 m and at 4000 m. Significant mean flows were found at Clusters A and B at 1500 m. Complete descriptions of the cluster results can be found in Fu, Keffer, Niiler and Wunsch (1980).

Horizontal Velocity Profile. The procedure for calculating the mean relative velocity field was as follows: first, at a given depth, temperature, salinity, and pressure were used to calculate *in situ* density. A least square regression of ρ on x and y was then done to this $\rho(x,y)$ field. The slopes of the resultant "plane" (ρ_x and ρ_y) are the mean horizontal density gradients at that depth. These were then related to vertical shear through the thermal wind relation (2.1) and vertically integrated from a reference level (discussed below) to give the relative horizontal (u and v) velocity field.

The choice of an appropriate reference level and reference velocity at each cluster was made by referring to the current meter data. At Clusters A and B, stable mean flows to the northwest were observed at 1500 m at all moorings except one (Cluster B, #627) where the mean flow was still northward but had a slight eastward component (see Figures 2a,b and 3a,b). The average (u_o, v_o) of the observed mean flows at 1500 m are $(-.62 \pm .1, .69 \pm .1)$ and $(-.80 \pm .4, .38 \pm .1)$ in cm s^{-1} at Clusters A and B, respectively. The meridional velocity within these two clusters was especially stable, with a maximum difference of observed means of only 0.5 cm/sec. Confidence in the meridional reference velocities at Clusters A and B is important because they will be used later to find vertical velocity.

The resulting absolute zonal and meridional velocity profiles at Clusters A and B are shown in Figures 2 and 3 along with the observed mean flows. Also shown is an estimate of the standard error of the velocity profiles (dashed line). Standard errors of the slopes of the density planes (and hence shear) can be determined from the quality of the fit of the density planes (Draper and Smith, 1966) which, in the absence of measurement errors, is related to the eddy energy at each level. If the shears at each level are independent then a standard error of the integral of the shear (and hence velocity) can be derived. Details are in Appendix A.

Direct measurements at Cluster C indicate that 2500 m is a level of no horizontal motion ($u_o = 0$, $v_o = 0$). Unfortunately, only two instruments functioned properly at this depth and so our assumption about the reference velocity is not as well founded as at Clusters A

and B. However, because the historical data indicates no vertical shear for 500 m to either side of 2500 m, we believe this is not a sensitive choice. Again, the meridional velocity seems to be more stable than the zonal velocity (Figures 2c and 3c).

At all three clusters the final absolute profiles agree quite well with the directly measured mean velocities. In general, the meridional velocities are in better agreement than the zonal velocities, especially in the upper ocean. This is not surprising in light of the longer time scale of the u velocity observed in Fu et al. (1980). Confidence in the two mid-gyre profiles (Clusters A and B) is increased by their similarity, differing only in details at the base of the thermocline and at the bottom, despite being derived from completely independent data sets.

The zonal profile at Cluster C deserves special comment. The hydrographically derived profile seems to underestimate the shear that was observed between 500 and 200 meters. We can determine if the observed mean shear is consistent with the mean horizontal density gradient present during the deployment of the moorings, by using the mean temperatures recorded by the current meters. These were corrected to nominal depths (175 m, 325 m, 525 m) and then the horizontal temperature gradient was calculated in a least squares fashion. This was then converted to a horizontal density gradient using appropriate values of $d\rho/dT$. The thermal wind relation was then used to estimate the shear. The shears estimated this way agree extremely well with the observed shears, and we conclude that the thermal wind relation holds. It would appear that the moorings were deployed during a time

of anomously large shear.

This same profile (Fig. 2c) also predicts the currents near the bottom to be more to the west than was observed at most of the instruments. The Cluster C area is where the deep western North Atlantic and South Atlantic basins are connected. From bathymetric maps one can see that the deepest passage runs north and then west. Mooring #79 was located at this turn and is the one that measured the westward mean at 4000 m in Figure 2c. The hydrographic data will "see" the largest scale and hence predicts a northwestward direction.

Figure 4 shows the absolute hodographs of the horizontal velocity at the three clusters. For comparison, the absolute hodograph proposed by Schott and Stommel (1978) is drawn as a dotted line on Figure 4a and the hodograph proposed by Behringer and Stommel (1980) on Figure 4b. The relative spirals are virtually identical. However, the direct measurement method shows large values of the deep velocity to the northwest which is not found with the β-spiral method. In fact, a net northward mean velocity at Clusters A and B of .45 and .29 cm s^{-1}, respectively, is found.

Vertical Velocity Profile. As shown in Section 2, the vertical velocity profile is derived from the vertical integral of the north-south component of the flow. Our reference velocity, w_1, is taken to be the Ekman velocity $\hat{k} \cdot \nabla \times (\vec{T}/\rho_o f)$ at the ocean surface as calculated by Leetma and Bunker (1978). We choose -1.5, -1.5, -2.5 x 10^{-4} cm s^{-1}, at A, B, and C, respectively. This prescription is consistent as long as we do not use the computed u,v,w in the vigorously turbulent surface layer. There the local velocity profile is

modified by the turbulent vertical transport of horizontal momentum. However, below about 100 m w is computed accurately by this scheme.

The profiles of $\bar{w}$ are displayed on Figure 5. Because the $\bar{v}(z)$ profiles of Clusters A and B are similar, so is $\bar{w}(z)$, and it is negative throughout the entire water column. At Cluster C, the near surface down-welling is larger. However, because there is a strong geostrophic flow to the south in the upper layers, the Ekman divergence does not penetrate into the main thermocline.

As discussed in Section 2, if the turbulent flux of potential density vanishes, a vertical velocity estimate can also be made from the balances of horizontal and vertical density advection (see Equn. 2.4). The vertical velocity computed this way is also shown on Figure 5. The horizontal density gradients are those used in the velocity calculations. The vertical gradient is described in the next section. The two profiles of w are not the same because of the dissipation of density, also described in the next section.

Divergence Profiles. Knowledge of the three dimensional velocity profile allows the calculation of divergence of potential temperature, salinity, and potential density from the dot product of the mean velocity vector with the respective mean gradient (left-hand sides of 2.3). We evaluated the horizontal temperature and salinity gradients with a plane fitting method identical to the one used to calculate the velocity field. No extra editing of the data set was done, nor were any observations added or removed.

The vertical gradients were calculated from the ensemble average of CTD casts taken during the recovery cruises. This was a total of

5, 5, and 28 casts at Clusters A, B, and C, respectively. Vertical gradients of density and temperature at a standard depth were calculated by first referencing them to a nominal pressure at that depth to remove the effects of compressibility and adiabatic heating. In this way, temperature and density used at each depth were "conserved" quantities. No corrections are necessary for salinity. Vertical gradients were then estimated from linear regressions of salinity, or these corrected temperatures and densities, on depth. The regressions were done in bands 50 m thick (100 m below 1000 m) at 2.0 m resolution (2.5 for Cluster C) around each standard depth. The resulting profiles are shown in Figures 6 and 7.

The potential density flux distribution with depth is on Figure 6. Remarkably, at both Clusters A and B the potential density increases following the mean motion throughout the water column. The largest values of the convergence are below the warm, saline, subtropical surface water (200-400 m) and in the water mass surrounding the Mediterranean warm, salty water at 1200 m.

Ocean mesoscale eddy processes can result in an eddy diffusion expressed as

$$\dot{Q}_{\tilde{\rho}} = -\overline{u' \frac{\partial \rho'}{\partial x}} - \overline{v' \frac{\partial \rho'}{\partial y}} - \overline{w' \frac{\partial \tilde{\rho}'}{\partial z}} \qquad (3.1)$$

where the primed quantities represent the low-frequency deviations from the mean quantities. The first two terms on the right-hand side of (3.1) can be computed from current meter data. Following Bryden (1976), these can be evaluated, using the geostrophic balance, as

$$-\overline{u' \frac{\partial \rho'}{\partial x}} - \overline{v' \frac{\partial \rho'}{\partial y}} = \frac{f\rho_o}{g} \left(\overline{u' \frac{\partial v'}{\partial z}} - \overline{v' \frac{\partial u'}{\partial z}} \right) \qquad (3.2)$$

The quantities u' and v' are taken to be the vertical averages and u_z' and v_z' are the vertical differences between two current meters. At Cluster C, 8 of such pairings are possible. Estimates of $-\overline{u'\rho_x'} - \overline{v'\rho_y'}$ are shown on Figure 6. In all cases but one they lie to the left of the hydrographically inferred $\dot{Q}_{\tilde{\rho}}$ implying a mean negative $\overline{w'\rho_z'}$.

4. Discussion and Conclusions

The divergence profiles shown on Figures 6 and 7 have errors that may be as large as the estimate itself in some depth ranges. However, at other depths the picture is unambiguous. Consider the depths near the Mediterranean tongue (1000 to 1200 m) at Clusters A and B. Figure 8 shows salinity on the 6°C surface (Worthington, 1976) with the calculated absolute horizontal velocity vectors from appropriate depths (1150 m, 1250 m, and 800 m at Clusters A, B, and C, respectively) superimposed. Also shown is the observed salinity gradients from the plane fitting procedure in Section 3. The velocity vectors at Clusters A and B are very near the reference depths where very stable mean flows to the north were observed in the current meter data and so do not involve integration through large sections of the water column. It is clear that there will be depths where low salinity water will be moving northward and into the high salinity Mediterranean salt tongue. The implied Eulerian salinity divergence by the horizontal mean flow ($\bar{u}_H \cdot \nabla\bar{S} > 0$) must be balanced by either a salinity convergence from the mean vertical velocity ($\overline{w}\,\overline{S_z} < 0$) or by eddy convergence ($\overline{-\vec{u}' \cdot \nabla S'} > 0$). The former would require an intricate vertical velocity field because the vertical salinity gradient changes sign across the Mediterranean tongue. Indeed, the profiles in Figures 7a, 7b suggest the latter. If the needed eddy convergence was entirely horizontal, Needler and Heath's (1975) estimate of 2×10^7 cm^2 s^{-1} for the horizontal austausch coefficient would imply a mean horizontal salinity Laplacian ($\nabla_H^2\bar{S}$) of 5×10^{-17} ppt cm^{-2} at Cluster B at 1000 m. Thus the gradient shown in Figure 8

(3.7×10^{-9} ppt cm^{-1}) should decrease to zero in 750 km, a not unreasonable prospect judging from the figure.

Hence, in the Cluster A and B area it appears that in the low thermocline (900-1300 m) low salinity South Atlantic Water moves northward, into the local salinity maximum of the Mediterranean tongue, gaining salinity as it travels. This northward movement is consistent with Worthington's (1976) hypothesis that the Gulf Stream return flow is confined northwest of the 35.2 ppt isohaline at 6°C (Fig. 8). Above this, in the mid-thermocline, high salinity Western North Atlantic Water moves north and down into the low salinity South Atlantic Water, losing salinity.

At Cluster C, the Antarctic Intermediate Water (AAIW) found from 500-1000 m moves northward, gaining heat and salinity (see Fig. 7c) as it moves. This heat and salinity convergence could be driven by a downward flux of heat and salt from the warm, salty sub-tropical underwater (SUW) above it, driven by a double-diffusive process. Schmitt and Evans (1978) analyzed an area at 16°15'N, 57°13'W (about 300 km west of Cluster C) and found "steppy" temperature and salinity profiles characteristic of salt fingering (see, for example, Turner, 1973) at depths from 300 to 500 m. We ourselves, during the 1978 Cluster C recovery cruise, observed extensive step structure from 400 to 600 m. Schmitt and Evans (1978) suggest that salt fingers grow sufficiently fast to avoid disruption by the internal wave field when $\alpha T_z/\beta S_z \leq 2$, where $\alpha = \partial\rho/\partial T$, $\beta = \partial\rho/\partial S$. Using this criterium, the temperature and salinity fields at Cluster C would be unstable to fingering at depths from 300 to 700 m with the maximum instability at

500 m ($\alpha T_z/\beta S_z = 1.5$).

Such a process could also operate at Clusters A and B where the criterium $\alpha T_z/\beta S_z \leq 2$ is marginally satisfied from 400 to 600 m and 300-600 m, respectively. However, $\dot{Q}_\theta$ and $\dot{Q}_s$ are negative at Cluster A and only slightly positive at Cluster B at these depths. These depths are probably marginally unstable to fingering.

The two clusters on the western side of the mid-Atlantic Ridge (A and C) have similar deep water motions. Water moves north, west, and down into the fresher and colder Antarctic Bottom water underlying it.

Cluster B is very near the locations studied by Schott and Stommel (1978), Behringer (1979) and Behringer and Stommel (1980) using the β-spiral technique. The equilateral triangle used by Behringer and Stommel is shown on Figure 1.

As indicated in Section 2, the quantity $\frac{\partial}{\partial z}(\dot{Q}_{\tilde{\rho}}/\frac{\partial \tilde{\rho}}{\partial z})$ vanishes where $\frac{\partial \tilde{w}}{\partial z} = \frac{\partial \bar{w}}{\partial z}$ in Figure 4, i.e. where the two lines are parallel. The β-spiral method (which in general can incorporate non-zero potential vorticity dissipation if it is known) should render appropriate values of u_o and v_o in these regions. From Figure 4, this includes 200 to 600 m and 1500 to 2500 m at Clusters A and B. However, in these levels, Stommel and Armi (1980, private communication) find no significant horizontal gradients of potential vorticity and the β-spiral method will be ill-conditioned for determining horizontal velocity. Between 600 and 1500 m our analysis shows that a turbulent flux of potential vorticity exists. While horizontal potential vorticity gradients also occur and it should be possible to use the

β-spiral method, its application in the presently used form is not physically valid. We have had a similar experience in applying conservation of potential vorticity for determining u_o, v_o in the circumpolar Current in the Drake Passage (Niiler and Spillane, 1977, private communication). There, potential vorticity gradients also vanish in the homogeneous water mass below 1000 m. Gradients exist above 1000 m but this area is obviously a sinking and strongly mixing region of the Antarctic Intermediate water. Clearly, an inverse method for determining u_o and v_o is needed which determines both advection and diffusion together in a best fit sense, and perhaps minimizes the fields with respect to diffusion coefficients of many trace constituents across and along isopycnals.

Appendix A: Error Analysis

To derive an estimate of the standard error of the density (or temperature, salinity) gradient at a depth, we assume that all density measurements are independent at that depth. This is practical because most of the observations were taken at widely different times, eliminating the possibility of horizontal correlations due to eddy aliasing. The quality of the plane fits can then be related to a standard error of the horizontal density gradient (Draper and Smith, 1966).

The gradients and errors were then converted to vertical shear using the thermal wind relation and then vertically integrating to find velocity:

$$v_n = \sum_{i=r_H}^{n} \lambda_i v_{z_i} + v_{ref} \tag{A.1}$$

where: v_n is the velocity (u or v) at level n

v_{z_i} is the shear at level i

r_H is the reference level for horizontal velocity

v_{ref} is the reference velocity at level $i=r_H$

$\lambda_i = \frac{z_{i+i} - z_{i-1}}{2}$

z_i is the depth of level i for $i \neq r_H-1$ or n+1

$z_{r_H-1} \equiv z_{r_H}$

$z_{n+1} \equiv z_n$.

The variance of v_n is given by:

$$\mathrm{Var}\{v_n\} = \sum_{i=r_H}^{n} \sum_{j=r_H}^{n} \lambda_i \lambda_j \, \mathrm{Cov}\{v_{z_i}, v_{z_j}\}. \tag{A.2}$$

We assume that the shears are pairwise independent, i.e. $\mathrm{Cov}\{v_{z_l}, v_{z_j}\} = 0$, $i \neq j$. This will not be true to the extent that measurements within a cast are correlated by, for example, an internal wave. However, the shears involve many different casts and so it was felt that correlations within a cast would not be sufficient to cause covariance between the shears. Hence, (A.2) becomes:

$$\mathrm{Var}\{v_n\} = \sum_{i=r_H}^{n} \lambda_i^2 \, \mathrm{Var}\{v_{z_i}\} \tag{A.3}$$

Calculation of vertical velocity using the Sverdrup relation requires integration of the meridional velocity profile:

$$w_n = \frac{\beta}{f} \sum_{i=r_w}^{n} \lambda_i v_i + w_{ref} \tag{A.4}$$

where: w_n is the vertical velocity at level n

v_i is the meridional velocity at level i

r_w is the reference level for vertical velocity

w_{ref} is the vertical reference velocity at level $i=r_w$

λ_i is as defined in (A.1).

Again the variance of this sum of random variables is given by:

$$\mathrm{Var}\{w_n\} = \sum_{i=r_w}^{n} \sum_{j=r_w}^{n} \lambda_i \lambda_j \, \mathrm{Cov}\{v_i, v_j\}. \tag{A.5}$$

Here, however, the integrands (v_i) are highly correlated, being sums of the same shears. We assume, first, that velocities on opposite sides of the horizontal reference level (r_H) are uncorrelated because they involve completely different sums of shears. Secondly, we assume that velocities on the same side of the reference level share the variance of the velocity closest to the reference level, i.e.:

$$\mathrm{Cov}\{v_i, v_j\} = \mathrm{Var}\{v_k\}$$

where: $k=i$ if $|i-r_H| < |j-r_H|$

$k=j$ if $|i-r_H| > |j-r_H|$.

All of the covariances were then summed to give an estimate of the variance of w_n.

Estimates of the variance of the eddy convergences were then derived using an approximation for the variance of the product of two random variables:

$$\mathrm{Var}\{X_1, X_2\} \simeq \mu_1^2 \mathrm{Var}\{X_2\} + \mu_2^2 \mathrm{Var}\{X_1\} + 2\mu_1\mu_2 \mathrm{Cov}\{X_1, X_2\} \qquad (A.7)$$

where: μ_1 is the mean of X_1,

μ_2 is the mean of X_2.

It was assumed that the covariances of a velocity component with the gradient in that direction was zero, e.g. $\mathrm{Cov}\{u, T_x\} = 0$. Hence:

$$\begin{aligned}\mathrm{Var}\{\overline{\dot{Q}_\theta}\} \simeq\ & u^2 \mathrm{Var}\{T_x\} + T_x^2 \mathrm{Var}\{u\} \\ & + v^2 \mathrm{Var}\{T_y\} + T_y^2 \mathrm{Var}\{v\} \\ & + w^2 \mathrm{Var}\{\theta_z\} + \theta_z^2 \mathrm{Var}\{w\}. \end{aligned} \qquad (A.8)$$

REFERENCES

ANONYMOUS (1974) User's guide to NODC's data services. United States Government Printing Office, 72 pp.

BEHRINGER D. W. (1979) On computing the absolute geostrophic velocity spiral. Journal of Marine Research, 37,459-470.

BEHRINGER D. W. and H. STOMMEL (1980) The beta spiral in the North Atlantic subtropical gyre. Deep-Sea Research, 27,225-238.

BRYDEN H. L. (1976) Horizontal advection of temperature for low-frequency motions. Deep-Sea Research, 23,1165-1174.

DAVIS R. A. (1978) On estimating velocity from hydrographic data. Journal of Geophysical Research, 83,5507-5509.

DRAPER N. R. and H. SMITH (1966) Applied regression analysis. John Wiley and Sons, 407 pp.

FU L., T. KEFFER, P. P. NIILER and C. WUNSCH (1980) Low-frequency motions observed in POLYMODE Array III: The Mid-Atlantic Ridge and the Atlantic North-Equatorial Current. In preparation.

HIDAKA K. (1940) Absolute evaluation of ocean currents in dynamical calculation. Proceedings of the Imperial Academy of Japan, 16,391-393.

LEETMA A. and A. BUNKER (1978) Updated charts of the mean annual wind stress, convergences in the Ekman layers, and Sverdrup transports in the North Atlantic. Journal of Marine Research, 36,311-322.

NEEDLER G. T. and R. A. HEATH (1975) Diffusion coefficients calculated from the Mediterranean salinity anomaly in the North Atlantic ocean. Journal of Physical Oceanography, 5,173-182.

NIILER, P. P. and R. REYNOLDS (1980) Circulation around the Eastern North Pacific Sub-Tropical Front. Unpublished manuscript.

SCHOTT F. and H. STOMMEL (1978) Beta spirals and absolute velocities in different oceans. Deep-Sea Research, 25,961-1010.

SCHMITT R. W. and D. L. EVANS (1978) An estimate of the vertical mixing due to salt fingers based on observations in the North Atlantic Centeral Water. Journal of Geophysical Research, 83,2913-2920.

STOMMEL, H. (1956) On the determinination of the depth of no meridional motion. Deep-Sea Research, 3,273-278.

STOMMEL, H. and F. SCHOTT (1977) The beta spiral and the determination of the absolute velocity field from hydrographic station data. Deep-Sea Research, 24,325-329.

SUDD H. (1965) An analysis of the deep current of the ocean; with its application to the circulation of the Atlantic Ocean. Japanese Journal of Geophysics, 4,1-70.

WORTHINGTON L. V. (1976) On the North Atlantic circulation. Johns Hopkins University press, 110 pp.

WUNSCH C. (1978) The North Atlantic general circulation west of 50°W determined by inverse methods. Reviews of Geophysics and Space Physics, 16,583-620.

Captions

Figure 1. The hydrographic stations used to find horizontal density, temperature, and salinity gradients are denoted by (+), the POLYMODE moorings are shown as small triangles (▲). The large triangle is the location of the data set used by Behringer and Stommel (1980).

Figure 2. Absolute zonal velocity profiles at (a) Cluster A, (b) Cluster B, and (c) Cluster C. The dashed line is the estimated standard error. The crosses are means from direct measurements using current meters. Also shown at each level where there was more than one current meter is the overall average and estimated standard error. In (c) the mean vertical shear estimated from mean horizontal temperature gradients as measured by the current meters is indicated as sloping lines.

Figure 3. Absolute meridional velocity profiles at (a) Cluster A, (b) Cluster B, and (c) Cluster C. Other features as in Figure 2.

Figure 4. Hodographs at (a) Cluster A, (b) Cluster B, and (c) Cluster C. The dashed lines in (a) and (b) are the estimated hodographs from Schott and Stommel (1978) and Behringer and Stommel (1980), respectively.

Figure 5. The solid line ($\bar{w}$) is the vertical velocity as determined from the vertical integration of the first order vorticity equation (2.1c). Also shown is the estimated standard error. The dashed line ($\tilde{w}$) is the vertical velocity estimated from potential density conservation (Eqn. 2.4).

Figure 6. Divergence of potential density from mean motions at (a) Cluster A, (b) Cluster B, and (c) Cluster C. Estimates of the standard error are shown. Crosses are estimates of horizontal eddy convergence of density from current meters.

Figure 7. Potential temperature and salinity divergence from mean motions ($\dot{Q}_\theta$, $\dot{Q}_S$, respectively) at (a) Cluster A, (b) Cluster B, and (c) Cluster C. Estimates of the standard error are shown.

Figure 8. Salinity on the 6°C surface in the North Atlantic (from Worthington, 1976). Also shown are the absolute velocity (solid) and salinity (dashed) gradient vectors at the appropriate depths (1150, 1250, 800 m at Clusters A, B, C, respectively).

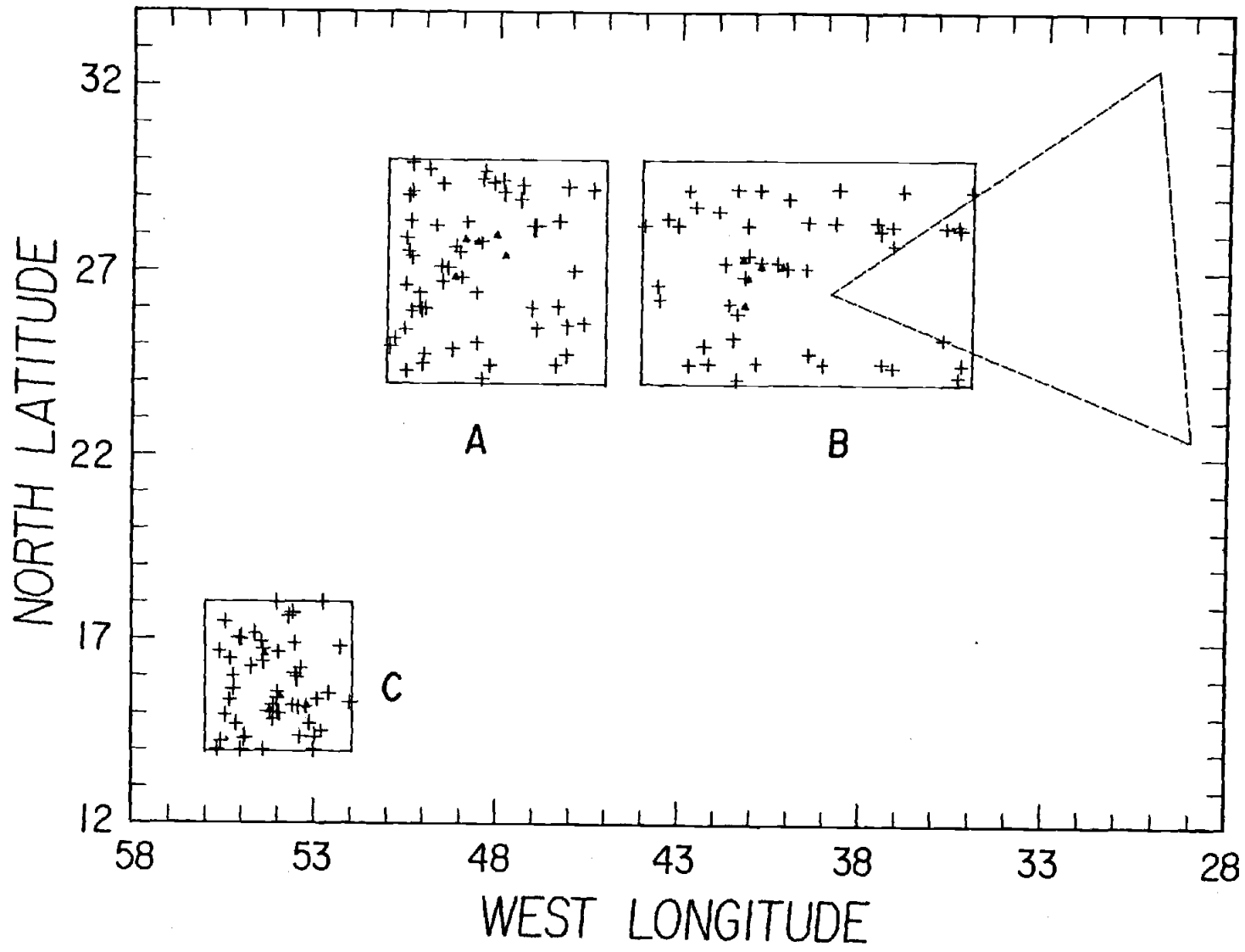
NORTH LATITUDE
32
27
22
17
12
58
53
48
43
38
33
28
WEST LONGITUDE
A
B
C

Figure 1

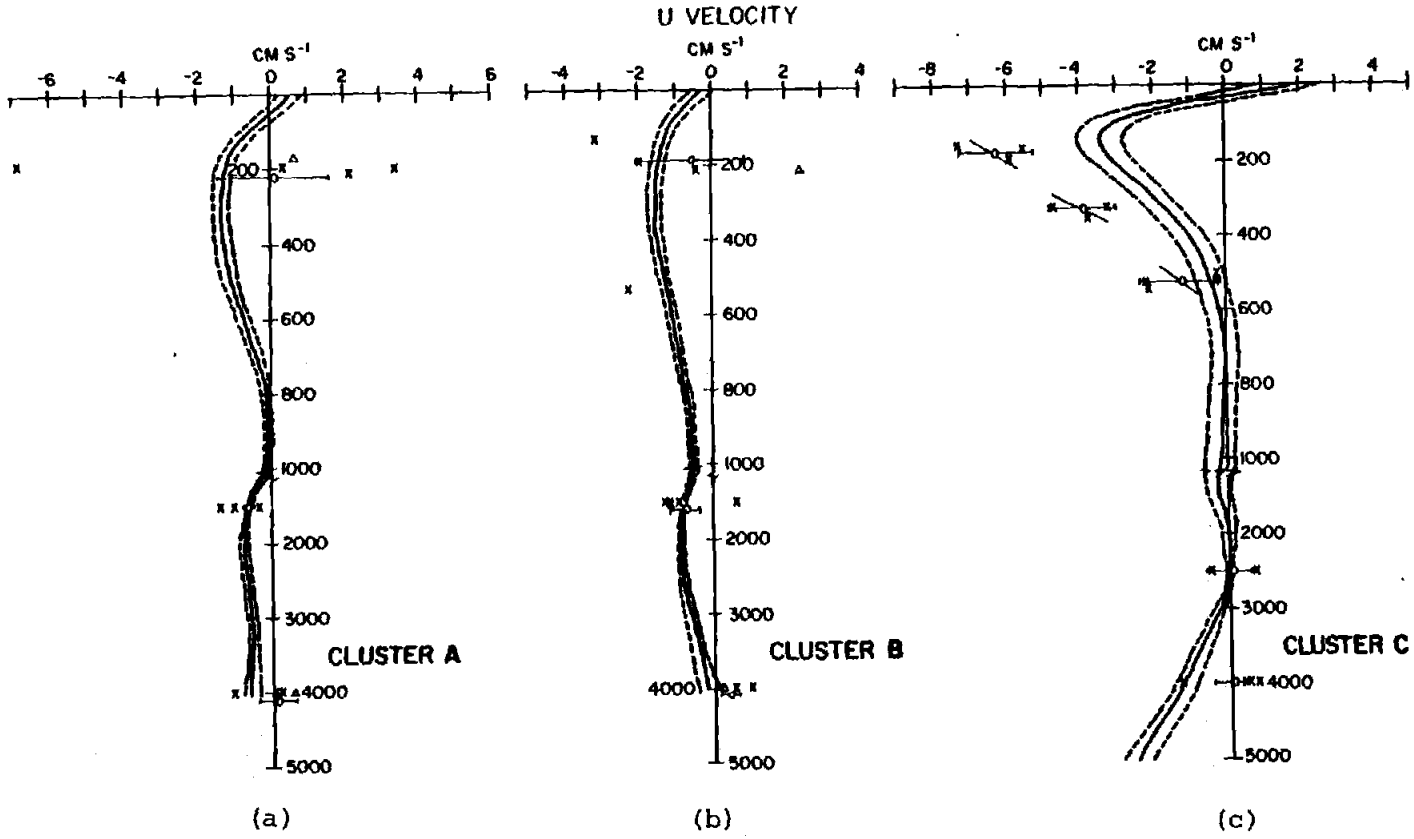
U VELOCITY
CM S-1
-6
-4
-2
0
2
4
6
200
400
600
800
1000
2000
3000
4000
5000
CLUSTER A
(a)
CM S-1
-4
-2
0
2
4
200
400
600
800
1000
2000
3000
4000
5000
CLUSTER B
(b)
CM S-1
-8
-6
-4
-2
0
2
4
200
400
600
800
1000
2000
3000
4000
5000
CLUSTER C
(c)

Figure 2

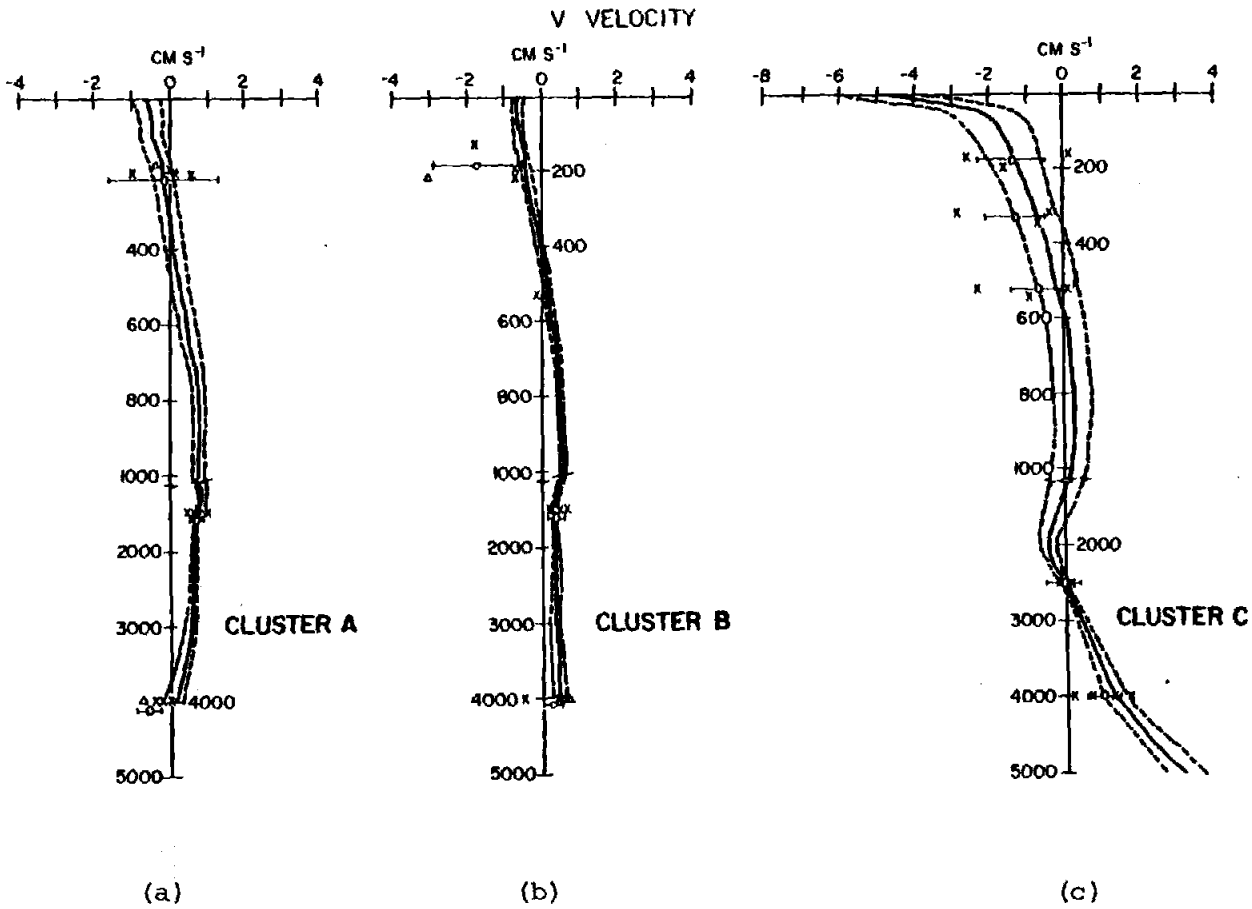
V VELOCITY
CM S⁻¹
-4
-2
0
2
4
200
400
600
800
1000
2000
3000
4000
5000
CLUSTER A
CLUSTER B
-8
-6
CLUSTER C
(a)
(b)
(c)

Figure 3

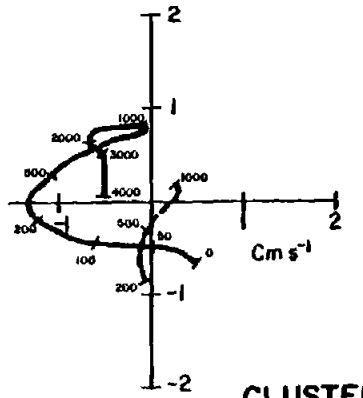

CLUSTER A

(a)

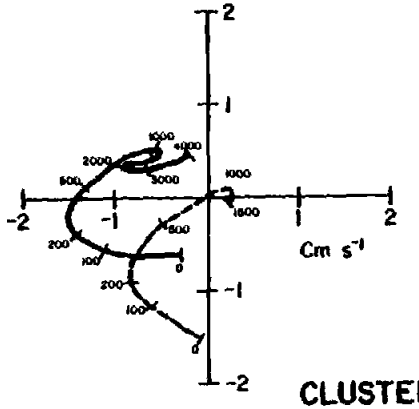

CLUSTER B

(b)

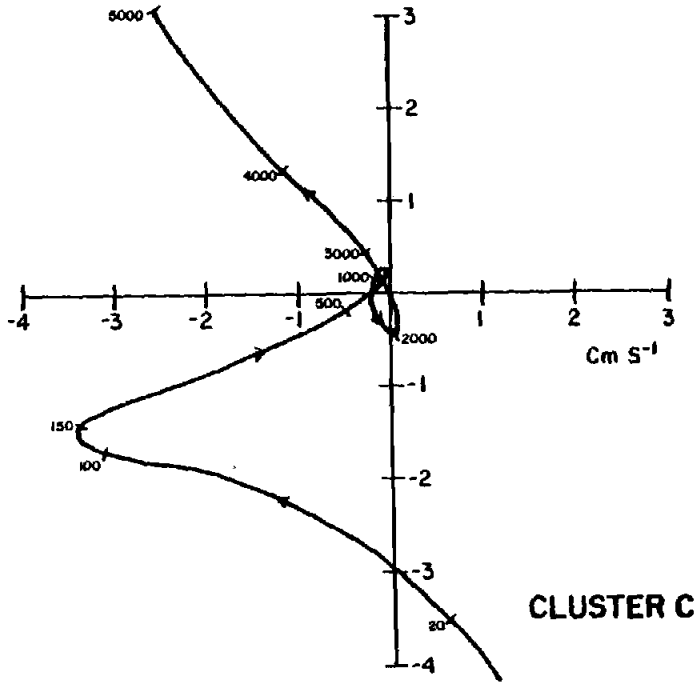

CLUSTER C

(c)

Figure 4

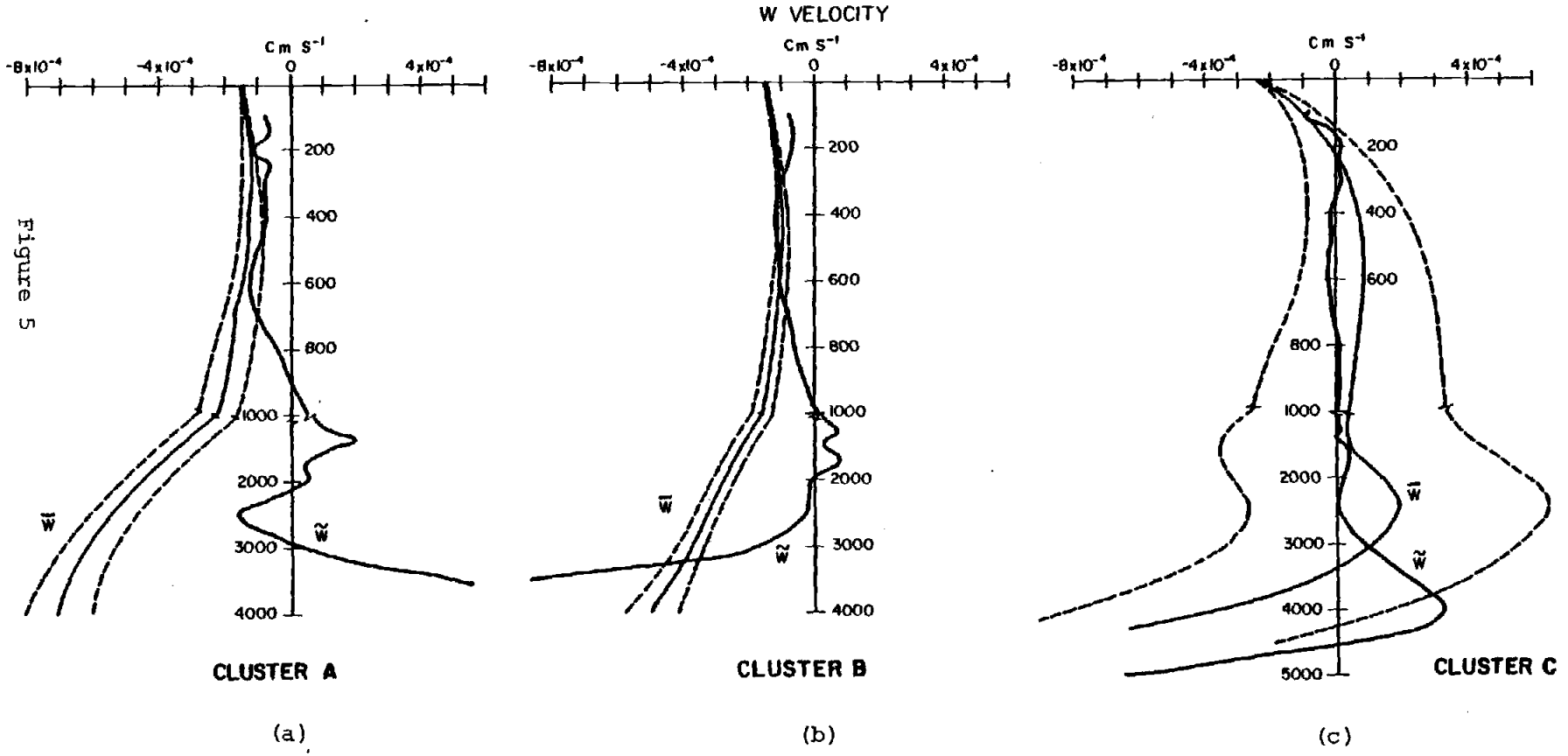
W VELOCITY
Cm S⁻¹
-8x10⁻⁴
-4x10⁻⁴
0
4x10⁻⁴
200
400
600
800
1000
2000
3000
4000
5000
CLUSTER A
CLUSTER B
CLUSTER C
(a)
(b)
(c)

Figure 5

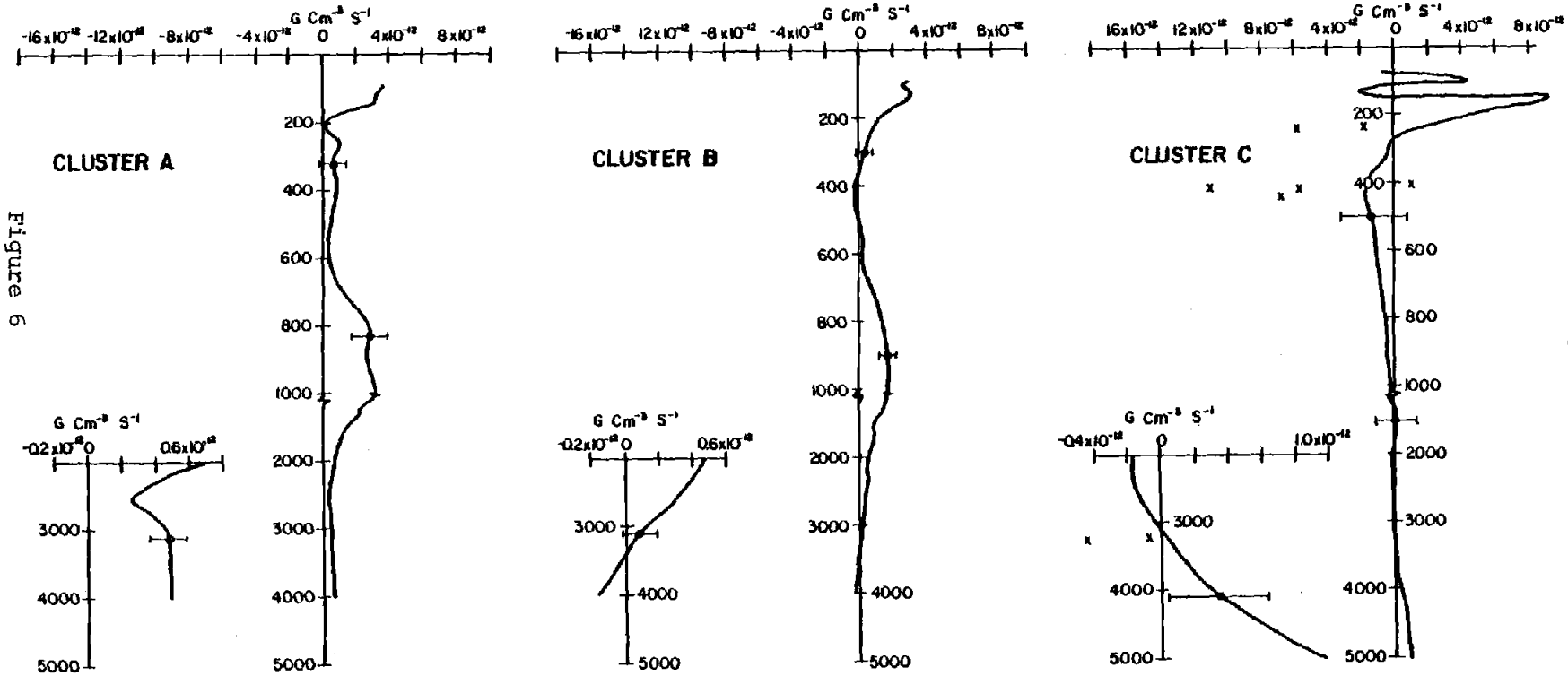
CLUSTER A
CLUSTER B
CLUSTER C
G Cm⁻³ S⁻¹
-16x10⁻¹² -12x10⁻¹² -8x10⁻¹² -4x10⁻¹² 0 4x10⁻¹² 8x10⁻¹²
-0.2x10⁻¹² 0 0.6x10⁻¹²
-0.4x10⁻¹² 0 1.0x10⁻¹²
200
400
600
800
1000
2000
3000
4000
5000
(a)
(b)
(c)

Figure 6

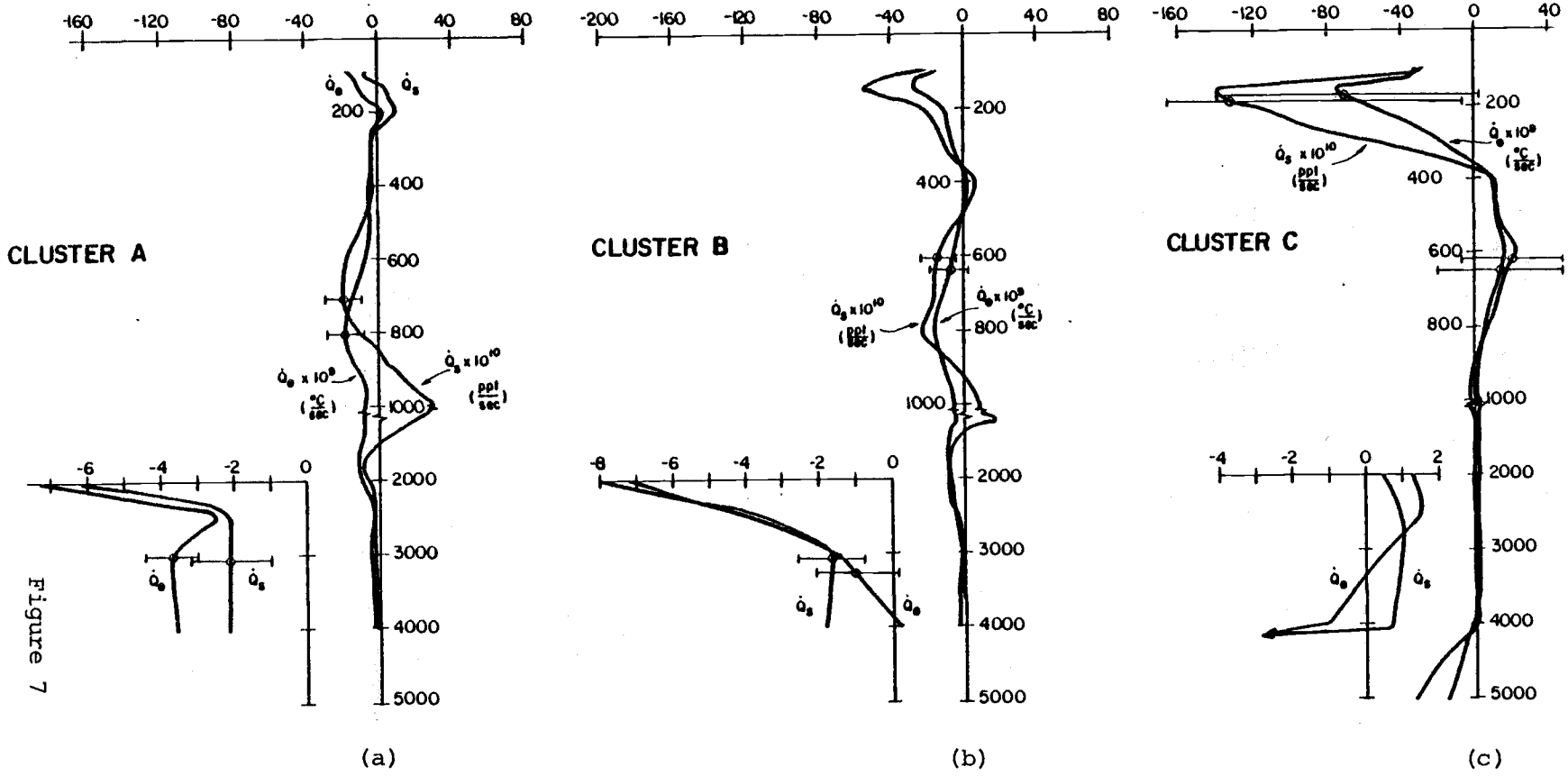

Figure 7

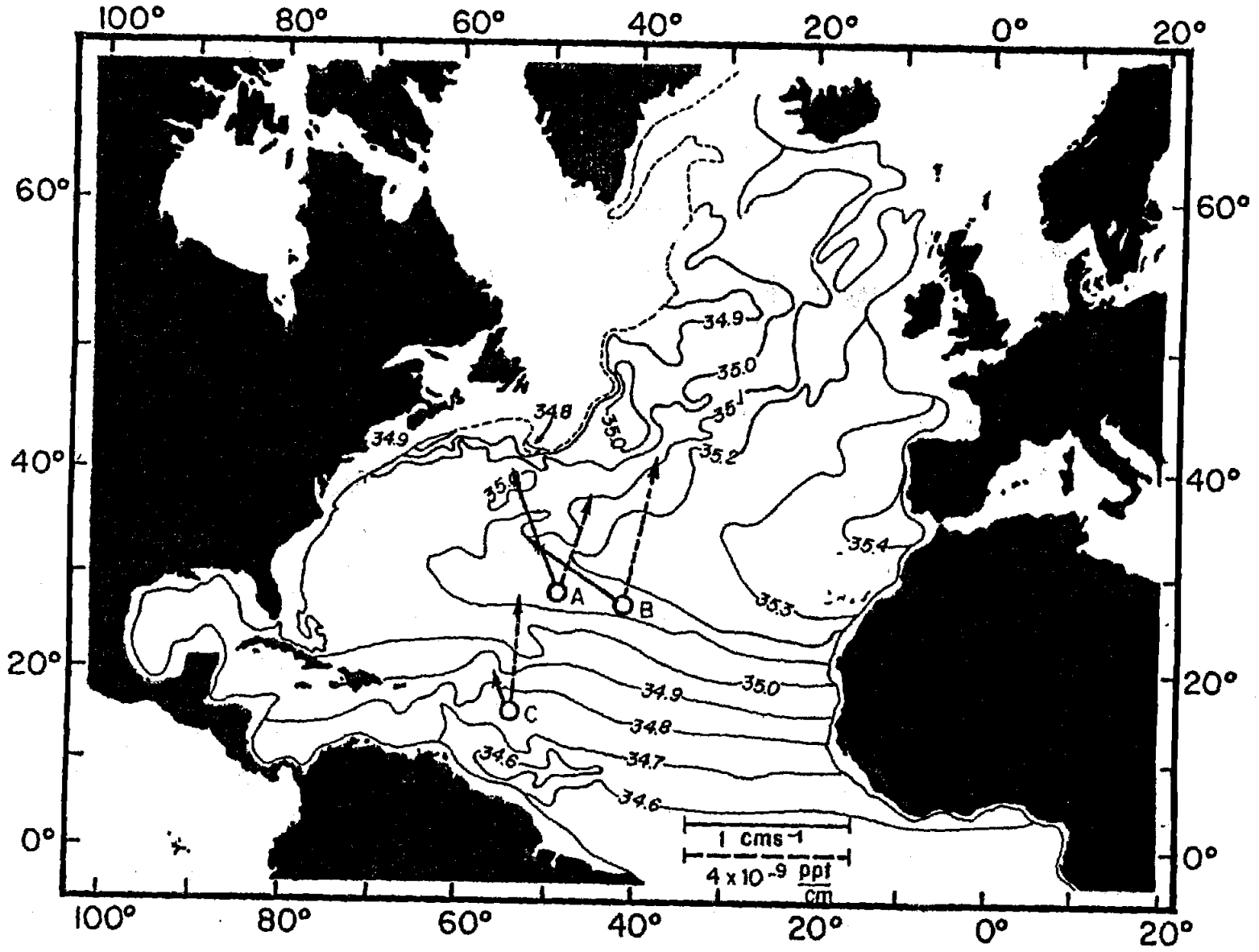
100°
80°
60°
40°
20°
0°
20°
60°
40°
20°
0°
34.9
35.0
35.1
35.2
34.8
35.0
34.9
35.3
35.4
35.3
A
B
C
34.9
35.0
34.8
34.7
34.6
34.6
1 cms⁻¹
4 x 10⁻⁹ ppt/cm

Figure 8

Chapter IV

Time Dependent Temperature and Vorticity Balances in the Atlantic North Equatorial Current

by

Thomas Keffer

School of Oceanography

Oregon State University

Corvallis, Oregon 97331

October 1980

Abstract

The POLYMODE Array III Cluster C data set was tested for consistency with linearized heat and vorticity equations in four frequency bands at three depths to test the impact of the non-linear terms. The amplitude and phasal relations predicted by the linear heat equation were found to be operating with additional inputs from non-linear terms. Relative vorticity changes were found to be balanced by advection of planetary vorticity in the low-frequency (324-81 days), within the estimated errors. Advection of vorticity was found to be important at mid-frequencies (65-30 days) and stretching important at high-frequencies (28-4 days). The velocity field was found to be horizontally non-divergent within the rather large sampling errors. Finally, the baroclinic instability model of Gill, Green and Simmons was tested for predicted growth rates and modal structure.

1. Introduction

One traditional model of fluctuations in the ocean is to expand the velocity and temperature fields as the sum of a set of normal Rossby-wave modes (Rhines, 1977). Some studies have either ignored mean flow and balanced the local change of temperature with vertical advection of the mean temperature gradient (Kundu, Allen and Smith, 1975; McWilliams and Flierl, 1976) or explicitly included the mean flow (McWilliams and Robinson, 1973; Gill, Green and Simmons, 1974, hereafter referred to as GGS; Robinson and McWilliams, 1974).

However, while all models include vertical temperature advection, Bryden (1976), using the IWEX data set, showed that not only was horizontal advection important, but that within the errors of his analysis it could completely balance the local change of temperature. He suggested that a linearization that includes the mean flow and horizontal temperature gradients is more appropriate. In this study, horizontal advection is Reynold's decomposed into linear and non-linear components and their relation to each other and the local time change of temperature is studied. Furthermore, use of the more extensive Polymode Cluster C data set allows Bryden's analysis to be carried out in different frequency bands and different depths. It is found that horizontal advection balances the local temperature change only in the mid-thermocline and at mid-frequencies (30-65 day period), although it is an important term at other depths and at lower frequencies. Furthermore, the nature of the balance is primarily linear. At higher frequencies horizontal advection is found to play a minor role.

In a separate paper, Bryden and Fofonoff (1977), estimated horizontal velocity gradients by finite differencing velocity between moorings. The velocity field was found to be horizontally non-divergent within their errors. The velocity gradients were also used to estimate vorticity. It was found that advection of planetary vorticity could only explain one half of the vorticity changes. Although direct estimates of vertical stretching from horizontal divergence were not found to be correlated with the remaining vorticity changes, indirect estimates from a linear heat balance were. However, other evidence, such as the importance of non-linear heat advection, suggested that advection of vorticity could also be important.

The test of horizontal non-divergence was applied to the Cluster C data set. Although u_x was not found to be correlated with v_y, their sum was still found to be less than the estimated sampling error due to the peculiar design of the Cluster C array.

Estimates of vorticity were found to be highly coherent with estimates of time integrated advection of planetary vorticity in the lowest frequency band. In the highest frequency bands (4-27 days) stretching was found to be highly important while at intermediate frequencies advection of vorticity was important.

The Cluster C area is characterized by a northward temperature gradient representing a supply of potential energy that is available to be converted into eddy energy if an appropriate mechanism is available. A downgradient (south) temperature flux and an upward phase propagation is necessary to tap this reservoir. That is, a southward velocity should correlate with warmer temperatures and

motion should occur first at depth and "propagate" upwards. However, Fu, Keffer, Niiler and Wunsch (1980, hereafter referred to as FKNW) found temperature fluxes that were more nearly across-gradient (eastward) and only occasionally southwards. Furthermore, there was only slight evidence of upward phase propagation. In this study the baroclinic instability model of GGS is found to predict similar phase changes and a consistent mode shape but larger heat fluxes. The model also selects smaller scales than the observed scales.

Horizontal and vertical coherence scales as well as eddy heat fluxes, phase propagation and observed potential and kinetic energy distributions of the three clusters in POLYMODE Array III are discussed in FKNW. Mean density, temperature, salinity, and vorticity balances are discussed in Keffer and Niiler (1980)

Temperature

In the absence of heating and cooling, the conservation of temperature can be written as:

$$T_t + uT_x + vT_y + w\theta_z = 0 \tag{2.1}$$

where T is temperature, t is time, (u,v,w) is current velocity in the (x,y,z) (east, north, upwards) direction, θ_z is the instantaneous vertical adiabatic temperature gradient and subscripts denote differentiation.

A locally tight temperature/salinity relation allows the thermal wind relations to be written:

$$T_x = \frac{1}{\alpha}\rho_x = -\frac{f\rho_o}{g\alpha} v_z + O(\varepsilon) + O(\delta) + O(\gamma) \tag{2.2}$$

$$T_y = \frac{1}{\alpha}\rho_y = \frac{f\rho_o}{g\alpha} u_z + O(\varepsilon) + O(\delta) + O(\gamma) \tag{2.3}$$

where ρ is density, f is the Coriolis parameter, g is the gravitational acceleration, and α relates temperature to density:

$$\alpha = \left(\frac{\partial\bar{\rho}}{\partial T} + \frac{\partial\bar{\rho}}{\partial S}\frac{d\bar{s}}{dT}\right) = \frac{d\bar{\rho}}{dT}. \tag{2.4}$$

The non-dimensional parameters ε, γ, δ measure the ratio of nonlinear effects to geostrophic effects, inertial effects to geostrophic effects, and non-hydrostatic to hydrostatic effects:

$$\varepsilon = \frac{u}{Lf} \qquad \gamma = \frac{1}{\tau f} \qquad \delta = \max\left(\frac{H^2}{L^2}\varepsilon, \frac{H^2}{L^2}\gamma\right)$$

For Cluster C, u = 5 cm s^{-1}, L = 80 km, f = 0.4 x 10^{-4} s^{-1}, and H = 1 km. The parameter τ measures a time scale. Thus for 10 day time scales:

$$\varepsilon = .016, \quad \gamma = .029, \quad \text{and} \quad \delta = 2.5 \times 10^{-6}$$

The maximum frequencies considered in this study is 0.25 cpd (τ = .65 days) which gives:

$$\gamma = .45 \quad \delta = 7 \times 10^{-5}$$

Thus the thermal wind relations range from an excellent approximation in the low-frequency to fair in the higher frequencies. This allows the second and third terms in (2.1) to be written:

$$u\,T_x + v\,T_y = \frac{f\rho_o}{g\alpha}\,(-uv_z + vu_z) \tag{2.5}$$

Eqn. (2.5) can be further Reynolds' decomposed into mean (denoted by overbar) and fluctuating or eddy (prime) components:

$$\begin{aligned} u\,T_x + v\,T_y = \frac{f\rho_o}{g\alpha}\{&-\bar{U}\bar{V}_z - \bar{U}v_z' - u'\bar{V}_z - u'v_z' \\ &(\bar{U}\bar{T}_x)\ (\bar{U}T_x')\ (u'\bar{T}_x)\ (u'T_x') \\ &+ \bar{V}\bar{U}_z + \bar{V}u_z' + v'\bar{U}_z + v'U_z'\} \\ &(\bar{V}\bar{T}_y)\ (\bar{V}T_y')\ (v'\bar{T}_y)\ (v'T_y') \end{aligned} \tag{2.6}$$

where the corresponding term in the temperature balance has been written below. Six terms can contribute to the time dependent balance ($\bar{U}T_x'$, $u'\bar{T}_x$, $u'T_x'$, $\bar{V}T_y'$, $v'\bar{T}_y$, $v'T_y'$) and four to a mean horizontal advection ($\bar{U}\bar{T}_x$, $\overline{u'T_x'}$, $\bar{V}\bar{T}_y$, $\overline{v'T_y'}$). In the traditional linear models of baroclinic instability of a zonal shear flow, two time dependent terms are retained: $\bar{U}T_x'$ and $v'\bar{T}_y$ (GGS). Two others are dropped because of the small mean meridional velocity and small mean zonal temperature gradient: $\bar{V}T_y'$ and $u'\bar{T}_x$. The two non-linear terms ($u'T_x'$ and $v'T_y'$) are dropped because they are considered small during the initial stages of eddy growth. Finally, the vertical advection of temperature is represented as a fluctuating upward

velocity advecting a mean vertical potential temperature gradient: $w'\bar{\theta}_z$.

The temperature balance in the shear flow is written as:

$$T_t' + \bar{U}T_x' + v'\bar{T}_y + w'\bar{\theta}_z = 0 \qquad (2.7)$$

The thermocline of the Cluster C area closely parallels this linear model. The mean horizontal temperature gradient is nearly due north and the mean flow is nearly zonal (FKNW). Because the zonal fluctuations are at least as large as the zonal mean flow, the term $u'T_x'$ can be expected to be as large as $\bar{U}T_x'$. Furthermore, the mean zonal shear ($\nabla\bar{T}_y$) is of similar size to the fluctuations of shear ($\nabla T_y'$) implying that $v'\bar{T}_y$ and $v'T_y'$ will be of similar size. Nonetheless, the balances suggested by the linear balance may be operating with additional contributions from the non-linear terms. For example, the change of local temperature (T_t') may consist of contributions predicted by the linear model, as well as additional non-linear contributions. We now consider the nature of the linear balance.

The geostropic and hydrostatic approximations allow the introduction of the disturbance stream function:

$$\psi(x,y,z,t) = \mathrm{Re}\,\{A(z)e^{i(kx + ly - \omega t - \phi(z))}\} \qquad (2.8)$$

where A(z) is the real vertical structure function, $\phi(z)$ is the relative phase, (k,l) is the horizontal wavenumber vector, and $\omega (= \omega_r + i\omega_i)$ is the complex frequency. If $\omega_i > 0$ (<0) the wave will be growing (decaying). The terms u', v', T', w' are written as:

$$u' = -\psi_y$$

$$v' = \psi_x \tag{2.9}$$

$$T' = -\frac{f\rho_o}{g\alpha}\psi_z$$

$$w' = -(T_t' + \bar{U}T_x' + v'\bar{T}_y)/\bar{\theta}_z .$$

Substitution of (2.8) and (2.9) into the temperature equation allows evaluation of the relative amplitudes and phases of each of the terms. The rms amplitude of T_t' averaged over a cycle is

$$\text{rms}[T_t'] = \frac{f\rho_o}{\sqrt{2}g\alpha}(\omega_r^2 + \omega_i^2)^{1/2}\,[A_z^2 + A^2\phi_z^2]^{1/2}$$

which for a slowly growing or decaying wave (e-folding time comparable or longer than a period) is approximately,

$$\text{rms}[T_t'] = \frac{f\rho_o}{\sqrt{2}g\alpha}\omega_r[A_z^2 + A^2\phi_z^2]^{1/2} . \tag{2.10}$$

The phase is given by

$$\arg[T_t'] = \arg\{A_z[(\omega_i - \eta\omega_r) - i(\eta\omega_i + \omega_r)]\} \tag{2.11}$$

where $\eta = \frac{A\phi_z}{A_z}$ and it was assumed $\alpha < 0$. Note that although FKNW found only small vertical phase changes in Cluster C, ϕ_z enters as η which may not be small. Similarly,

$$\text{rms}[\bar{U}T_x'] = \frac{f\rho_o}{\sqrt{2}g\alpha}k\bar{U}\,[A_z^2 + A^2\phi_z^2]^{1/2} \tag{2.12}$$

$$\arg[\bar{U}T_x'] = \arg[k\bar{U}A_z(\eta + i)] \tag{2.13}$$

The ratio of the amplitudes of T_t' to $\bar{U}T_x'$ is

$$\frac{\text{rms}[T_t']}{\text{rms}[\bar{U}T_x']} = \frac{\omega_r}{k\bar{U}} \tag{2.14}$$

while the relative phase difference will be:

$$\arg[T_t'] - \arg[\bar{U}T_x'] = \arg[-\omega_r - i\omega_i] \tag{2.15}$$

Thus the ratio of amplitudes will depend on the proximity to the critical layer. Within the layer, $\frac{\omega_r}{k} = \bar{U}$ and the ratio becomes one. The extent to which the two terms are not 180° out of phase will depend on the stability. For a growing wave T_t' will lead with an angle $-180° < \phi < 0$, while for a decaying wave, $0° < \phi < 180°$. A neutral wave has $\phi = 180°$. In practice, because $\omega_i << \omega_r$, it would be difficult to observe the small difference from $\phi = 180°$.

Phases between other components are, in general, more complicated because of dependence on the parameter η. The phase difference between $\bar{U}T_x'$ and $v'\overline{T_y}$ is, for example:

$$\arg[\bar{U}T_x'] - \arg[v'\overline{T_y}] = \arg\left[\frac{f\rho_o}{g\alpha}\frac{\omega_r A_z}{kA\bar{T}_y}(1 - \eta i)\right] \tag{2.16}$$

Which half-plane the phase is in will depend on the sign of A_z, where in the half-plane will depend on η. In Section 4 an estimate of η is made in the upper-thermocline and is found to be consistent with other phase relations that use it.

Vorticity

The equation for conservation of the vertical component of vorticity ($\zeta = v_x - u_y$) is

$$\zeta_t + \underset{\sim}{u} \cdot \nabla\zeta + \beta v = f w_z \qquad (2.17)$$

$$\left(\frac{u}{L\tau}\right) \quad \left(\frac{u^2}{L^2}\right) \qquad (\beta v)$$

where it was assumed $f >> \zeta$ and the expected size of each term is written underneath. For $u = 5$ cm s^{-1}, $L = 75$ km, $\tau = 10$ days, $\beta = 2.2 \times 10^{-13}$ cm^{-1} s^{-1} all terms on the left-hand side are of order 7×10^{-13} s^{-2}, implying that the right-hand side will be too. Hence, we expect all terms to be important. However, only three (ζ_t, βv, $f w_z$) can be estimated directly from the Cluster C velocity and temperature data while the fourth ($\underset{\sim}{u} \cdot \nabla\zeta$) would require at least an additional mooring in principle (and probably several in practice) to directly estimate. We can only infer its existence by showing that the sum of the other terms is greater than their expected error.

Stability

In FKNW it was indicated that on the time scale of the observation period, the eddy field was generally stable or slowly growing, although localized rapid growth was possible. That is, the average e-folding time is comparable to one year. The linear model of GGS allows prediction of eddy growth times as a function of wavenumber for a given mean $\bar{U}$ velocity profile and mean north-south potential vorticity gradient (Q_y), as well as the vertical structure of the disturbance streamfunction. One would like to know whether the linear model would predict such slow growth rates or whether non-linear, finite-amplitude dynamics have come into play.

Substitution of the plane wave (2.8) into the linearized version of (2.17) give the vorticity equation:

$$\left(\frac{\partial}{\partial t} + \bar{U}\frac{\partial}{\partial x}\right)\left(\nabla_H^2 \psi + \left(\frac{f_o^2}{N^2}\psi_z\right)_z\right) + \psi_x Q_y = 0 \qquad (2.18)$$

where $Q_y = \beta - (f^2\bar{U}_z/N^2)_z$, gives an eigenvalue problem for the complex vertical structure function $F(z)$:

$$(\bar{U} - \frac{\omega}{k})\left\{\left(\frac{f^2}{N^2}F_z\right)_z - (k^2 + l^2)F\right\} + Q_y F = 0 \qquad (2.19)$$

where ω is the complex eigenvalue. The boundary conditions are:

$$F_z(\bar{U} - \frac{\omega}{k}) = \bar{U}_z F \qquad \text{at } z = 0 \qquad (2.20a)$$

$$F_z(\bar{U} - \frac{\omega}{k}) = (\bar{U}_z - \frac{N^2 h_y}{f})F \qquad \text{at } z = -H. \qquad (2.20b)$$

A mode with $\omega_i > 0$ will grow exponentially with time and the assumption is that the modes with the largest ω_i will dominate.

Figure 1 shows the vertical profile of $\bar{U}$ from Keffer and Niiler (1980). This profile, along with the Brunt-Vaisala profile (Fig. 2), can be combined to form the mean meridional potential vorticity gradient Q_y (Fig. 3). A bottom slope of $h_y = -2\text{x}10^{-3}$ was assumed and then Eqn. (2.19), along with boundary conditions (2.20), was then solved using the finite difference method for a variety of westward ($k < 0$, $l = 0$) waves and examined for complex eigenvalues. Due westward waves will be unaffected by any mean ($\bar{V}$) flow while waves with a north-south wavenumber component ($l \neq 0$) will be affected. However, as shown by Keffer and Niiler (1980), the north-south mean shears and velocities are generally much smaller than their east-west counterpart. Furthermore, as shown by FKNW, no north-south propagation was detected. Hence, it is assumed that

the dynamics will be dominated by westward travelling waves experiencing the westward mean shear and velocities.

The e-folding times shown in Figure 4 were found. Five different classes of instability are predicted, classed by where the maximum amplitude was found. Two of them (the "surface" and "bottom" trapped modes) would be difficult to detect because the instruments were placed too far from the top and bottom boundaries. They may also have limited physical significance; the surface-trapped mode because its entire structure is trapped above 50 m where the N^2 and $\bar{U}$ profiles are unreliable, the bottom profile because of the poor estimate of $\bar{U}$ (and hence, Q_y) below 2500 m due to the lack of reliable hydrographic stations.

The remaining three detectable classes all have velocity maxima somewhere in the thermocline and growth times greater than 200 days. The fastest growing (marked A in Fig. 4) which has a growth time of 216 days, a period of 104 days, and a wavenumber of 2.51×10^{-5} m^{-1} (scale of 40 km) is shown in Figure 5. Observed scales, however, were closer to 80 km. Also shown in Figure 5 is a "lower-thermocline" mode (marked B in Fig. 4) with a wavenumber of 1.26×10^{-5} m^{-1} (scale of 80 km), period of 300 days and a growth time of 500 days. Observed v velocity amplitudes and phases at the moorings (to be discussed in Section 4) are also shown.

POLYMODE Array III, Cluster C was deployed in May 1977 and recovered in April, 1978 in an area 400 km northwest of Barbados in the Atlantic North Equatorial Current. The area is characterized by a general westward mean flow of 2-5 cm s^{-1} and a mean northward temperature gradient of 5 x 10^{-3}°C km^{-1} in the mid-thermocline. At 4000 m there is a mean northward flow of 1 cm s^{-1} and a mean westward temperature gradient of 1.8 x 10^{-4}°C km^{-1}. Bottom topography is considered to be "moderately rough" in that an abyssal plain covers much of the cluster site but there are large peaks rising 1400 m above the plain. The bottom slope under the three southern moorings is approximately (2×10^{-3}, -2×10^{-3}), sloping upwards to the southwest. The foothills of the mid-Atlantic ridge generally lie 200 km to the northeast.

Figure 6 is a schematic of the array configuration. Complete T, u, v data records were available at 500 m and 4000 m, partial records at 180 m, 300 m, and 2500 m. Details of the mooring configuration, mean hydrography and first order statistics can be found in Koblinsky, Keffer and Niiler (1979). The analysis of horizontal divergence and vorticity was done using the southernmost three moorings whose nominal spacing was on the order of the Rossby radius (80 km).

Vertical coherence between adjacent instruments is generally very strong, especially in v velocity. Horizontal coherences were best at 500 m where they ranged from .65 to .95 in the low-frequency (80-320 days) based on 8 degrees of freedom (90% significance level = 0.7). They were the worst at 4000 m where they ranged from .45 to

.91. Westward propagation of north-south (v) velocity and temperature of 3.5 to 5.5 cm s^{-1} was observed at 500 m where the westward mean flow is 1 to 1.5 cm s^{-1}. There was no propagation of east-west (u) velocity (FKNW).

All data used in this study were low-pass filtered with a half-power point of 0.26 cpd and then subsampled daily to suppress the two-day inertial oscillations. The subsequent analysis was then done by dividing the frequency spectrum into four bands, chosen with the dispersion relation of barotropic and baroclinic Rossby-waves in mind. Normal flat-bottom baroclinic modes, calculated from the Brunt-Vaisala profile shown in Fig. 2 (Rhines, 1977), have a high frequency cut-off of 100 days. Hence, the "low-frequency" band (320-80 days) includes the first and second baroclinic modes. The "mid-frequency" band (64-30 days) includes the barotropic waves (cut-off of 20 days). The two "high-frequency" bands (30-10 days and 10-4 days) include the wind-forced motions described by Koblinsky (1980), and the dominant wind frequency (2-10 days). The bands are summarized in Table 1.

Because the estimation of horizontal temperature advection will require evaluating shear (u_z and v_z), two vertically separated instruments are required. Hence, it is the vertically averaged temperature between the two instruments that must be balanced. The available Cluster C data allowed nine different vertical instrument groupings representing three different depth bands as summarized in Table 2. "Upper-thermocline" included the 180, 250, and 300 m (nominal depths) instruments. Only temperature was recorded at the 250 m instruments.

"Mid-thermocline" included the 300 and 500 m instruments while "deep-water" included the 2500 and 4000 m instruments. Note that mooring 81, 309 m, is a short record (196d) and so the upper and mid-thermocline groups at that mooring are both shortened. Only velocity was recorded at mooring 82, 2538 m, allowing only advection to be estimated in the deep-water pair at that mooring. The mean flow in the thermocline at mooring 79 was seen to be substantially to the south (although the north-south shear was still small) and so rotated versions of the upper and mid-thermocline estimates (-32° and -56°, respectively) were calculated as well. These were designed such that the vertically averaged mean velocity was due zonal. At the other thermocline groups the mean flow was nearly due zonal.

Temperature rate of change

The local change of vertically averaged temperature (T'_t) was evaluated by first vertically averaging using the trapezoidal rule. E.g. average temperature for the mooring 81, 160-309 m group was calculated as $.24\ T_{160} + .50\ T_{233} + .26\ T_{309}$ for each day. Then the resulting data sequence was time differentiated using a time centered difference: $T'^{i}_{t} = (T^{i+1} - T^{i-1})/2\Delta t$ where the superscript is the time index and Δt is one day. The first and last points were evaluated using a backward and forward differencing, respectively, to preserve the series length.

Errors will occur due to the inability to measure temperature precisely ("measurement errors") and from finite difference approximations of continuous variations ("sampling error"). The temperature

measurements are accurate to within .01°C, most of which is due to bias. Because T_t involves relative temperature changes, the relative error of .001°C (Payne et al., 1976) is more appropriate. If two instruments are involved in the vertical average then this will cause a measurement error of $(.001°C)/2\Delta t = 0.6 \times 10^{-8}$°C s^{-1} where the measurements have been considered independent in space and time as far as the measurement error is concerned. Correlation of errors between different times is quite likely and would double this estimate. Mooring motion can also cause an observed temperature charge without any balancing dynamics. The rms excursion of the moorings was about 1-2 meters at 240 m (nominal depth of the "upper-thermocline" instruments), the maximum excursion was 10 m. These represent a temperature change of .05°C and .4°C, respectively. Over a 20 day time scale this is an average error of 3×10^{-8}°C s^{-1} and a maximum error of 23×10^{-8}°C s^{-1}. Hence, the total measurement error is at most 24×10^{-8}°C s^{-1}, and more often 4×10^{-8}°C s^{-1} at 240 m. Mooring motion is probably small at 2500 m and so the measurement error is of order 1×10^{-8}°C s^{-1}.

The sampling error in the upper and mid-thermocline groups are probably small because of the close vertical separation (200 m or less) compared to the scales of the lowest modes. The fastest growing shear mode has a vertical scale of approximately 300 m (see Section 2), the first baroclinic mode of about 1000 m. Comparison of the vertical integration of these modes with the finite difference version shows a 6% and 3% underestimate, respectively, for the upper-thermocline finite difference. The deep-water pairs have a larger separa-

tion (1500 m), although the scales are also larger. If the temperature mode is sinusoidal with the thermocline and the bottom as nodes, then the average is underestimated by 9%.

The total measurement and sampling error in T_t' will be of the order of

$$(\gamma^2 + \mathrm{Var}[\varepsilon]/\mathrm{Var}[T_t])^{1/2} \tag{3.1}$$

where γ is the sampling error, ε is the measurement error, and Var[ ] denotes variance. This is 9%, 10%, and 65% in the upper, mid-thermocline and deep water, respectively, where the average observed value of $(\mathrm{Var}[T_t])^{1/2}$ was 6.5×10^{-7}, 7.2×10^{-7}, and 1.7×10^{-8} °C s^{-1}, respectively. Hence we can expect the observed T_t' to be a good estimate of temperature change in the upper and mid-thermocline and a fair to poor estimate in the deep water.

Horizontal Temperature Advection

Total horizontal temperature advection is calculated as:

$$u_H \cdot \nabla T(t) = \frac{f\rho_o}{g\alpha}(-uv_z + vu_z)$$

$$\approx \frac{f\rho_o}{g\alpha}\left[-\left(\frac{u_1 + u_2}{2}\right)\left(\frac{v_1 - v_2}{\Delta z}\right) + \left(\frac{v_1 + v_2}{2}\right)\left(\frac{u_1 - u_2}{\Delta z}\right)\right. \tag{3.2}$$

where the subscript 1 (2) refers to the upper (lower) instrument, $f_o = 0.4 \times 10^{-4}$ s^{-1}, $\rho_o = 1.035$ gcm^{-3}, $g = 980$ cm s^{-2}, and all velocities are functions of time. The constant α was computed from hydrographic data taken during the 1978 recovery cruise. Generally, at any given time, the two terms $-uv_z$ and vu_z were very different in size and so small differences of large number were not being taken. Bryden (1976) rewrites (3.2) by expressing the velocity vector in

polar notation to get horizontal advection in terms of the depth turning of the velocity vector. While this allows an intuitive feel for what the turning of the vector means, it also brings in a 180° ambiguity in the differencing of the velocity vector.

The Reynolds decomposition of the temperature advection term was performed by first calculating the record mean of the vertically averaged and vertically differentiated velocities. These were then subtracted off. The six time dependent terms = $-\bar{U}v_z'$, $-u'\bar{V}_z$, $-u'v_z'$, $\bar{V}u_z'$, $v'\bar{U}_z$, and $v'u_z'$ were then calculated. These six terms along with the total horizontal advection and the local time change of temperature as evaluated at mooring 82, 338-538 m, are shown in Figures 7 and 8.

Horizontal advection will also be subject to measurement and sampling errors. The inability of the VACM to precisely measure velocity will cause a measurement error. Bryden (1976), using the IWEX data set, estimates the standard error of u and v due to measuring error to be .45 cm s^{-1}. While intercomparisons between VACMs in the Cluster C area are not available, the rms u and v velocities are similar to the IWEX area and so .45 cm s^{-1} is used here. Eqn. (3.2) involves eight products of the form (uv). The standard deviation of the measurement error due to velocity for the upper-thermocline pairs will be:

$$\frac{\sqrt{8}}{2\Delta z}\frac{f\rho_o}{g\alpha}\,\mathrm{Err}[uv] \simeq 1.4 \times 10^{-7}\,^{\circ}\mathrm{C}\ s^{-1}$$

where Δz = 100 m, $\alpha = 1.3 \times 10^{-4}$ gcm^{-3} °C^{-1}, and Err[uv] is the error in the product uv (with a 5 cm s^{-1} rms current and a .45 cm s^{-1} measurement error this will be approximately $\sqrt{2}(.45)(5)$ cm^2 s^{-2} =

3.2 $cm^2\ s^{-2}$). For the mid-thermocline pairs the measurement error is about 1.2×10^{-7}°C s^{-1}. The rms currents of the deep water pairs are smaller (about 2.5 cm s^{-1}) giving an error of 5×10^{-9}°C s^{-1}. These errors will probably be smaller for the high frequency bands due to the smaller velocities. From 28 CTD casts taken during the 1978 recovery cruise, α was found to vary 15%, 10%, and 30% in the upper, mid-thermocline and deep water, respectively. Variations in α in the deep water were probably due to inability to measure salinity precisely. Because relative changes of temperature are being observed, the exact value of α is less important than how much it varies, which is probably very little in the well mixed North Atlantic Deep Water found from 2500 m to 4000 m (Worthington, 1976). Based on rms values of 6.0×10^{-7}, 4.3×10^{-7}, 7.7×10^{-9}°C s^{-1} for $u_H \cdot \nabla T$ in the upper, mid-thermocline and deep water these correspond to a total measurement error of 1.5×10^{-7}, 1.3×10^{-3}, and 5.5×10^{-9}°C s^{-1}, respectively, or about 25%, 30%, and 71%, respectively, of the rms $u_H \cdot \nabla T$.

Estimation of the horizontal advection sampling error requires knowledge of the true vertical structure. Comparison of the upper and mid-thermocline finite difference estimates (3.2) with the fastest growing thermocline shear mode (Section 2) shows a 24% and 20% underestimate, respectively. Comparison with the first baroclinic mode shows 18% and 14% errors. The value of 20% is probably accurate for the thermocline. Comparison of the finite difference estimate of a cosine function with maximums at the thermocline (800 m) and bottom (5300 m) and node at 3050 m, with the true value, gives an underestimate of 10% and 5% for vertically averaged and differentiated velocity,

respectively, for a total error of 15% in each of the terms in (3.2). Hence, the total sampling error would be about 21% for the deep-water pairs.

The total measurement plus sampling error in $u_H \cdot \nabla T$ will be of the order of 32%, 36%, and 74% for the upper-thermocline, mid-thermocline, and deep-water instruments. Thus, the observed horizontal temperature advection will be a fair estimate in the upper and mid-thermocline, and a poor estimate in the deep-water.

Temperature Balance

A necessary condition for two terms to balance is that the residual must not be significantly greater than our ability to estimate it. Suppose we wish to test the balance

$$x + y = 0$$

and have estimates x_e, y_e with measurement errors, ε_x, ε_y and sampling errors γ_x, γ_y of the form:

$$x_e = x + \gamma_x x + \varepsilon_x$$

$$y_e = y + \gamma_y y + \varepsilon_y$$

where x and y are the true values. Note that:

$$E[x_e] = (1 + \gamma_x)\, E[x]$$

$$\mathrm{Var}[x_e - x] = \mathrm{Var}[\gamma_x x + \varepsilon_x]$$

$$\approx \gamma_x^2\, \mathrm{Var}[x] + \mathrm{Var}[\varepsilon_x]$$

where E[ ] denotes expected value and Var[ ] denotes variance. We have assumed that the measurement error is uncorrelated with the true value of x and that its expected value is zero. Similar equations

can be written for y. Then the variance of the error of the sum x_e + y_e can be written as:

$$\mathrm{Var}[(x_e + y_e) - (x + y)] = \gamma_x^2\,\mathrm{Var}[x] + \gamma_y^2\,\mathrm{Var}[y] + 2\gamma_x\gamma_y\,\mathrm{Cov}[x,y] + \mathrm{Var}[\varepsilon_x] + \mathrm{Var}[\varepsilon_y]$$

If y does in fact equal -x then the variance of the error will be:

$$\mathrm{Var}[(x_e + y_e) - (x + y)] = \mathrm{Var}[(x_e + y_e)] = (\gamma_x - \gamma_y)^2\,\mathrm{Var}[x] + \mathrm{Var}[\varepsilon_x] + \mathrm{Var}[\varepsilon_y] \qquad (3.3)$$

Thus, if the variance of our measured residual (= x_e + y_e) significantly exceeds this amount then we must reject the hypothesis that x + y = 0, i.e. that they balance.

Table 3 shows the observed rms values of T_t' and $u_H \cdot \nabla T$ in the two lowest frequency bands as well as the observed residual and estimated error in the residual. Because the true value of $\mathrm{Var}[T_t']$ or $\mathrm{Var}[u_H \cdot \nabla T]$ is not known, their average was used. In the upper thermocline (180-300 m), in either frequency band, it is unlikely that T_t' and $u_H \cdot \nabla T$ balance because the residual is significantly greater than the estimated errors. Here the residual will be a good estimate of vertical velocity:

$$w' = -(T_t' + u_H \cdot \nabla T)/\bar{\theta}_z \qquad (3.4)$$

At all other depths and moorings, the residual is smaller or of the same size as the expected error in the two low-frequency bands. In the two high-frequency bands horizontal advection is an order of magnitude smaller than temperature change. Here T_t' will be a good estimate of vertical velocity:

$$w' = -T_t'/\bar{\theta}_z \qquad (3.5)$$

While the condition that the residual be small compared to the error is a necessary condition for balancing, it can always be met with a sufficiently inaccurate instrument. Our faith that two terms balance is increased if they are significantly coherent, 180° out of phase, and have magnitudes that are not significantly different. Table 4 shows estimated coherence squared, phases, and ratios of rms amplitude between the time rate of change of temperature and horizontal advection. In the mid-thermocline, at mid-frequencies, the two are highly coherent, 180° out of phase and of nearly equal magnitude at 3 out of 4 of the moorings. The fourth mooring (81) has the correct phase and amplitude but low coherence. It was also a short record.

Figure 7b shows the low-passed signal (cut-off of 30 days) of T_t' and $-u_H \cdot \nabla T$ as well as the residual at mooring 82, 338-538 m (mid-thermocline). The correspondence is quite evident although there is a phase shift in the last half of the record. Figure 7a shows the complementary high frequency signal. Horizontal advection is considerably smaller than the temperature changes.

Also shown in Table 4 is the coherence squared and phase between T_t' and the Reynolds' decomposed components of $u_H \cdot \nabla T$. There is high coherence between T_t' and $\bar{U}T_x'$ in the upper thermocline in both frequency bands and in the mid-thermocline in the mid-frequency band. They are 180° out of phase.

Figure 8 shows low-passed time series of all the components of $u_H \cdot \nabla T$ at mooring 82, 338-538 m. Because $\bar{V}$ and $\overline{T_x}$ are small the components $\bar{V}T_y'$ and $u'\overline{T_x}$ are small. The coherence between T_t' and

$-\bar{U}T_x'$ is evident although the amplitudes are different by about a factor of 2.

Divergence

Divergence and vorticity estimates require at least three moorings to evaluate. The velocity coherences between the northernmost mooring (79) and the three southern moorings are low, between 0.05 and 0.51 in the low-frequency band at 500 m, due to the large separation distances (from 150 km to 210 km). The coherences among the three southern moorings was much better, between 0.64 and 0.92 at 500 m, and so they were used to estimate the required velocity derivatives. They form an asymmetrical triangle (Fig. 6).

At a given depth (300, 500, and 4000 m were done) we wish to fit the equation

$$u_x(t)\ \Delta x_i + u_y(t)\ \Delta y_i + u_o(t) = u_i(t) \qquad (3.6)$$

at each of the three moorings where $(\Delta x_i, \Delta y_i)$ is the horizontal position vector of a mooring, relative to the triangle's center of mass, $u_i(t)$ is the observed velocity, $(u_x(t), u_y(t))$ is the velocity gradient, and $u_o(t)$ is the velocity at the center of mass (the average velocity).

This will provide three equations in the three unknowns $u_x(t)$, $u_y(t)$, $u_o(t)$. A similar set of three equations can be found for v velocity. The solution procedure is given in Appendix A.

Fig. 9 shows the estimates of u_x and v_y at 500 m. Although their coherence is not significant (see Table 5) their sum, $u_x + v_y$, is still less than the estimated error. Appendix A considers the

response of the array to a horizontally non-divergent plane wave of the form

$$\psi = \mathrm{Re}\ \{A(z)e^{i(kx + ly - \omega t)}\} \tag{3.7}$$

where A(z) is the vertical structure, (k,l) is the horizontal wavenumber, ω is frequency, and the associated velocities would be given by $(u,v) = (-\psi_y, \psi_x)$. In general, a non-zero value of $u_x + v_y$ would be detected due to the measurement and sampling errors inherent in the array design. The measurement error is estimated to be 1.75×10^{-7} s^{-1} in the low frequency, due to the inaccuracies of the VACM. The sampling error will depend on the horizontal wavenumber and the amplitude of the wave. Fig. 10a shows the rms value of $u_x + v_y$ that would be detected for a wave of form (3.7) with rms currents of 5 cm s^{-1}, as a function of (k,l), and assuming perfect coherence across the array. Because the true value of $u_x + v_y$ is zero, the values in Fig. 10a are also the rms sampling error. Details are given in Appendix A.

The errors shown are as large as the actual values that were observed in the ocean for wavenumbers greater than .01 km^{-1} (wavelength less than 630 km). Fig. 10b shows the sampling error if the coherence between all u,v pairs drops to 0.8. The sampling error is at least as large as the observed $u_x + v_y$ for all wavenumbers. Hence, although the observed u_x does not resemble the observed v_y we must conclude that their sum, $u_x + v_y$, is still indistinguishable from horizontal non-divergence.

The large sampling error arises because the "response" of the array to an arriving wave is different for u_x than for v_y, due to the

asymmetry of the triangle legs. The wave may cause an observed u_x without the compensating v_y ever being seen. The signals for u_x and v_y shown in Fig. 9 are probably due to waves coming from completely different directions. The array acts as a highly directional "antenna."

Vorticity

Vorticity is estimated in a manner similar to divergence except that the difference, $v_x - u_y$, is formed. Fig. 11 shows the estimates of v_x and $-u_y$ at 500 m as well as estimated vorticity. The measurement and sampling errors can be treated similarly to the divergence errors. However, because the vorticity of a plane wave given by (3.7) is not zero (except for $k = l = 0$), the response of the array can be normalized by the true vorticity to give an amplitude "gain" as a function of horizontal wavenumber. Details are given in Appendix A. This is shown in Fig. 12, where the coherence has been assumed to be unity across the array. The array again acts as a highly directional vorticity detector. Waves arriving from the northeast or southwest are faithfully received while waves from the southeast or northwest are nearly totally suppressed.

Planetary Advection

The meridional velocities at the three southern moorings were averaged together for each day and then multiplied by β to obtain estimates of the advection of planetary advection (βv). The mean of this result was then removed (to eliminate time trends) and the

remainder time integrated using the trapezoidal rule to allow comparison with $v_x - u_y$. Estimation of the error is discussed in Appendix B.

The vorticity $(v_x - u_y)$ and time integrated advection of planetary vorticity at all three depths, are plotted in Fig. 13, along with their difference. Table 6 gives rms estimates of their amplitudes and relative coherence and phase in the four frequency bands. In the low-frequency band they are significantly coherent at all depths, approximately 180° out of phase and have similar amplitudes. Their sum is smaller than the rms error. They are significantly coherent in band 3 in the upper-thermocline and in bands 2, 3, and 4 in the deep-water. However, their amplitudes are very different.

Stretching

It was found that the local temperature change provides good estimates of vertical velocity in the two high frequency bands at all depths. The sum of local temperature change and horizontal advection was found to provide good estimates in the two low-frequency bands in the upper-thermocline, at moorings 81 and 82. At other locations, for the two low-frequency bands, w is of the same order or smaller than the estimated errors. It may or may not be dynamically important.

Here we test the vorticity balance

$$\zeta + \int_0^t \beta v dt = \frac{f}{(z_1 - z_2)} \int_0^t [w(z = z_1) - w(z = z_2)]dt \qquad (3.8)$$

where the subscript 1 refers to z at a near surface location and the subscript 2 to a deeper location, relative to the depth where the

left-hand side is being evaluated. The assumption is that $\zeta + \int \beta v dt$ is fairly constant from z_1 to z_2 and so the estimate is representative of the vertical average.

The results of the comparison (3.8) are summarized in Table 7. Five different estimates of vertical velocity were used for the right-hand side. Three of them were from the temperature balance

$$w = -(T_t' + u_H \cdot \nabla T)/\bar{\theta}_z \tag{3.9}$$

in the two low-frequency bands, and the balance

$$w = -T_t'/\bar{\theta}_z \tag{3.10}$$

in the two high-frequency bands. The estimated w at each of the southern moorings were averaged together to give horizontally-averaged estimates of vertical velocity in the upper-thermocline (nominal depth 240 m), mid-thermocline (400 m), and deep-water (3250 m). The estimate w_{240} is the average of only two estimates because there was no instrument at mooring 80, 180 m. The horizontal averaging procedure probably tends to select the larger scales because phase changes from small scales would tend to cancel out their contribution.

The other two vertical velocity estimates were at the surface and bottom. The surface velocity was simply set to zero (accurate time series of Ekman pumping are hard to come by). The bottom vertical velocity was either set to zero or was estimated as

$$w_{bot} = u_{4000}\, h_x + v_{4000}\, h_y \tag{3.11}$$

where (u_{4000}, v_{4000}) is the horizontally averaged 4000 m velocity and (h_x, h_y) is the average bottom slope, taken to be $(2 \times 10^{-3}, -2 \times 10^{-3})$. The assumption here is that the 4000 m velocity is representative of the bottom velocity (z = 5300 m).

Coherence squared and amplitudes were calculated between the two sides of (3.8) and are summarized in Table 7. A high coherence and a phase near zero indicates that the two terms balance to the extent that their amplitudes let them. The amplitude of the right-hand side is somewhat arbitrary for some comparisons in that a depth was arbitrarily picked where vertical velocity goes to zero. These amplitudes are marked with an X.

Heat equation

It was indicated in Section 2 that the ratio of the rms amplitude of T_t' and $\overline{U}T_x'$ should be related to their proximity to the critical layer. Cross-correlation analysis from FKNW showed westward propagation of 3.5 to 5.5 cm s^{-1} at 500 m where the mean flow is estimated to be 1 to 1.5 xm s^{-1}. The wave speed is probably on the order of 2.5 cm s^{-1}. From Keffer and Niiler (1980) westward mean flow at this speed is found at 250 m. A least squares fit to the observed mean flow versus depth would put it at 400 m (See Figure 1). The observed ratios of T_t' to $\overline{U}T_x'$ are shown in Table 8. In the low-frequency band the ratio appears to approach one in the upper-thermocline at 200-300 m at moorings 79 and 82. Mooring 80 was missing velocity at 180 m while 81 is a short record. At all of the moorings the terms are coherent and 180° out of phase in the upper-thermocline while only one is coherent in the mid-thermocline (79). It would appear that a critical layer is located somewhere around 200-300 m in the low-frequency.

FKNW also reported a local eddy potential energy maximum at 300 m. Large vertical phase changes are associated with critical layers (see Pedlosky, 1979, p. 467 and Fig. 5b, 250 m). Because T' is proportional to ψ_z, this PE' maximum may be a feature of the critical layer. Because PE' profiles can be calculated from hydrographic or XBT data alone, this invites examining other mid-ocean currents for such a maximum.

In Section 2 the phase relation between T_t' and $v'\overline{T_y}$ was predicted by the linear model to be:

$$\arg[T_t'] - \arg[v'\overline{T_y}] = \arg[\frac{f\rho_o}{g\alpha} \frac{\omega_r A_z}{kAT_y} (1 - \eta i)] \qquad (4.1)$$

In the upper-thermocline, in the mid-frequency band, the phase between these two terms is fairly stable, although the coherence is marginally significant. It averages around -30°. If $A_z > 0$, this would set η = .58; for $A_z < 0$ then η = -.58. The phase between $\bar{U}T_x'$ and $v'\overline{T_y}$ is given by:

$$\arg[\overline{U}T_x'] - \arg[v'\overline{T_y}] = \arg[\frac{\overline{U}A_z}{\overline{T_y}}(1 - \eta i)]. \qquad (4.2)$$

Because the coefficient in front of $(1 - \eta i)$ is opposite in sign to the one in (4.1), we expect a phase of 150° or -150° for $A_z > 0$, $A_z < 0$, respectively. The actual phases were 154°, 141°, -130°, 157° for coherence squared of .40, .49, .88, and .80 at moorings 79, 79 rotated, 81, and 82. Elsewhere, the coherences generally are not significant.

The coherence begween T_t' and $\overline{U}T_x'$ is generally much higher than that between T_t' and $v'\overline{T_y}$. This may be because the phase of the former is dependent only on the ratio ω_i/ω_r, generally quite small, while the latter depends on $A\phi_z/A_z$, which is highly mode dependent. Non-constant phases tend to degrade coherences.

The fact that so much of the temperature variance can be explained by horizontal advection (up to 100%) invites caution when interpreting eddy potential energy as vertical fluctuations of isotherms. In the Cluster C area the isotherms generally slope downwards to the north ($\overline{T_y} > 0$). While this represents available potential energy, any north-south movement of these mean isotherms ($v'\overline{T_y}$) or western advection of deformed isotherms ($\overline{U}T_x'$), becomes "eddy" potential energy simply because the energy varies spatially and temporally.

Vorticity

Time integrated advection of planetary vorticity was found to be

highly coherent and of similar magnitude to vorticity in the low-frequency band (see left column, Table 6) and within the errors of the analysis could be said to "balance." However, as indicated in Section 3, we may be seeing only a fraction of the vorticity due to the geometry of the moorings. Indications that this is true is seen by the (marginal) coherence of stretching with the residual (Table 7, lines 1,2,4). Because the two vertical velocity estimates that comprise low-frequency w_{240} (moorings 81, 82, upper-thermocline) were found to be significantly greater than their estimated errors, estimates made with w_{240} are probably meaningful. Even the w_{400} estimates are marginally larger than their estimated errors and are coherent with the residual.

In the mid-frequency the terms ζ and $\int \beta v dt$ were not coherent except at 4000 m where they were significantly different in size. Furthermore, although the estimates of vertical velocity are also meaningful in this band, they are marginally coherent with the residual and of the wrong phase. The residual must include large contributions from advection of vorticity. Just how much would depend on how much of the vorticity we are seeing. If one half, then at 300 m this would increase the residual $\zeta + \int \beta v dt$ to half again as much and make it the same size as the stretching ($\sim 4.3 \times 10^{-7}\ s^{-1}$). Advection would be of the same size and represent one half of the energy. It is important to note, however, that this advection need not be nonlinear. Terms like $\bar{U}\zeta_x$ could dominate the first order dynamics.

The high-frequency picture appears to be simpler. Scale analysis would predict that for time scales shorter than $\tau = L/U = 20$ days,

horizontal advection will be smaller than T_t'. In the two high-frequency bands (4.3d > τ > .64d) horizontal advection was found to be an order of magnitude smaller. Local change of temperature is assumed to be a good estimator of vertical velocity within the limits of its errors at all depths. The scales shown in Eqn. (2.17) predict planetary advection to be less important at time scales less than $\tau = L^{-1} \beta^{-1}$ = 7 days and horizontal advection at scales less than L/U (20 days). Thus, vorticity changes should be balanced by stretching. This is indicated in Table 7. However, w_{400} is 180° out of phase with 300 m vorticity. These two bands are where Koblinsky (1980) found rotary coherence between velocity and wind estimates from the Windward Islands. If vertical velocity forced by the Ekman pumping decayed with depth, then w estimated above vorticity would be correlated (lines 1,4,5) while w below would be anti-correlated (line 2). This seems to be the pattern with both 300 m and 500 m vorticity although the coherences are only marginally significant at the latter depth. At 4000 m there is evidence of stretching both from above (line 7) and below (line 8).

The conclusion is that the sum

$$\zeta + \int \beta v dt - \int f w_z dt \tag{4.3}$$

is less than the errors everywhere except in the mid-frequency band. This does not mean that horizontal advection is unimportant elsewhere (particularly in the low-frequency band) because errors in w and ζ are large.

Modal Description and Stability

The shear modes calculated in section 2 describe the vertical structure and phase of growing and decaying modes. It would be useful to compare the observed structure and phases with the shear modes shown in Figure 5. The period of both modes are in the low-frequency band (105 and 300 days for modes A and B, respectively). The relative v velocity amplitudes in the low-frequency band are also plotted on Figure 5a, scaled such that their 500 m amplitudes all match the mode A amplitude at 500 m. Any of the mooring or mode relative amplitudes can be multiplied by an arbitrary constant. Phases were also calculated by first arbitrarily setting the 500 m phase equal to the mode A phase at 500 m, and then "chaining" outwards. That is, the 300 m phase is relative to the 500 m phase, the 180 m phase is relative to the 300 m phase. Any of the mooring or mode phases can be shifted by an arbitrary constant.

On the basis of the amplitudes one might say that mooring 81 is following mode B while the other moorings are following mode A. The phases are inconclusive. The phase increases with depth at all four moorings which is consistent with either a growing mode A or a decaying mode B, although they match mode A more closely. However, none of the observed phase changes are significantly different from zero.

Only two moorings had significant north-south eddy heat fluxes, one of them down-gradient (82), the other up-gradient (81). For a 2 cm s^{-1} rms current at 500 m, modes A and B predict heat fluxes

of .15 and .95 ^{o}C cm s^{-1}, respectively. A rough idea of the minimum flux that can be detected can be made by considering the estimated flux of two signals whose true correlation is zero:

$$T = T_o \cos\omega t + \overline{T}$$
$$V = V_o \sin\omega t + \overline{V} \qquad (4.4)$$

In general, the true means ($\overline{T}$ and $\overline{V}$) are not known, only estimates ($\overline{T}_e$, $\overline{V}_e$) subject to bias (α_T, α_V) caused by the finite observation period. In addition, there will be measurement errors (ε_T, ε_V) due to instrumental inaccuracies and mooring motion. Hence, the calculated covariance will be:

$$\overline{(T-T_e)(V-V_e)} = \overline{\varepsilon_T V_o \sin\omega t} + \overline{\varepsilon_V T_o \cos\omega t} + \overline{\varepsilon_T \varepsilon_V} + \alpha_T \alpha_V \qquad (4.5)$$

The expected value of the right-hand side is zero but, in general, it will not be. Calculation of the standard deviation about zero requires knowledge of the correlation between ε_T and $V_o \sin\omega t$ etc.[1].

---

[1] It would be interesting, however, to speculate on the effect of velocity perturbations forcing the mooring downwards into colder waters. If the mooring's nominal position is straight up this would not cause a mean u'T', because positive or negative u' will cause a negative T'. However, in the presence of a mean flow the mooring will be leaning over; perturbations in the direction of the mean flow would decrease temperature and vice versa. A mean u'T'

The smallest (4.5) could be is $\alpha_T\alpha_V$, the largest $\frac{1}{2}\varepsilon_T V_o + \frac{1}{2}\varepsilon_V T_o + \varepsilon_T\varepsilon_V + \alpha_T\alpha_V$. For six degrees of freedom and Var{T} = 0.25 $^oC^2$, Var{V} = 4.0 $cm^2 s^{-2}$ (approximate low-frequency averages at 500 m), then $\alpha_T = .20^oC$, $\alpha_V = .8$ cm s^{-1}, $V_o = 2\sqrt{2}$ cm s^{-1}, $T_o = .5\sqrt{2}$ ^oC. From section 2, $\varepsilon_T = .05^oC$, $\varepsilon_V = .45$ cm s^{-1}. Hence, the standard deviation of the estimated covariance will be somewhere between .16 and .41 ^oC cm s^{-1}. If the true heat flux is something other than zero it probably could not be detected unless it exceeded this threshold. Clearly, heat fluxes from mode B would be difficult to detect; those from mode A should be fairly easy. While these modes are not intended to be definitive, they probably are representative of the sort of heat fluxes that would be produced by linear amplification. Hence, one is forced to either invoke finite amplitude dynamics or an explanation of why the larger, slower growing waves are selected. Either way, it is clear non-linear dynamics are at work.

Ubiquitous in the Cluster C data set is an eddy heat flux vector more nearly directed <u>across</u> the mean temperature gradient.

---

would be measured. At Cluster C, the rms excursion was only 1-2 meters or a temperature change of .05 ^oC, much less than the observed temperature changes. Furthermore, temperature and pressure were not significantly correlated. However, this could be a problem with less rigid moorings in the presence of a strong mean flow.

The linear model predicts a mean $\overline{u'T'}$ in the presence of a non-zero north-south wavenumber:

$$\overline{u'T'} = -\tfrac{1}{2}lA^2 \frac{f\rho_o}{g\alpha} \phi_z \qquad (4.6)$$

and indeed, these fluxes are of the order of $1^{\circ}C$ cm s^{-1} or more. Moreover, they are located at 300 to 500 m, where the phase shown in Figure 5 varies most rapidly. However, because they are across gradient they do not transfer energy and hence may not be as involved in finite amplitude dynamics.

FKNW hypothesize a "mean" field varying on a secular scale that occasionally provides the necessary horizontal density gradients and vertical shears necessary for instability. Indeed, the observations at mooring 82 seem to fit the linear model fairly well. However, the above analysis would suggest turning this hypothesis around. The mean state, as determined from historical data, is quite capable of supporting detectable, amplifying modes. An explanation is needed as to what is preventing these modes from transferring energy into the eddy fields.

Appendix A

Divergence and Vorticity Estimates and Errors

We wish to solve the system:

$$\begin{pmatrix} \Delta x_1 & \Delta y_1 & 1 \\ \Delta x_2 & \Delta y_2 & 1 \\ \Delta x_3 & \Delta y_3 & 1 \end{pmatrix} \begin{pmatrix} u_x(t) \\ u_y(t) \\ u_o(t) \end{pmatrix} = \begin{pmatrix} u_1(t) \\ u_2(t) \\ u_3(t) \end{pmatrix} \qquad \text{(A.1a)}$$

$$\begin{pmatrix} \Delta x_1 & \Delta y_1 & 1 \\ \Delta x_2 & \Delta y_2 & 1 \\ \Delta x_3 & \Delta y_3 & 1 \end{pmatrix} \begin{pmatrix} v_x(t) \\ v_y(t) \\ v_o(t) \end{pmatrix} = \begin{pmatrix} v_1(t) \\ v_2(t) \\ v_3(t) \end{pmatrix} \qquad \text{(A.1b)}$$

where $(\Delta x_i, \Delta y_i)$ are the mooring locations relative to the mean mooring location and (u_o, v_o) is the velocity at the mean location. For moorings 80, 81, 82:

$$\underset{\sim}{A} = \begin{pmatrix} \Delta x_{80} & \Delta y_{80} & 1 \\ \Delta x_{81} & \Delta y_{81} & 1 \\ \Delta x_{82} & \Delta y_{82} & 1 \end{pmatrix} = \begin{pmatrix} -1.50\text{x}10^6\text{cm} & 2.05\text{x}10^6\text{cm} & 1 \\ 6.17\text{x}10^6\text{cm} & -.16\text{x}10^6\text{cm} & 1 \\ -4.67\text{x}10^6\text{cm} & -1.90\text{x}10^6\text{cm} & 1 \end{pmatrix} \qquad \text{(A.2)}$$

The inverse of $\underset{\sim}{A}$ allows simple multiplication with the column matrix of u_i (or v_i) to find u_x, u_y (v_x, v_y):

$$\underset{\sim}{A}^{-1} = \begin{pmatrix} \hat{a}_{11} & \hat{a}_{12} & \hat{a}_{13} \\ \hat{a}_{21} & \hat{a}_{22} & \hat{a}_{23} \\ \hat{a}_{31} & \hat{a}_{32} & \hat{a}_{33} \end{pmatrix} \qquad \text{(A.3)}$$

$$= \begin{pmatrix} -4.68\text{x}10^{-8}\,\text{cm}^{-1} & 1.06\text{x}10^{-7}\,\text{cm}^{-1} & -5.91\text{x}10^{-8}\,\text{cm}^{-1} \\ 2.91\text{x}10^{-7}\,\text{cm}^{-1} & -8.50\text{x}10^{-8}\,\text{cm}^{-1} & -2.06\text{x}10^{-7}\,\text{cm}^{-1} \\ .333 & .333 & .333 \end{pmatrix} \qquad \text{(A.4)}$$

and so,

$$\underset{\sim}{A}^{-1} \begin{pmatrix} u_1(t) \\ u_2(t) \\ u_3(t) \end{pmatrix} = \begin{pmatrix} u_x(t) \\ u_y(t) \\ u_o(t) \end{pmatrix} \qquad \text{(A.5)}$$

$$\underset{\sim}{A}^{-1} \begin{pmatrix} v_1(t) \\ v_2(t) \\ v_3(t) \end{pmatrix} = \begin{pmatrix} v_x(t) \\ v_y(t) \\ v_o(t) \end{pmatrix} \qquad \text{(A.6)}$$

Hence, to find divergence:

$$u_x(t) + v_y(t) = \sum_{j=1}^{3} \hat{a}_{1j}\, u_j(t) + \sum_{j=1}^{3} \hat{a}_{2j}\, v_j(t) \qquad \text{(A.7)}$$

Because horizontal non-divergence (to first order) for low frequency motions is so well grounded theoretically, we would expect any deviation of $u_x + v_y$ from zero to be due to errors. The inability

cause a "measurement" error. The lack of horizontal coherency and the aliasing due to insufficient horizontal resolution will cause a "sampling" error.

Assuming a .45 cm s^{-1} measurement error in velocity, (A.7) gives a measurement error in $u_x + v_y$ of

$$(\sum_{j=1}^{3} \hat{a}_{1j}^2 + \sum_{j=1}^{3} \hat{a}_{2j}^2)^{\frac{1}{2}} (.45 \text{ cm s}^{-1}) = 1.75\text{x}10^{-7}\text{s}^{-1}$$

where the (u_j, v_j) are assumed to be independent. This will also be the measurement error in vorticity ($=v_x - u_y$).

The sampling error is more difficult to assess and generally requires some knowledge of the horizontal wavenumber and coherency scales. Here, we calculate the autospectrum of the sampling error by making assumptions about the nature of the velocity field and by assuming our ability to measure u and v is precise. To simplify the notation let:

$$b_j = a_{1j} \quad j=1,3$$

$$b_{j+3} = a_{2j} \quad j=1,3$$

$$\xi_j(t) = u_j(t) \quad j=1,3$$

$$\xi_{j+3}(t) = v_j(t) \quad j=1,3$$

Then the measured horizontal divergence is simply:

$$u_x(t) + v_y(t) = \sum_{j=1}^{6} \hat{b}_j \, \xi_j(t) \qquad \text{(A.8)}$$

and will consist of error plus real divergence. The Fourier transform will be

$$(u_x + v_y) = \sum_{j=1}^{3} \hat{b}_j \tilde{\xi}_j(f) \qquad \text{(A.9)}$$

where $\tilde{\xi}_j$ is the transform of ξ_j.

Hence the auto-spectrum of the estimated $u_x + v_y$ will be

$$\mathcal{E} = \left(\sum_{j=1}^{6} \hat{b}_j \tilde{\xi}_j^* \right) \left(\sum_{k=1}^{6} \hat{b}_k \tilde{\xi}_k \right)$$

$$= \sum_j \sum_k \hat{b}_j \hat{b}_k \tilde{\xi}_j^* \tilde{\xi}_k$$

$$= \sum_j \sum_k \hat{b}_j \hat{b}_k \gamma_{jk} e^{i\phi_{jk}} \sqrt{C_{jj} C_{kk}} \qquad \text{(A.10)}$$

where γ_{jk} is the coherency between ξ_j and ξ_k

ϕ_{jk} is the associated phase

C_{jj} is the autospectrum of ξ_j

Using the antisymmetry of phase and assuming that the velocity field is horizontally isotropic and homogeneous ($C_{ii} = C_{jj} = C$) then this can be written:

$$\mathcal{E} = C \left\{ \sum_{j=1}^{6} \hat{b}_j^2 + 2 \sum_{j=1}^{5} \sum_{k=j+1}^{6} \hat{b}_j \hat{b}_k \gamma_{jk} \cos \phi_{jk} \right\} \qquad \text{(A.11)}$$

Equation (A.11) requires no assumptions about whether the velocity field is horizontally divergent. However, it requires knowledge of the theoretical coherence, phase, and velocity autospectrum. If the velocity field is due entirely to horizontally

non-divergent plane waves of the form:

$$(u,v) = i\ (-l,k)\ F(z)\ e^{i(kx + ly - \omega t)} \qquad (A.12)$$

then (A.11) will be the autospectrum of the sampling error. In this case

$$\phi_{jk} = k(x_k - x_j) + l(y_k - y_j) + \alpha_k - \alpha_j \qquad (A.13)$$

where $\alpha_j = -\pi/2$ for j=1,3 (u velocity)

$\pi/2$ for j=4,6 (v velocity)

Figure 10a shows the rms sampling error within some frequency band where the rms current speed is 5cm s^{-1} (that is C = 25 $cm^2 s^{-2}$/BW and $\sqrt{\epsilon BW}$ is plotted where BW is the bandwidth), as a function of horizontal wavenumber. A coherence of unity for all j,k pairs has been assumed (observed coherences ranged from .64 to .92 at 500 m). Figure 10b is identical except the coherence has been set to 0.8 .

Vorticity

The vorticity sampling error is treated similarly. The estimate of vorticity will be given by:

$$v_x(t) - u_y(t) = -\sum_{j=1}^{3} \hat{a}_{2j}\, u_j(t) + \sum_{j=1}^{3} \hat{a}_{1j}\, v_j(t) \qquad (A.14)$$

and all of the calculations will carry through if we define:

$$\hat{d}_j = -\hat{b}_{j+3} = -\hat{a}_{2j} \qquad j=1,3$$
$$\hat{d}_j = \hat{b}_{j-3} = \hat{a}_{1j} \qquad j=4,6 \tag{A.15}$$

such that

$$v_x(t) - u_y(t) = \sum_{j=1}^{6} \hat{d}_j \, \xi_j(t) \tag{A.16}$$

and continue with Eqn. (A.8). The result will be

$$Z = C \left\{ \sum_{j=1}^{6} \hat{d}_j^2 + 2 \sum_{j=1}^{5} \sum_{k=j+1}^{6} \hat{d}_j \hat{d}_k \gamma_{jk} \cos\phi_{jk} \right\} \tag{A.17}$$

However, because the vorticity of the plane wave described by (A.12) is not zero, (A.17) can be normalized by the true vorticity power spectrum to give

$$Z' = \frac{\sum_{j=1}^{6} \hat{d}_j^2 + 2 \sum_{j=1}^{5} \sum_{k=j+1}^{6} \hat{b}_j \hat{b}_k \gamma_{jk} \cos\phi_{jk}}{(k^2 + \ell^2)} \tag{A.18}$$

This is plotted in Figure 12 for a coherence of unity. The point (0,0) is a singularity.

Time integrated advection of planetary advection was calculated by horizontally averaging v velocity and then integrating using the trapezoidal rule:

$$P_m = \beta\Delta t \sum_{i=1}^{m} \lambda_i \langle v \rangle_i \qquad (B.1)$$

where P_m is the estimate at time $t = m\Delta t$, $\lambda_i = \frac{1}{2}$ for i=1,m and $\lambda_i = 1$ otherwise, $\langle v \rangle_i$ is the horizontal average of v velocity at time i. The measurement error in each $\langle v \rangle_i$ will be $.45/\sqrt{3}$ cm s^{-1} = .26 cm s^{-1} if the measurement errors are independent in space. The measurement error in the sum (B.1) is

$$Err[P_m] = \beta\Delta t \left[\sum_{i=1}^{m} \lambda_i^2 \, Err[\langle v \rangle_i]^2 \right]^{\frac{1}{2}}$$

$$= \beta\Delta t k Err[\langle v \rangle] \qquad (B.2)$$

or $5x10^{-9}s^{-1}$ at the beginning of the series and $7.5x10^{-7}$ at the middle. Because the integrand was demeaned before integrating, the series is constrained to end at zero where the error will again be $5x10^{-9}s^{-1}$.

References

Bryden, H.L., (1976), Horizontal advection of temperature for low-frequency motions. Deep-Sea Research, 23, 1165-1174.

Bryden, H.L. and N.P. Fofonoff, (1977), Horizontal divergence and vorticity estimates from velocity and temperature measurements in the MODE region. J. of Phys. Oc., 7, 329-337.

Fu, L., T. Keffer, P.P. Niiler and C. Wunsch, (1980), Low-frequency motions observed in POLYMODE Array III: The Mid-Atlantic Ridge and the Atlantic North Equatorial Current. In preparation.

Gill, A.E., J.S.A. Green and A.J. Simmons, (1974), Energy partition in the large-scale ocean circulation and the production of mid-ocean eddies. Deep-Sea Research, 21, 499-528.

Keffer, T. and P.P. Niiler, (1980), The vertical structure of observed and geostrophically derived mean flow, heat and salt eddy convergences in the sub-tropical North Atlantic. In preparation.

Koblinsky, C.J., (1980), Wind forced response of the Atlantic North Equatorial Current. In preparation.

Koblinsky, C.J., T. Keffer and P.P. Niiler, (1979), A Compilation of Observations in the Atlantic North Equatorial Current. Oregon State University, School of Oceanography technical report. Reference 79-12.

Kundu, P.K., J.S. Allen and R.L. Smith, (1975), Modal decomposition of the velocity field near the Oregon coast. J. of Phys. Oc., 5, 683-704.

McWilliams, J.C., and G.R. Flierl, (1976), Optimal, quasi-geostrophic wave analysis of the MODE array data. Deep-Sea Research, 23, 285-300.

McWilliams, J.C. and A.R. Robinson, (1974), A wave analysis of the Polygon array in the tropical Atlantic. Deep-Sea Research, 21, 359-368.

Payne, R.E., A.L. Bradshaw, J.P. Dean and K.E. Schleicher, (1976), Accuracy of Temperature Measurements with the VACM. W.H.O.I. Ref. 76-94. (Technical report)

Pedlosky, J., (1979), Geophysical Fluid Dynamics. Springer - Verlag, NY. 624pp.

Rhines, P.B., (1977), The dynamics of unsteady currents. In The Sea, Vol. 6. Goldberg, McCave, O'Brien and Steele, eds. Wiley, New York, 1048pp.

Robinson, A.R., J.C. McWilliams, (1974), The baroclinic instability of the open ocean. J. of Phys. Oc., 4, 281-294.

Worthington, L.V., (1976), On the North Atlantic Circulation. Johns Hopkins Univ. Press. 110pp.

Record length (days)	Band	Harmonics	Degrees of freedom	Days
196	1	1-3	6	196-65
324	1	1-4	8	324-81
196	2	3-7	10	65-28
324	2	5-11	14	65-29
196	3	8-19	24	24-10.3
324	3	12-32	42	27-10.1
196	4	20-49	60	9.8-4.0
324	4	33-81	98	9.8-4.0

Table 1. Summary of band averaging for 196 and 324 day record lengths.

Mooring	Depth (m)	Temperature (°C)	Velocity ($cm\ s^{-1}$)	168 Length (days)
		"Upper-thermocline" (180-300 m)		
79	172-322	172, 247, 322	172, 322	324
81	160-309	160, 233, 309	160, 309	196
82	194-338	194, 264, 338	194, 338	324
		"Mid-thermocline" (300-500 m)		
79	322-522	322, 522	322, 522	324
80	319-520	319, 520	319, 520	324
81	309-510	309, 510	309, 510	196
82	338-538	338, 538	338, 538	324
		"Deep-water" (2500-4000 m)		
81	2508-4008	2508, 4008	2508, 4008	324
82	2538-4038	4038	2538, 4038	324

Table 2. The nine available vertical instrument groupings. Note that no temperature was recorded by the mooring 82 instrument at 2538 m. Thus this pairing is only useful to evaluate horizontal temperature advection.

Mooring	T_t' (rms)	$u_H \cdot \nabla T$ (rms)	Residual (rms)	(error)
	"Upper-thermocline" (180-300 Meters)			
79	16.9/9.9	25.0/13.3	20.7/13.9	16.5/15.8
81	14.4/19.7	23.0/19.7	36.6†/32.0†	16.3/16.3
82	11.1/50.9	33.3/23.0	30.0†/40.6†	16.8/18.6
	"Mid-thermocline" (300-500 Meters)			
79	17.5/18.0	22.4/17.4	14.7/11.5	14.6/14.3
80	12.3/25.0	19.9/13.9	14.5/17.5	14.3/14.6
81	12.5/11.2	19.9/15.6	14.7/15.2	14.3/14.1
82	13.3/25.8	25.6/18.8	16.9/17.3	14.6/14.8
	"Deep-water" (2500-4000 Meters)			
81	0.41/.54	.56/.26	0.50/0.57	1.2/1.1

Table 3. Rms estimates of rate of change of temperature (T_t'), horizontal advection ($u_H \cdot \nabla T$), and their residual ($T_t' + u_H \cdot \nabla T$) in $x10^{-8}$°C s^{-1}. First number refers to the low frequency band, the second to the mid-frequency band. The last column shows the estimated error in the residual. Residuals that are significantly larger than the error at the 90% level are marked with a dagger (†).

Table 4. Coherence squared and phase between local change of temperature (T_t'), the components of horizontal advection of temperature, and total advection ($u_H \cdot \nabla T$) in (a) low-frequency band (324-81 days) and (b) mid-frequency band (65-29 days). Coherences which are significant from zero at the 90% confidence level are marked with a star (*). Also shown are the ratios of rms amplitude between T_t' and $u_H \cdot \nabla T$. Ratios which are significantly different from 1 at the 90% level are marked with a dagger (†). Mooring "79R" is a rotated version of the mooring 79 record (see text).

Mooring	Record length (days)	90% significance level	$\overline{UT}_x'$	$u'\overline{T}_x$	$u'T_x'$	$\overline{V}\overline{T}_y'$	$v'\overline{T}_y$	$v'T_y'$	$u_H \cdot \nabla T$	$\frac{rms(T_t')}{rms(u_H \cdot \nabla T)}$
					"Upper-thermocline" (180-300 Meters)					
79	324	.54	.86/163*	.56/119*	.74/-35*	.55/163*	.51/-124	.23/59	.41/-153	.68
79R	324	.54	.97/175*	.45/162	.68/-12*	.24/-114	.67/-102*	.07/64	.41/-153	.68
81	196	.68	.87/179*	.49/-7	.94/-15*	.53/61	.65/25	.65/-157	.83/3*	.62
82	324	.54	.59/-165*	.70/-93*	.08/-54	.06/168	.23/-98	.44/169	.53/-128	.33†
					"Mid-thermocline" (300-500 Meters)					
79	324	.54	.67/139*	.43/-95	.30/80	.13/153	.57/-157*	.46/-24	.52/-163	.78
79R	324	.54	.70/143*	.45/-177	.53/-42	.37/135	.51/-129	.50/72	.52/-163	.78
80	324	.54	.28/148	.63/-107*	.34/-16	.27/44	.40/-160	.07/-159	.48/-154	.62
81	196	.68	.05/-54	.08/83	.19/97	.65/-97	.37/175	.63/27	.49/164	.63
82	324	.54	.32/142	.61/61*	.19/-121	.10/-137	.36/-156	.41/164	.57/-171*	.52†
					"Deep-water" (2500-4000 Meters)					
81	324	.54	.44/-63	.09/-153	.52/167	.24/-109	.25/124	.37/114	.26/169	.74

Table 4a

Mooring	Record length (days)	90% significance level	$\bar{U}T_x'$	$u'\bar{T}_x$	$u'T_x'$	$\bar{V}T_y'$	$v'\bar{T}_y$	$v'T_y'$	$u_H \cdot \nabla T$	$\frac{rms\{T_t'\}}{rms\{u_H \cdot \nabla T\}}$
					"Upper-thermocline" (180-300 Meters)					
79	324	.32	.74/163*	.17/141	.38/-51*	.26/-61	.39/-61*	.30/99	.17/138	.75
79R	324	.32	.63/157*	.03/-144	.28/-22	.11/-109	.34/-55*	.23/109	.17/138	.75
81	196	.44	.41/120	.27/-139	.33/-63	.45/115*	.47/-5*	.17/175	.18/-42	1.00
82	324	.32	.85/-174*	.29/-129	.61/-157*	.45/48*	.89/-12*	.21/-15	.73/-136*	2.21†
					"Mid-thermocline" (300-500 Meters)					
79	324	.32	.29/139	.65/-136*	.65/-161*	.26/148	.57/-171*	.34/-30*	.70/-157*	1.03
79R	324	.32	.57/162*	.27/151	.53/-24*	.08/-112	.71/-151*	.76/-157*	.70/-157*	1.03
80	324	.32	.69/167*	.25/-165	.28/-177	.11/51	.26/-26	.08/178	.45/-173*	1.29
81	196	.44	.07/28	.04/130	.06/156	.07/-98	.04/-143	.10/82	.16/169	.72
82	324	.32	.52/175*	.23/51	.23/177	.28/-10	.44/-38*	.62/-153*	.72/-148*	1.37
					"Deep-water" (2500-4000 Meters)					
81	324	.32	.29/45	.48/-28*	.02/151	.20/134	.82/-170*	.27/-144	.17/-107	2.11†

Table 4b

Depth (m)	Low-frequency (Band 1)	Mid-frequency (Band 2)	High-frequency (Band 3)	(Band 4)
300 (196 days)	$\frac{1.33}{3.53}$ † (.37/.68/-44°)	$\frac{1.96}{2.62}$ (.04/.44/-80°)	$\frac{.61}{2.02}$ † (.14/.19/-148°)	$\frac{0.49}{1.31}$ † (.01/.08/-124°)
500 (324 days)	$\frac{6.13}{3.09}$ † (.46/.54/-04°)	$\frac{1.84}{4.89}$ † (.33/.32/-117°)	$\frac{1.08}{5.72}$ † (.04/.11/175°)	$\frac{0.47}{1.99}$ † (.02/.05/122°)
4000 (324 days)	$\frac{1.79}{1.99}$ (.43/.55/-121°)	$\frac{0.82}{2.04}$ † (.49/.32/144°)	$\frac{0.26}{0.92}$ † (.03/.11/75°)	$\frac{0.23}{0.46}$ † (.00/.05/-101°)

Table 5. The rms value of u_x (upper number) and v_y (lower number) in units of 10^{-7} s^{-1}. Ratios which are significantly different from 1.0 at the 90% level are shown with a dagger (†). The numbers in parentheses are (coherence squared, 90% significance level, phase) between u_x and v_y. Positive phase means u_x leads. Note that 300 m is a short record. Band definitions are given in Table 1.

Depth (m)	Low-frequency (Band 1)	Mid-frequency (Band 2)	High-frequency (Band 3)	(Band 4)
300 (196 days)	$\frac{4.27}{7.88}$ (.99/.68/-151°)	$\frac{2.95}{2.66}$ (.29/.44/-168°)	$\frac{2.08}{0.18}$ † (.43/.19/62°)	$\frac{1.31}{0.04}$ † (.06/.08/156°)
500 (324 days)	$\frac{9.79}{11.82}$ (.88/.54/158°)	$\frac{5.28}{2.42}$ † (.06/.32/94°)	$\frac{2.91}{0.34}$ † (.06/.11/-29°)	$\frac{1.50}{0.10}$ † (.04/.05/26°)
4000 (324 days)	$\frac{2.93}{3.80}$ (.54/.54/-141°)	$\frac{3.91}{0.92}$ † (.42/.32/-176°)	$\frac{1.00}{0.15}$ † (.28/.11/109°)	$\frac{0.75}{0.02}$ † (.16/.05/75°)

Table 6. The rms value of $(v_x - u_y)$ (upper number) and $\int \beta v dt$ (lower number) in units of 10^{-7} s^{-1}. Ratios which are significantly different from 1 at the 90% level are marked with a dagger (†). The numbers in parentheses are (coherence squared, 90% significance level, phase) between $(v_x - u_y)$ and $(\int \beta v dt)$. Positive phase means $(v_x - u_y)$ leads. Note that 300 m is a short record. Band definitions are given in Table 1.

Table 7. Comparison of vorticity plus time integrated advection of planetary vorticity to vertical stretching. w_1 refers to vertical velocity at some near-surface point, w_2 to an away-surface point. w_{240}, w_{400}, w_{3250} are vertical velocity in the upper, mid-thermocline and deep-water, respectively, derived from temperature conservation. w_{sfc} and w_{bot} are vertical velocity at the surface and bottom. The top numbers in the four frequency band columns refers to the rms value of $\zeta + \int \beta v dt$, the bottom number to the rms value of stretching, in units of $10^{-7} s^{-1}$. An X indicates that the amplitude is somewhat arbitrary (see text). The numbers in parentheses are (coherence squared, 90% significance level, phase), where positive phase means $\zeta + \int \beta v dt$ leads. See Table 1 for frequency band definitions.

$\zeta + \int \beta dt$	w_1	w_2	Low-frequency (Band 1)	Mid-frequency (Band 2)	High-frequency (Band 3)	(Band 4)
300m	$\frac{w_{240}}{160m}$	$w_{400} = 0$	$\frac{4.68}{26.99}$ X (.76,.68,-179°)	$\frac{2.74}{7.50}$ X (.05,.44,74°)	$\frac{2.15}{2.59}$ X (.22,.19,39°)	$\frac{1.30}{.96}$ X (.06,.08,126°)
300m	$w_{sfc} = 0$	$\frac{w_{400}}{400m}$	$\frac{4.68}{10.33}$ (.68,.68,10.2°)	$\frac{2.74}{2.90}$ (.22,.44,-162°)	$\frac{2.15}{1.16}$ (.14,.19,95°)	$\frac{1.30}{0.55}$ (.32,.08,176°)
300m	$\frac{w_{240}}{160m}$	$\frac{w_{400}}{160m}$	$\frac{4.68}{5.62}$ (.57,.68,128°)	$\frac{2.74}{4.33}$ (.42,.44,167°)	$\frac{2.15}{3.39}$ (.19,.19,155°)	$\frac{1.30}{1.48}$ (.45,.08,163°)
500m	$\frac{w_{240}}{160m}$	$w_{400}=0$	$\frac{4.95}{26.99}$ X (.72,.68,-128°)	$\frac{3.74}{7.50}$ X (.43,.44,148°)	$\frac{2.01}{2.59}$ X (.11,.19,76°)	$\frac{0.83}{0.96}$ X (.11,.08,163°)
500m	$\frac{w_{400}}{2850m}$	$w_{3250}=0$	$\frac{4.95}{1.45}$ X (.58,.68,-126°)	$\frac{3.74}{0.41}$ X (.34,.44,114°)	$\frac{2.01}{0.16}$ X (.06,.19,62°)	$\frac{0.83}{0.08}$ X (.11,.08,-2°)
500m	$\frac{w_{400}}{2850m}$	$\frac{w_{3250}}{2850m}$	$\frac{4.95}{2.65}$ (.63,.68,-34°)	$\frac{3.74}{1.35}$ (.52,.44,-35°)	$\frac{2.01}{0.32}$ (.27,.19,45°)	$\frac{0.83}{0.19}$ (.06,.08,-85°)
4000m	$\frac{w_{3250}}{2050m}$	$w_{bot}=0$	$\frac{3.27}{6.59}$ (.52,.54,-124°)	$\frac{3.33}{1.36}$ (.29,.32,-48°)	$\frac{0.98}{0.32}$ (.19,.11,-73°)	$\frac{0.75}{0.19}$ (.03,.05,84°)
4000m	$\frac{w_{3250}}{2050m}$	$\frac{w_{bot}}{2050m}$	$\frac{3.27}{11.73}$ (.39,.54,4°)	$\frac{3.33}{1.49}$ (.15,.32,-66°)	$\frac{0.98}{0.37}$ (.34,.11,-10.2°)	$\frac{0.75}{0.18}$ (.00,.05,20°)

Table 7

Mooring	Low-frequency (Band 1)	Mid-frequency (Band 2)
	"Upper-thermocline" (180-300 Meters)	
79	.97/163°	1.06/163°
81	1.23/179°	2.5/120°
82	.80/-165°	2.64/-174°
	"Mid-thermocline" (300-500 Meters)	
79	3.99/139°	5.93/139°
80	1.65/148°	2.71/167°
81	1.76/-54°	1.83/28°
82	1.33/142°	2.71/175°

Table 8. Ratio of rms T'_t to rms $\overline{UT}'_x$ and phase. Positive phase means T'_t leads. Mooring 81 is a short record. See Table 1 for band definitions.

Figure Captions

Figure 1. Estimated absolute zonal velocity at Cluster C. Derived from historical hydrographic stations using the dynamical method. Level of no motion is chosen as 2500m. From Keffer and Niiler (1980).

Figure 2. Brunt-Vaisala profile from the ensemble average of 28 stations taken during the 1978 Cluster C recovery cruise.

Figure 3. Northward potential vorticity gradient calculated as $Q_y = \beta - (f^2 \bar{U}_z/N^2)_z$ where $\bar{U}$ is from the profile in Figure 1 and N^2 is from the profile in Figure 2. The dashed line is the planetary vorticity gradient β.

Figure 4. The e-folding time for five different classes of modes calculated from Eqn. (2.19) as a function of zonal wavenumber. A north-south bottom slope of -2×10^{-3} was assumed. The modes at the points marked A and B are shown in Figure 5.

Figure 5. (a) The amplitude as a function of depth of the two modes marked in Figure 4, scaled so their maximum amplitude is 1. The mode marked A is the fastest growing thermocline mode while the mode marked B is a slower growing, larger mode. The symbols mark the relative observed v velocity amplitudes in the low-frequency band, scaled such that they

match mode A at 500m. Any of the mooring or mode relative amplitudes can be multiplyed by an arbitrary constant. (b) Phases of the same two modes. Also shown is the relative phases of the v velocites, shifted so that they match mode A at 500m. An arbitrary constant can be added.

Figure 6. A schematic of the Cluster C mooring and instrument locations.

Figure 7. (a) Vertically averaged high frequency (4 to 30 days) local temperature change (T'_t), negative horizontal advection ($-u_H \cdot \nabla T$) and their residual at mooring 82, between 338 and 538 m. (b) Same, except low-frequency (30 to 324 days).

Figure 8. Reynold's decomposition of vertically averaged low-frequency (30 to 324 days) horizontal advection. (a) Components of uT_x; (b) components of vT_y.

Figure 9. The estimated components of horizontal divergence and their sum at 500 m.

Figure 10. Estimated sampling error of horizontal divergence in units of $10^{-6} s^{-1}$ for a 5 cm s^{-1} rms current in the form of a plane wave, plotted as a function of horizontal wavenumber. See Appendix A. (a) Coherence of unity across the array; (b) coherence of 0.8 across the array.

Figure 11. The estimated components of relative vorticity at 500 m.

Figure 12. The estimated ratio of observed to actual relative vorticity as a function of horizontal wavenumber, assuming a coherence of unity across the array. See Appendix A.

Figure 13. Relative vorticity (ζ), negative time integrated advection of planetary vorticity ($-\int \beta v dt$) and their residual. Only the estimate measurement error is shown. (a) 300 meters; (b) 500 meters; (c) 4000 meters.

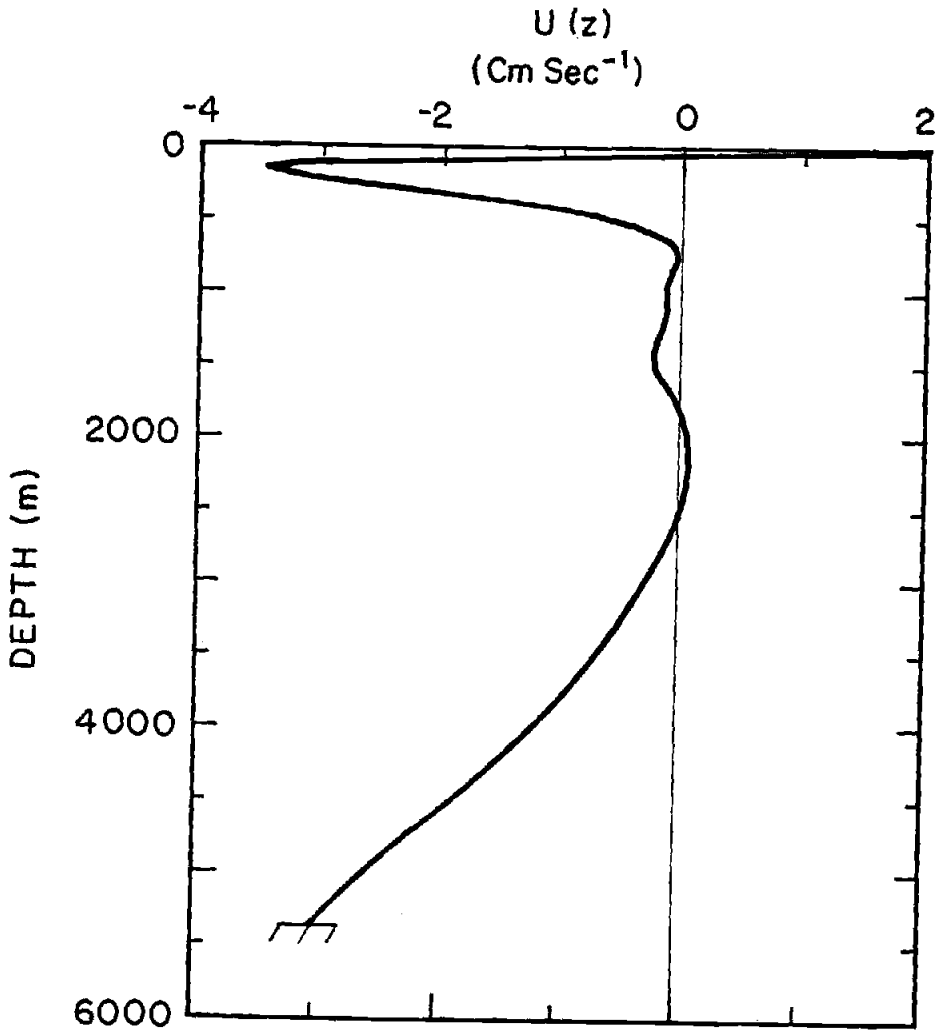

Figure 1

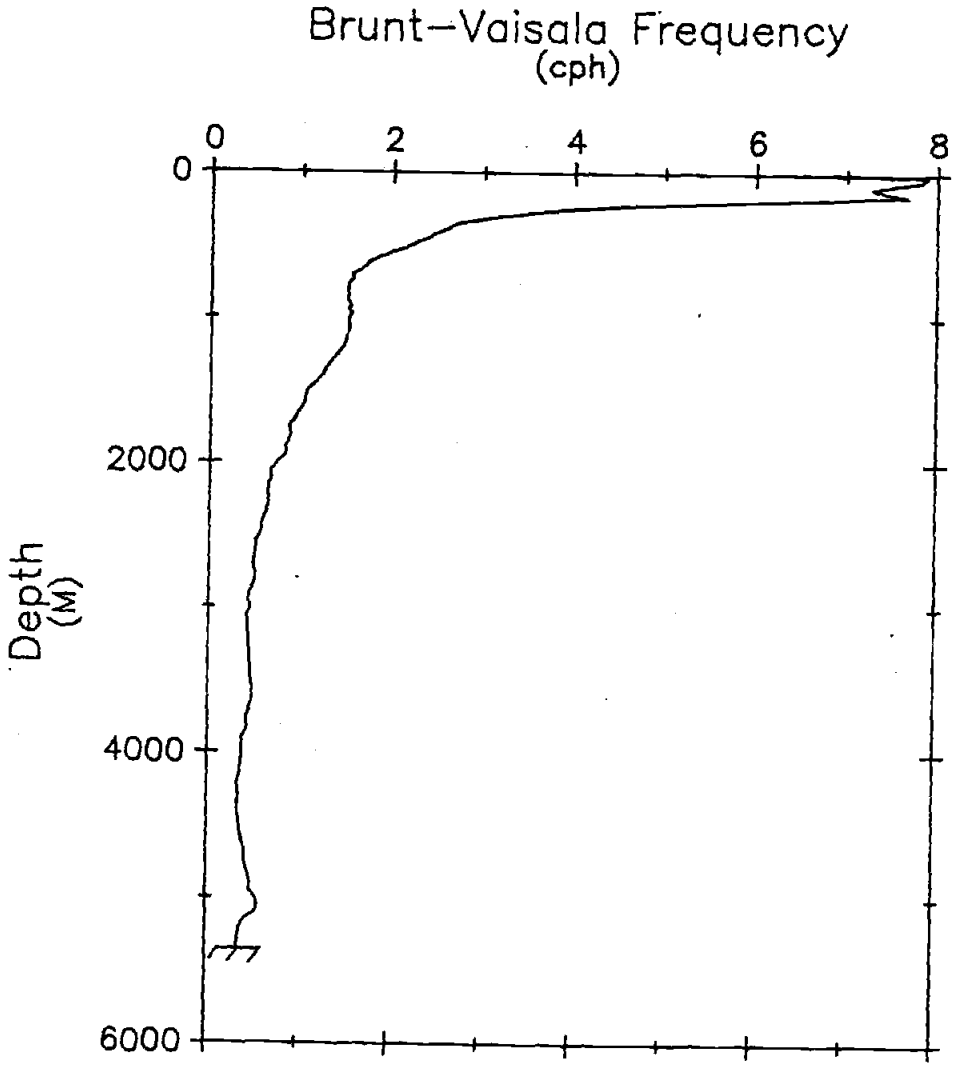

Figure 2

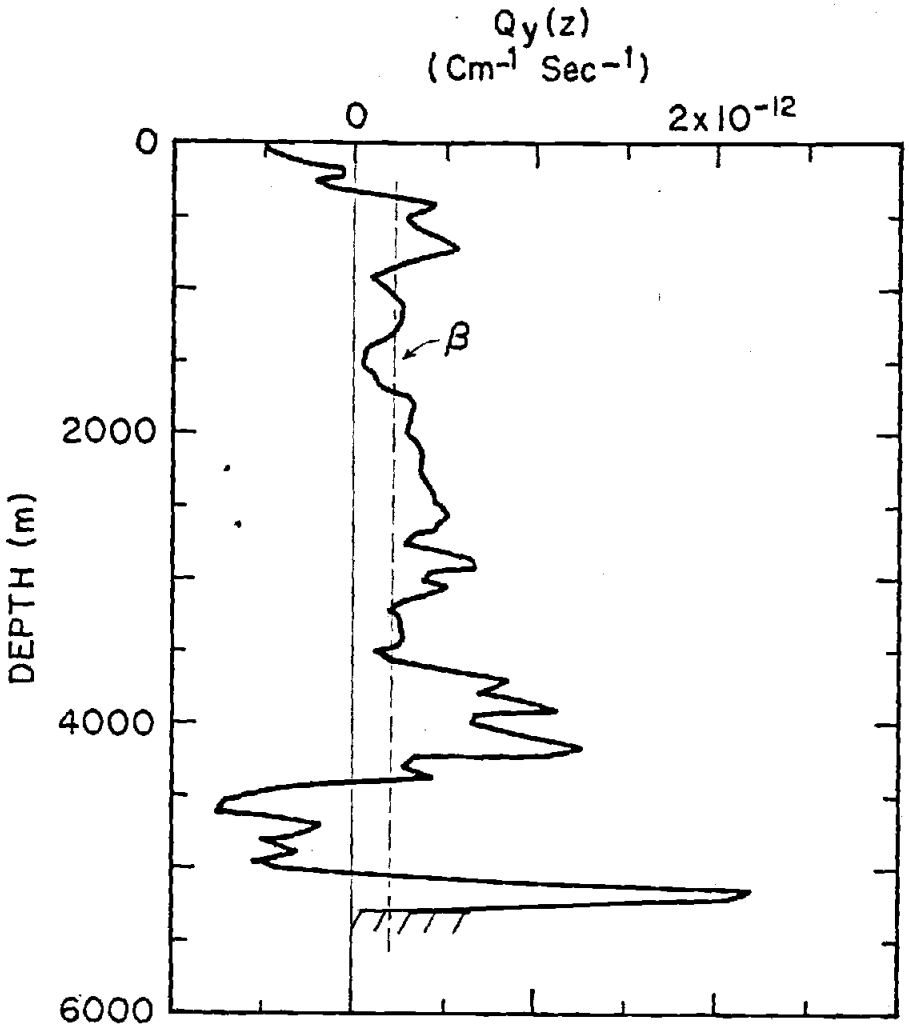

Figure 3

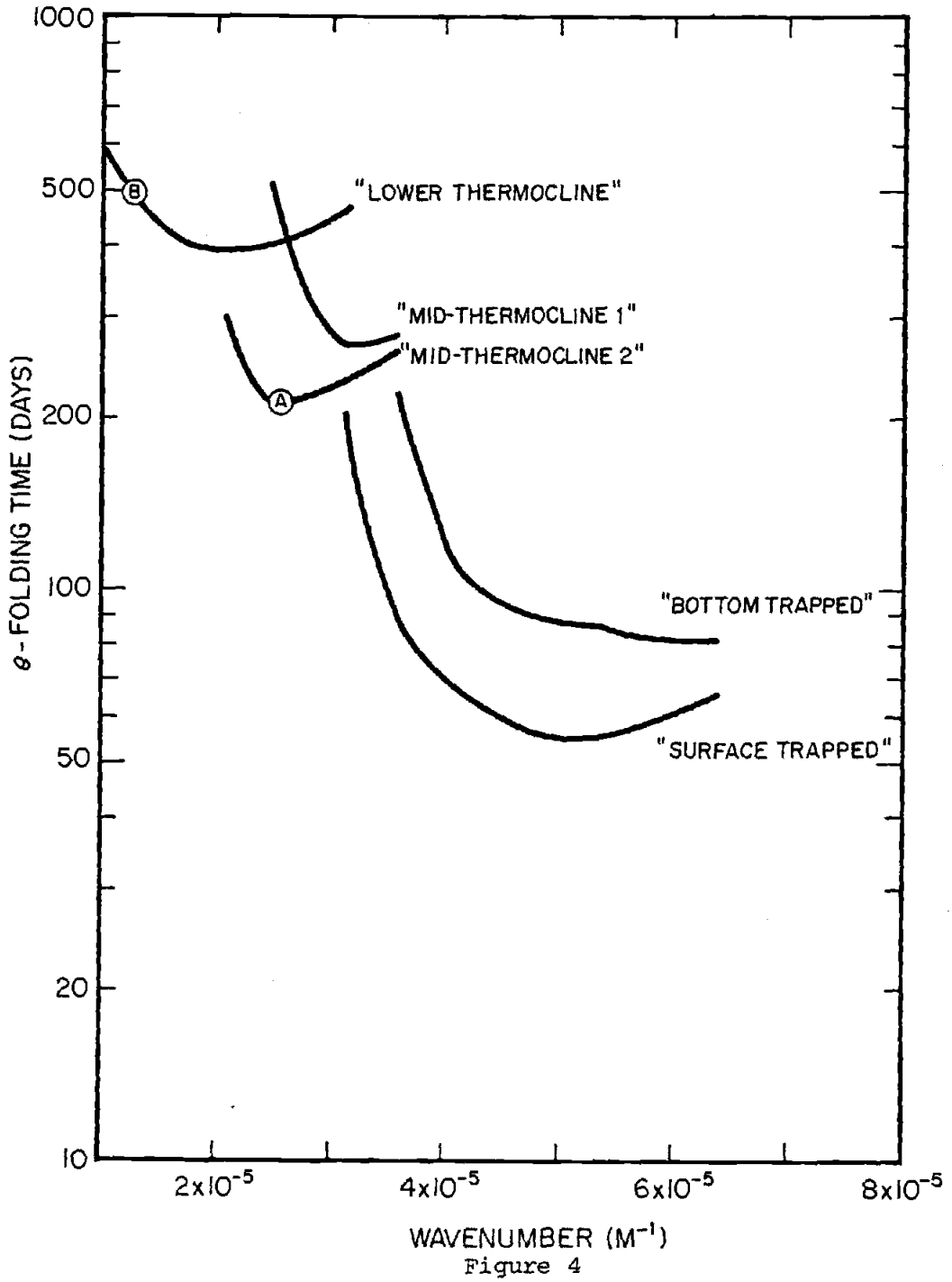
1000
500
200
100
50
20
10
ø - FOLDING TIME (DAYS)
B
A
"LOWER THERMOCLINE"
"MID-THERMOCLINE 1"
"MID-THERMOCLINE 2"
"BOTTOM TRAPPED"
"SURFACE TRAPPED"
2x10⁻⁵
4x10⁻⁵
6x10⁻⁵
8x10⁻⁵
WAVENUMBER (M⁻¹)

Figure 4

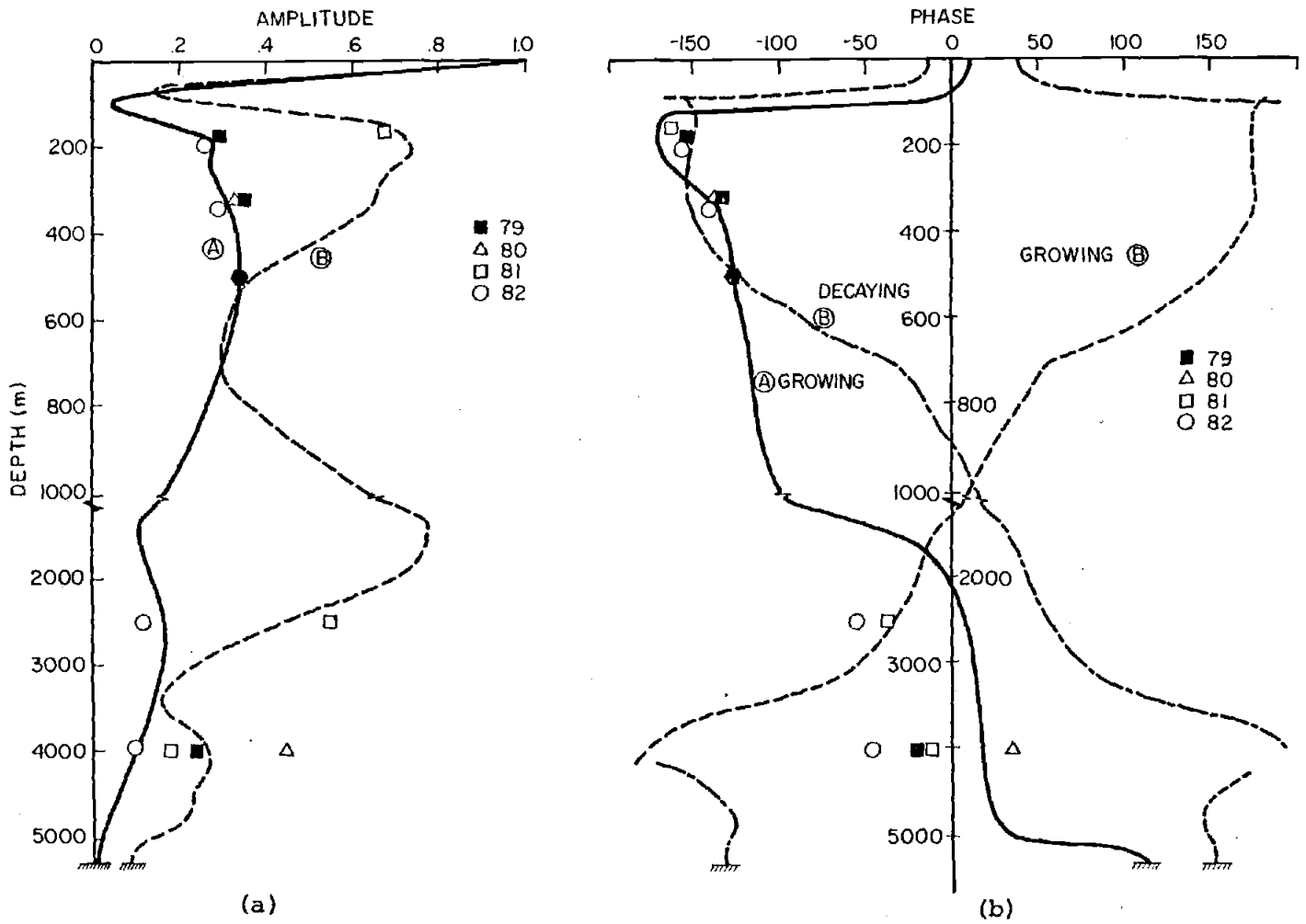
AMPLITUDE
0
.2
.4
.6
.8
1.0
DEPTH (m)
200
400
600
800
1000
2000
3000
4000
5000
79
80
81
82
Ⓐ
Ⓑ
(a)
PHASE
-150
-100
-50
0
50
100
150
GROWING Ⓑ
DECAYING
Ⓑ
Ⓐ GROWING
79
80
81
82
(b)

Figure 5

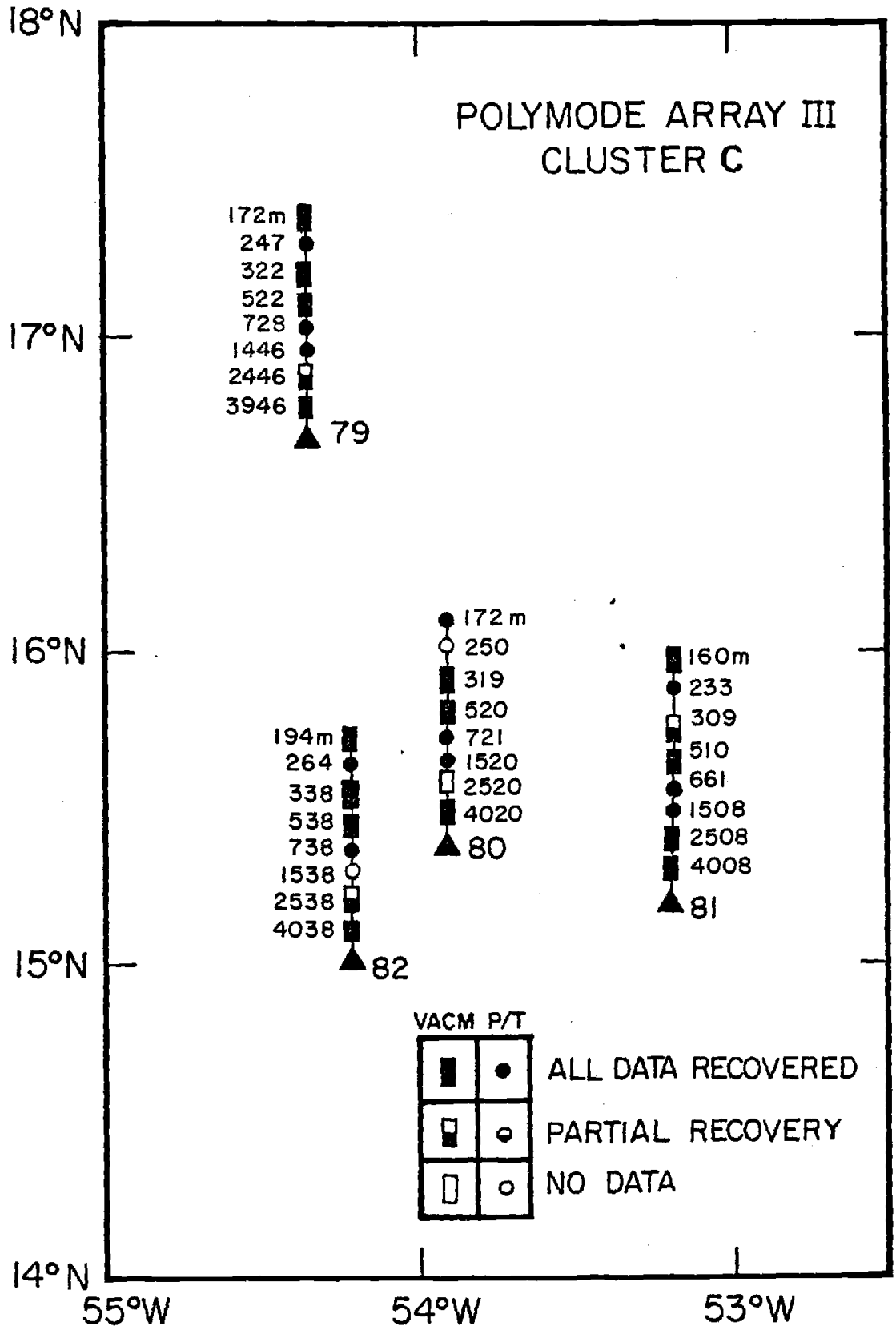
18°N
17°N
16°N
15°N
14°N
55°W
54°W
53°W
POLYMODE ARRAY III
CLUSTER C
172m
247
322
522
728
1446
2446
3946
79
172 m
250
319
520
721
1520
2520
4020
80
160m
233
309
510
661
1508
2508
4008
81
194m
264
338
538
738
1538
2538
4038
82
VACM P/T
ALL DATA RECOVERED
PARTIAL RECOVERY
NO DATA

Figure 6

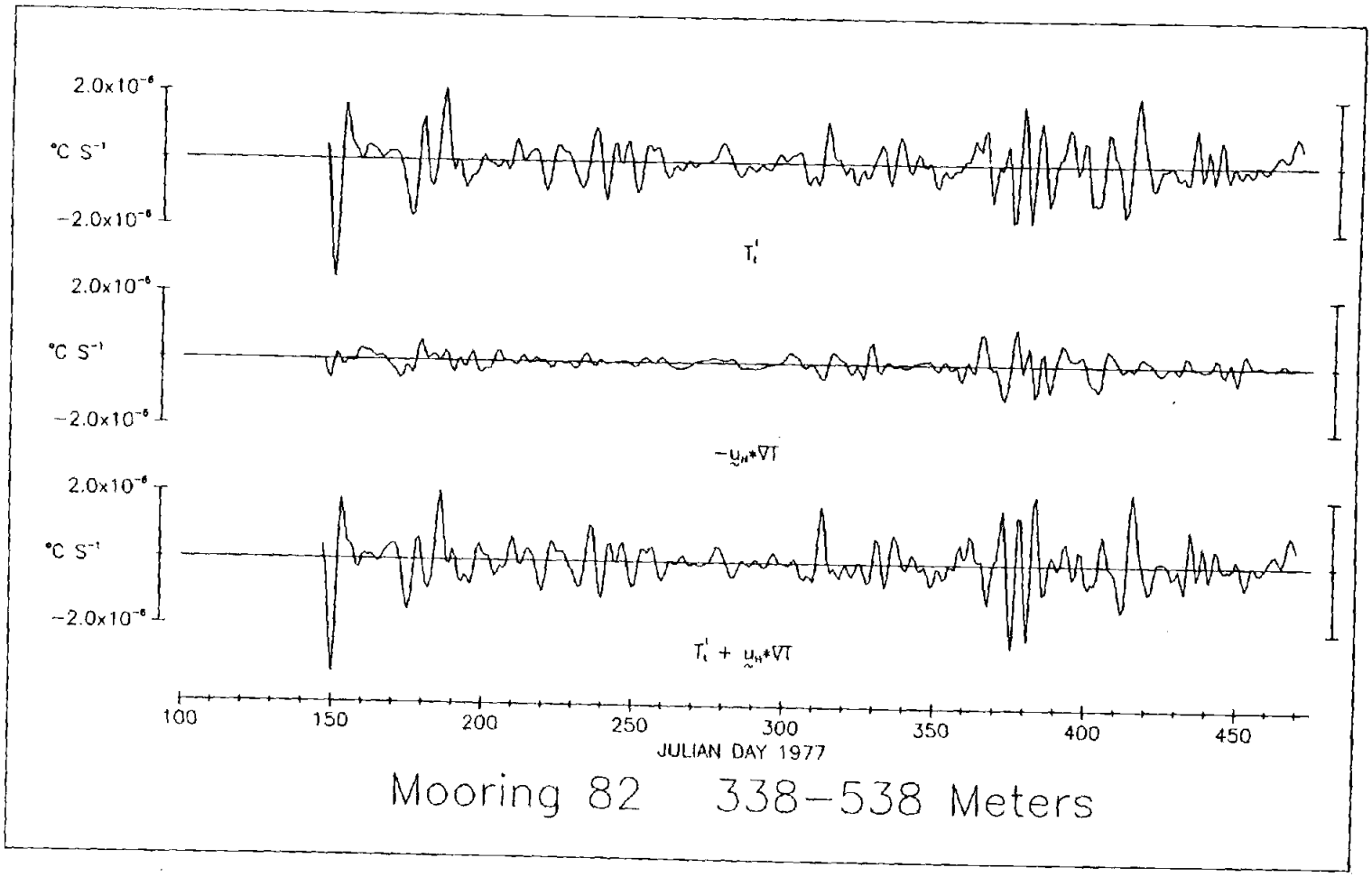
2.0x10⁻⁶
°C S⁻¹
-2.0x10⁻⁶
T_t'
2.0x10⁻⁶
°C S⁻¹
-2.0x10⁻⁶
-u_H*∇T
2.0x10⁻⁶
°C S⁻¹
-2.0x10⁻⁶
T_t' + u_H*∇T
100
150
200
250
300
350
400
450
JULIAN DAY 1977
Mooring 82 338-538 Meters

Figure 7a

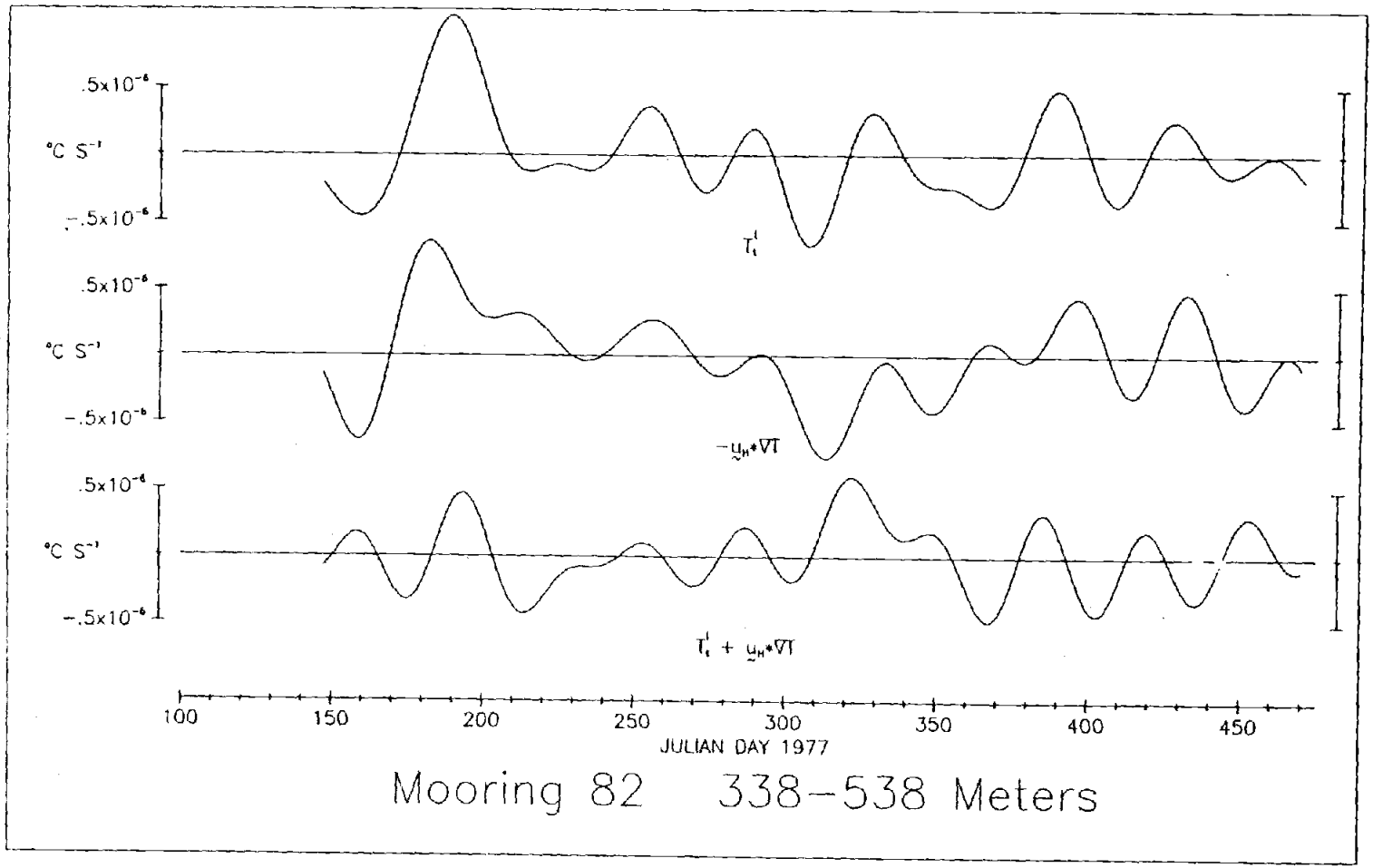
.5x10⁻⁶
°C S⁻¹
-.5x10⁻⁶
T'ₜ
.5x10⁻⁶
°C S⁻¹
-.5x10⁻⁶
-u_H*∇T
.5x10⁻⁶
°C S⁻¹
-.5x10⁻⁶
T'ₜ + u_H*∇T
100
150
200
250
300
350
400
450
JULIAN DAY 1977
Mooring 82 338-538 Meters

Figure 7b

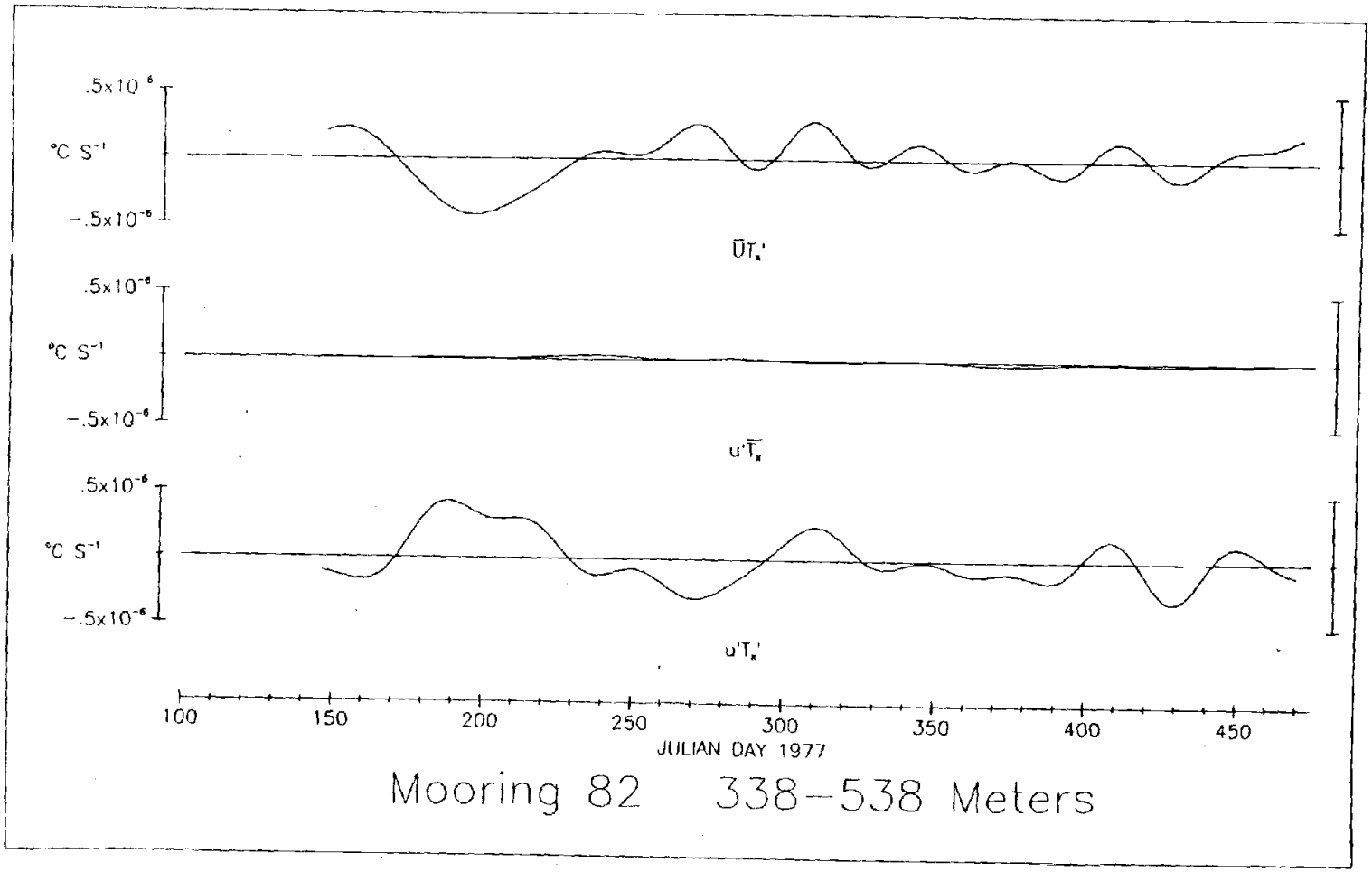
.5x10⁻⁶
°C S⁻¹
-.5x10⁻⁶
$\overline{v}T_z'$
.5x10⁻⁶
°C S⁻¹
-.5x10⁻⁶
$u'\overline{T}_z$
.5x10⁻⁶
°C S⁻¹
-.5x10⁻⁶
$u'T_z'$
100
150
200
250
300
350
400
450
JULIAN DAY 1977
Mooring 82 338-538 Meters

Figure 8a

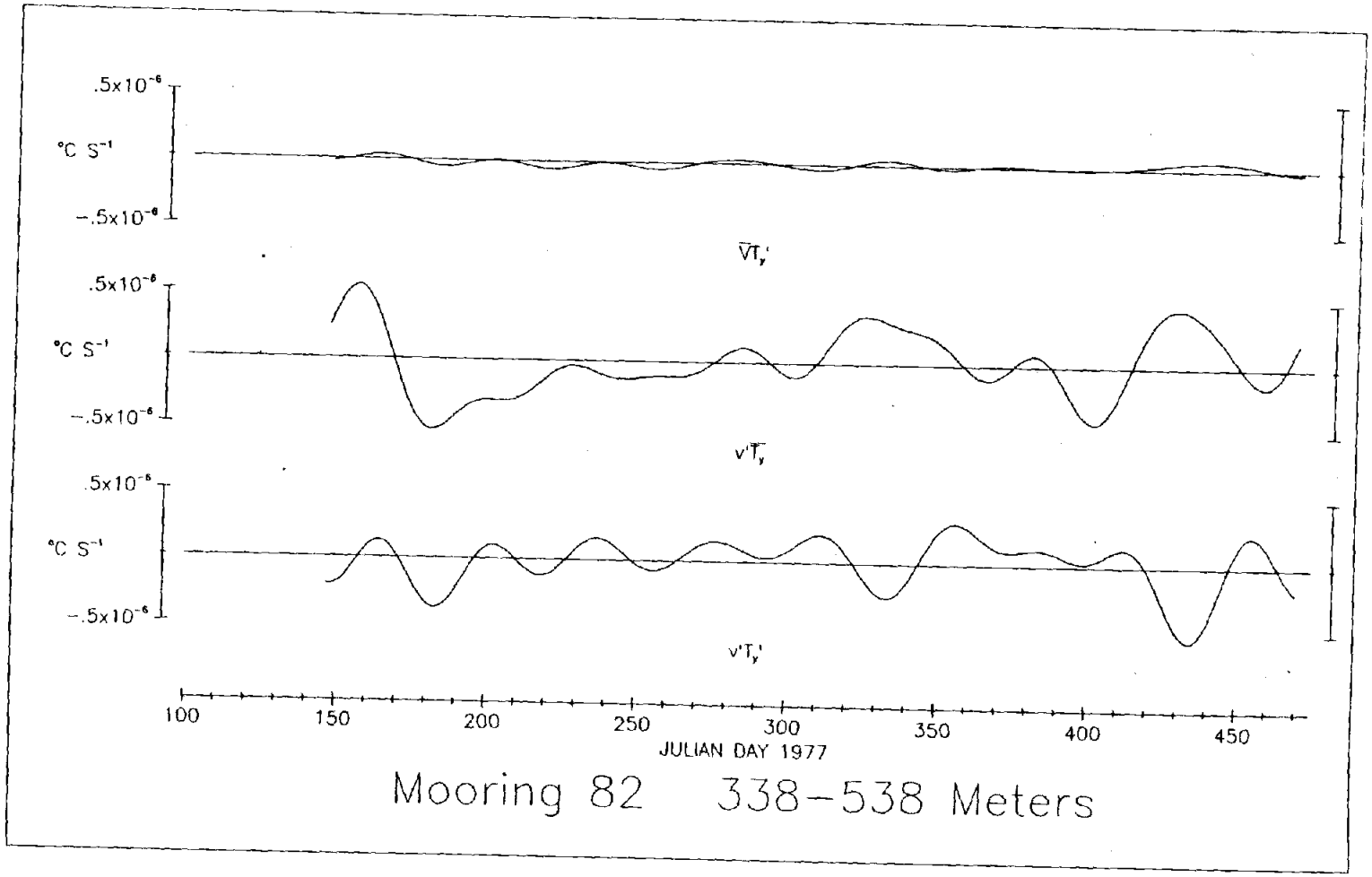
.5x10⁻⁶
°C S⁻¹
-.5x10⁻⁶
$\overline{v}\overline{T}_y$'
.5x10⁻⁶
°C S⁻¹
-.5x10⁻⁶
$v'\overline{T}_y$
.5x10⁻⁶
°C S⁻¹
-.5x10⁻⁶
$v'T_y'$
100
150
200
250
300
350
400
450
JULIAN DAY 1977
Mooring 82 338-538 Meters

Figure 8b

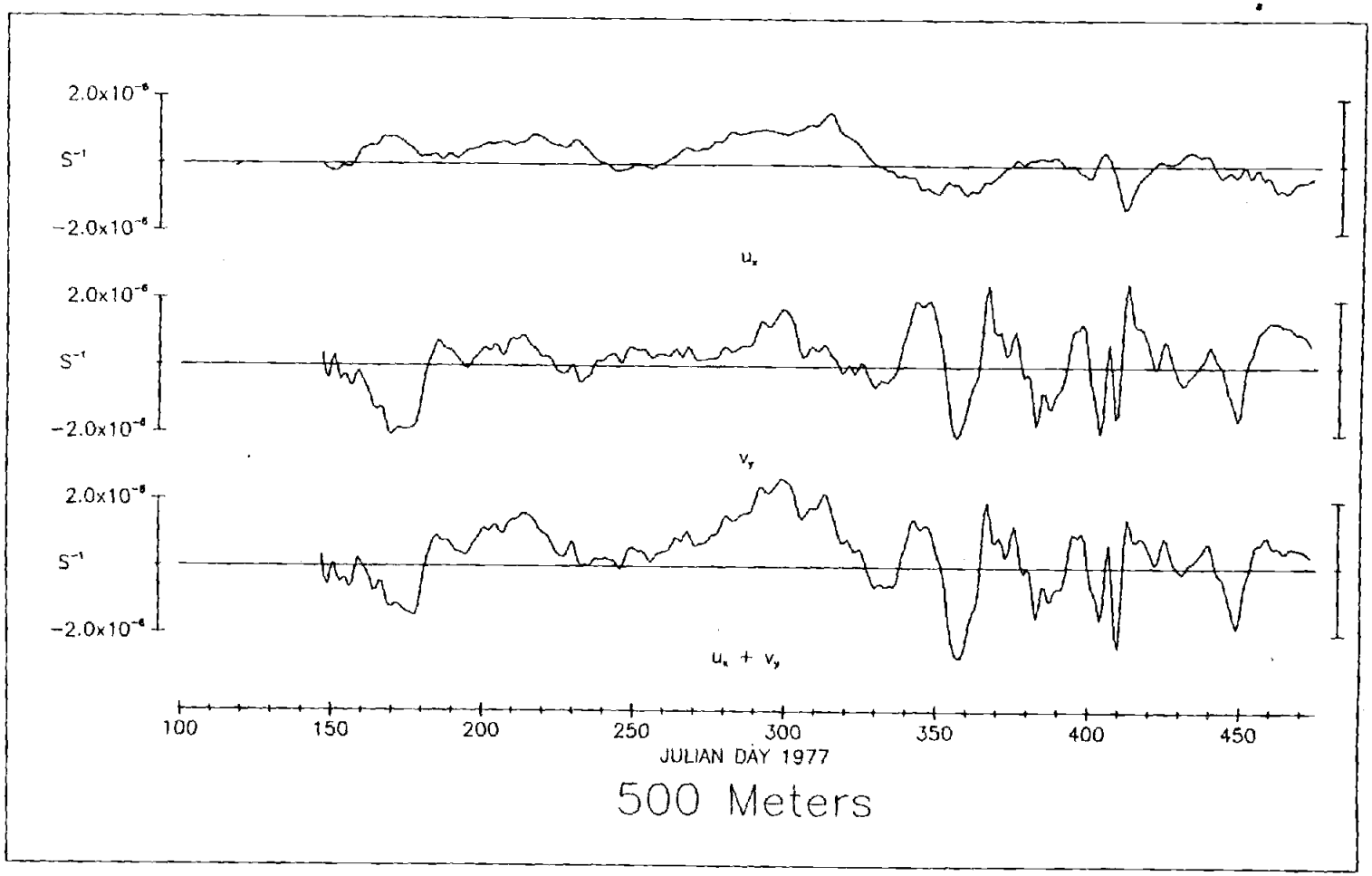
2.0x10⁻⁶
S⁻¹
-2.0x10⁻⁶
u
2.0x10⁻⁶
S⁻¹
-2.0x10⁻⁶
v
2.0x10⁻⁶
S⁻¹
-2.0x10⁻⁶
u + v
100
150
200
250
300
350
400
450
JULIAN DAY 1977
500 Meters

Figure 9

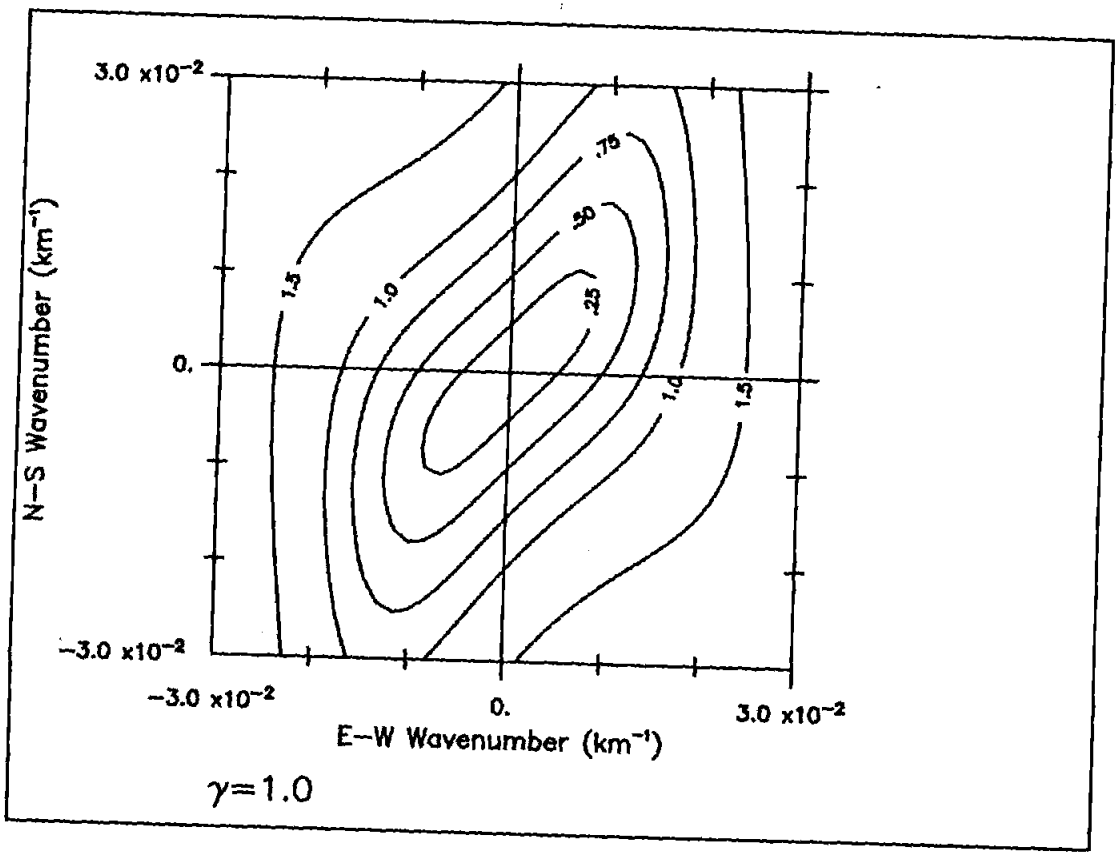
3.0 x10⁻²
0.
−3.0 x10⁻²
N−S Wavenumber (km⁻¹)
−3.0 x10⁻²
0.
3.0 x10⁻²
E−W Wavenumber (km⁻¹)
.75
.50
.25
1.5
1.0
1.5
1.0
1.5
γ=1.0

Figure 10a

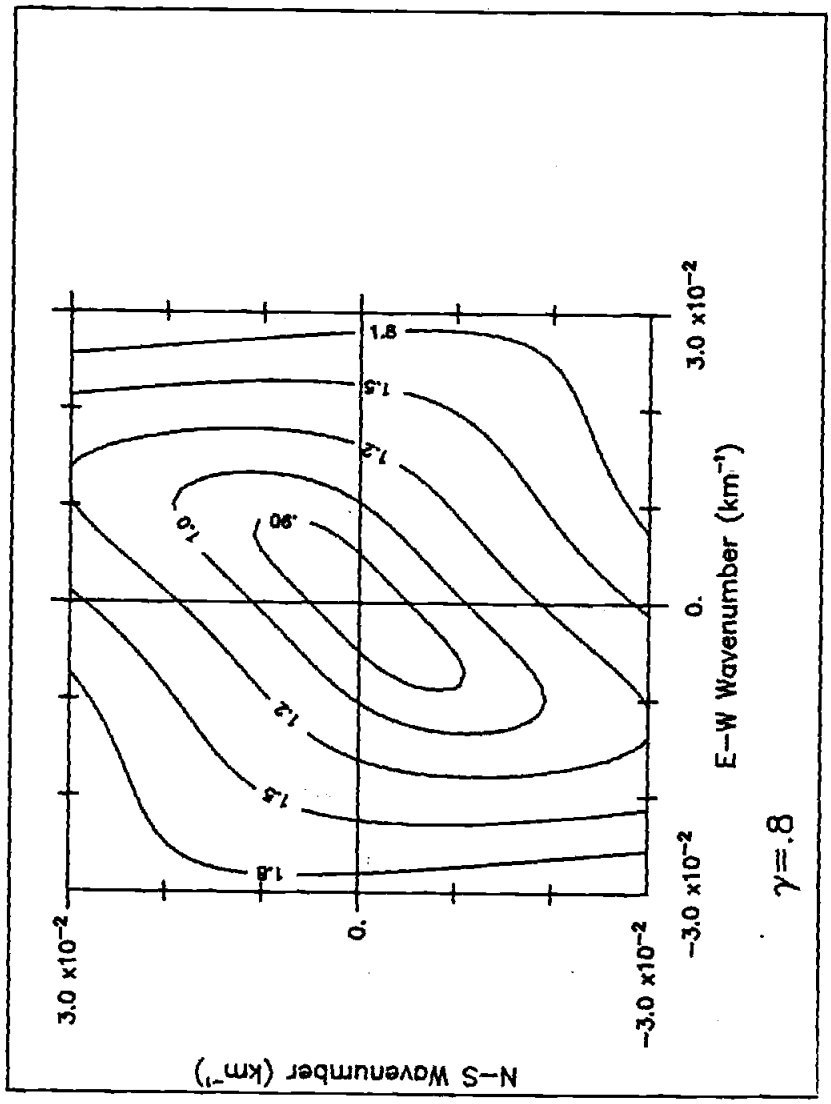
1.8
1.5
1.2
.90
1.0
1.2
1.5
1.8
3.0 x10⁻²
0.
-3.0 x10⁻²
E-W Wavenumber (km⁻¹)
γ=.8
N-S Wavenumber (km⁻¹)

Figure 10b

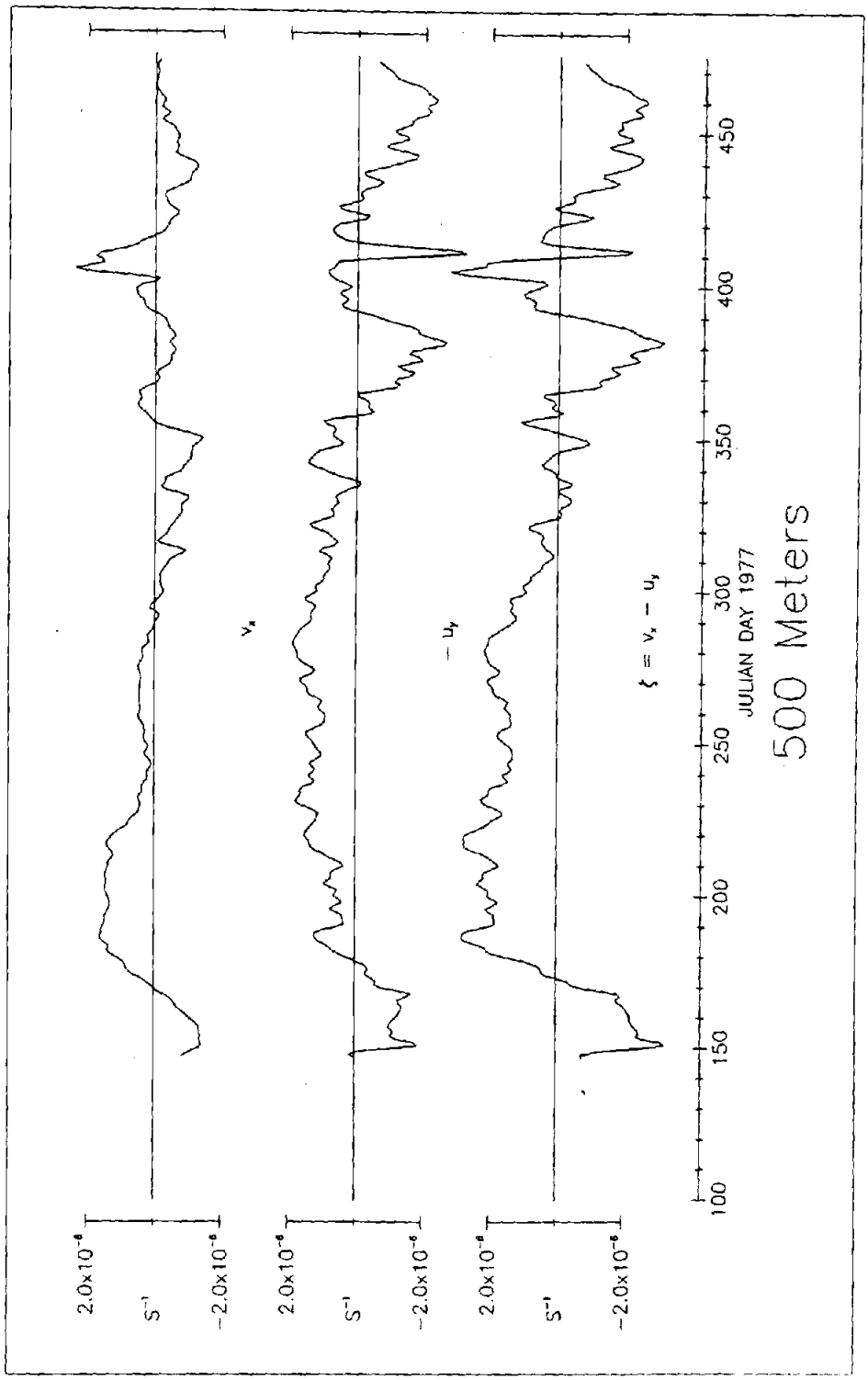
2.0x10⁻⁶
S⁻¹
-2.0x10⁻⁶
v_x
2.0x10⁻⁶
S⁻¹
-2.0x10⁻⁶
- u_y
2.0x10⁻⁶
S⁻¹
-2.0x10⁻⁶
ζ = v_x - u_y
100
150
200
250
300
350
400
450
JULIAN DAY 1977
500 Meters

Figure 11

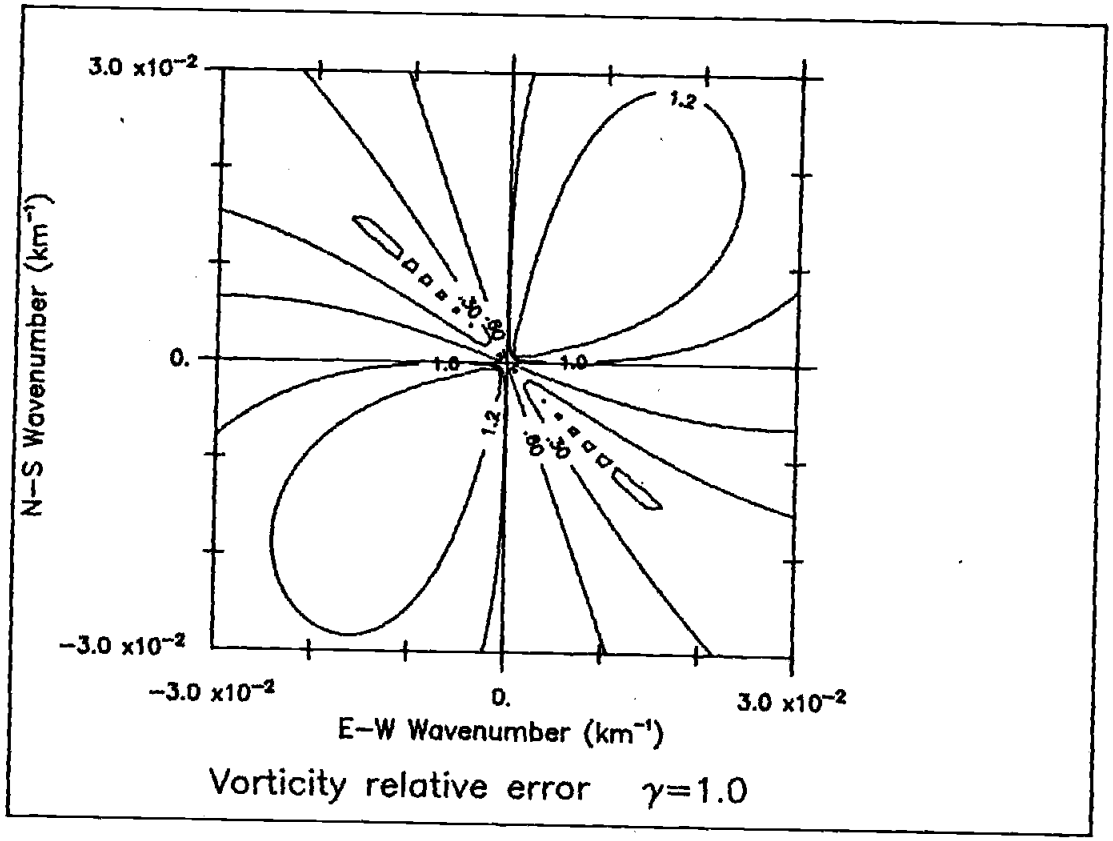
3.0 x10⁻²
0.
−3.0 x10⁻²
−3.0 x10⁻²
0.
3.0 x10⁻²
N−S Wavenumber (km⁻¹)
E−W Wavenumber (km⁻¹)
1.2
1.0
.8
.6
Vorticity relative error γ=1.0

Figure 12

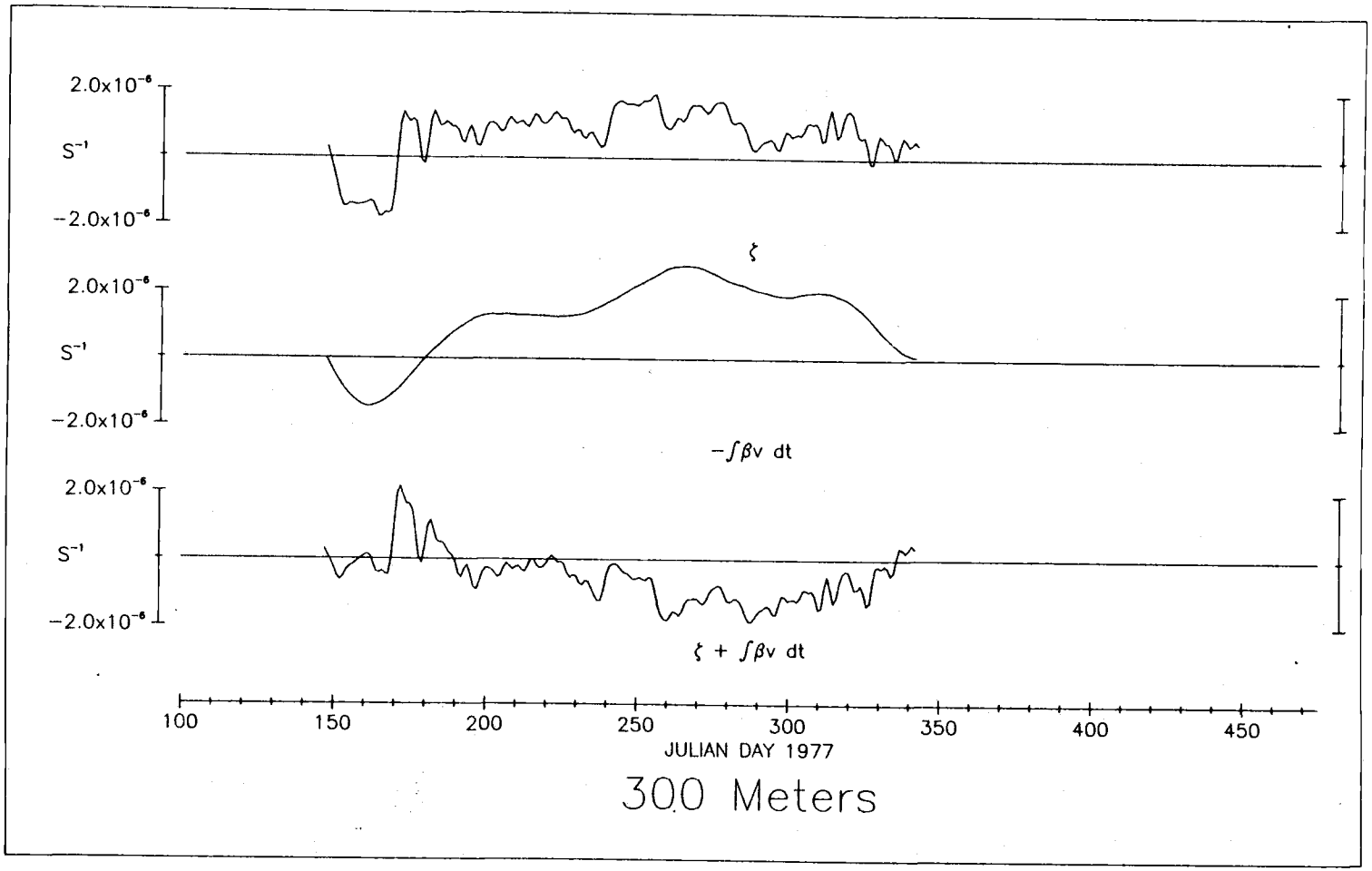
2.0x10⁻⁶
S⁻¹
-2.0x10⁻⁶
ζ
2.0x10⁻⁶
S⁻¹
-2.0x10⁻⁶
-∫βv dt
2.0x10⁻⁶
S⁻¹
-2.0x10⁻⁶
ζ + ∫βv dt
100
150
200
250
300
350
400
450
JULIAN DAY 1977
300 Meters

Figure 13a

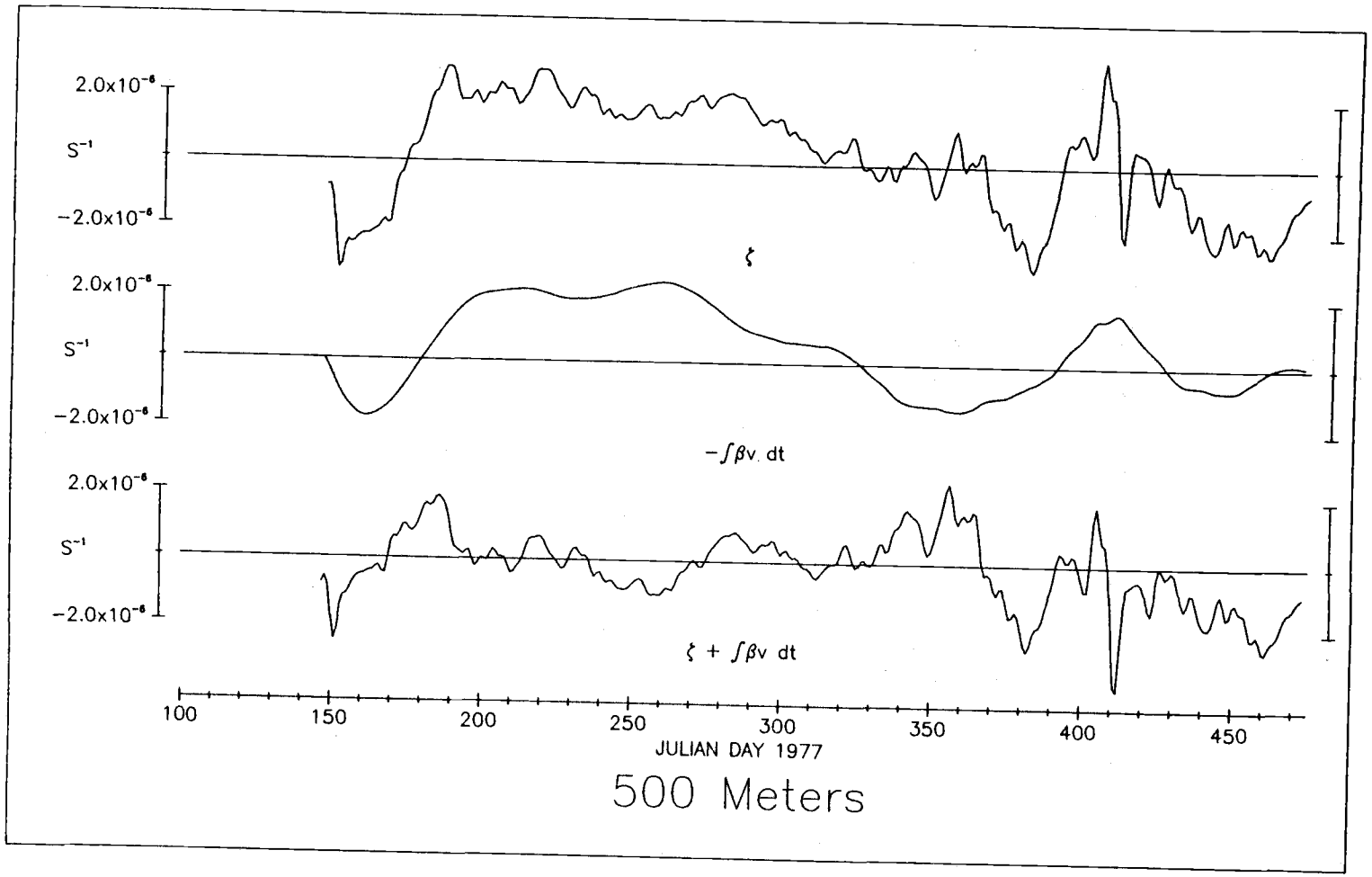
2.0x10⁻⁶
S⁻¹
-2.0x10⁻⁶
ζ
2.0x10⁻⁶
S⁻¹
-2.0x10⁻⁶
-∫βv dt
2.0x10⁻⁶
S⁻¹
-2.0x10⁻⁶
ζ + ∫βv dt
100
150
200
250
300
350
400
450
JULIAN DAY 1977
500 Meters

Figure 13b

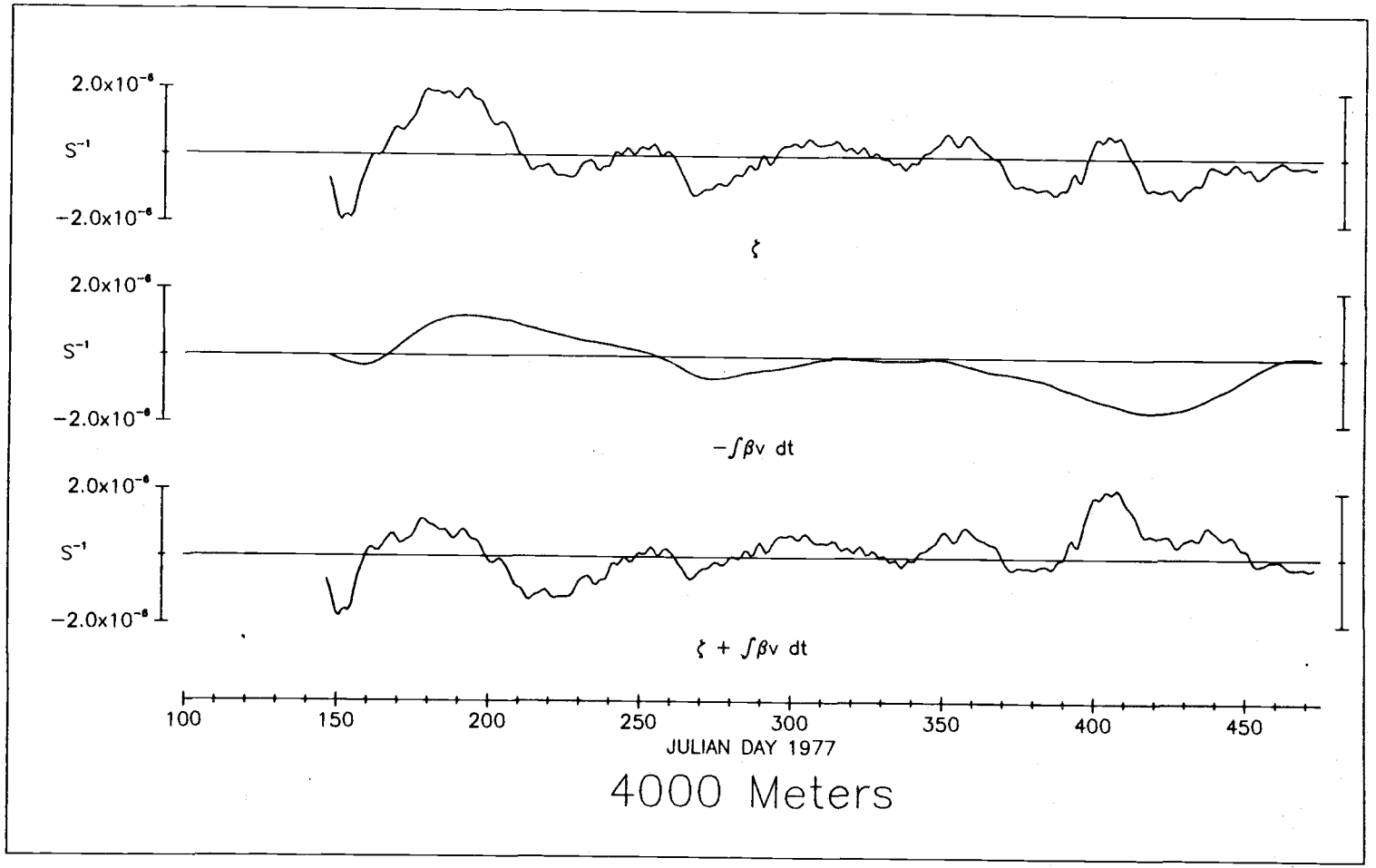
2.0x10⁻⁶
S⁻¹
-2.0x10⁻⁶
ζ
2.0x10⁻⁶
S⁻¹
-2.0x10⁻⁶
−∫βv dt
2.0x10⁻⁶
S⁻¹
-2.0x10⁻⁶
ζ + ∫βv dt
100
150
200
250
300
350
400
450
JULIAN DAY 1977
4000 Meters

Figure 13c